# Avalanche-mode silicon LEDs for monolithic optical coupling in CMOS technology

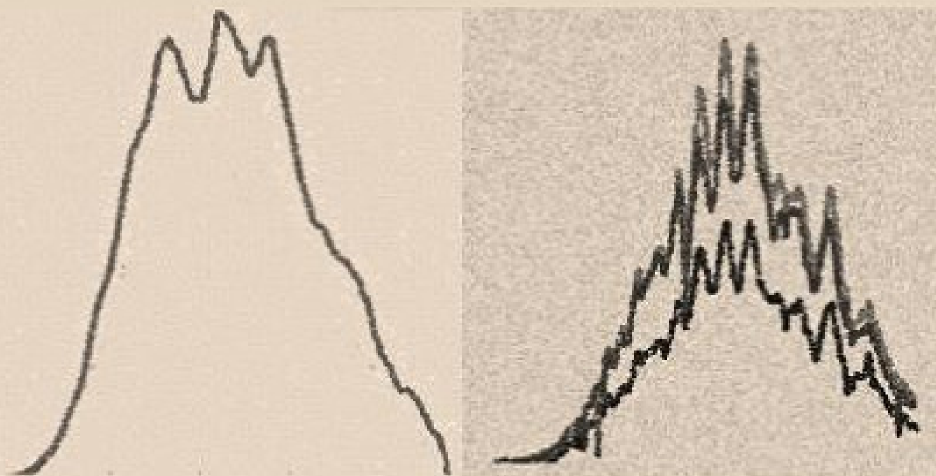

*Satadal Dutta*

# Avalanche-mode silicon LEDs for monolithic optical coupling in CMOS technology

Satadal Dutta

Members of the dissertation committee:

| | | |
|---|---|---|
| prof. dr. | P.M.G. Apers | University of Twente, EWI (chairman/secretary) |
| prof. dr. | J. Schmitz | University of Twente, EWI (supervisor) |
| dr. ir. | R.J.E. Hueting | University of Twente, EWI (co-supervisor) |
| dr. ir. | A.J. Annema | University of Twente, EWI (co-supervisor) |
| dr. ir. | R. Heideman | LioniX International, Enschede (referee) |
| prof. dr. ir. | B. Nauta | University of Twente, EWI |
| prof. dr. | L.K. Nanver | University of Twente, EWI |
| prof. dr. | P.G. Steeneken | Delft University of Technology, 3ME |
| prof. dr. | L.W. Snyman | University of South Africa, Johannesburg |

This work is part of the Optocoupling in CMOS project (no. 12835) and is supported financially by the Applied and Engineering Science division (TTW) of the Netherlands Organization for Scientific Research (NWO).

MESA+ Institute for Nanotechnology, University of Twente
P.O.Box 217, 7500 AE Enschede, the Netherlands

Copyright © 2017 by Satadal Dutta, Enschede, The Netherlands.

This work is licensed under the Creative Commons Attribution-Non-Commercial 3.0 Netherlands License. To view a copy of this license, visit http://creativecommons.org/licenses/by-nc/3.0/nl/ or send a letter to Creative Commons, 171 Second Street, Suite 300, San Francisco, California 94105, USA.

Typeset with LaTeX. Printed by Gildeprint, Enschede, The Netherlands.
Cover background: Aurora Borealis.
Source: https://commons.wikimedia.org/wiki/Aurora (available under the Creative Commons Attribution-ShareAlike License 3.0).
Cover foreground: (Front) Bright-field optical micrographs of avalanche-mode silicon light-emitting diodes studied in this thesis, and their electroluminescent spectra. (Back) FDTD simulated electric field profile in a superjunction diode (*left*), magnetic field profiles showing waveguiding via silicon-on-insulator and silicon nitride layers in a monolithic optocoupler (*right*).

ISBN 978-90-365-4413-9
DOI 10.3990/1.9789036544139
http://dx.doi.org/10.3990/1.9789036544139

# Avalanche-mode silicon LEDs for monolithic optical coupling in CMOS technology

## Proefschrift

ter verkrijging van
de graad van doctor aan de Universiteit Twente,
op gezag van de rector magnificus,
prof. dr. T.T.M. Palstra,
volgens besluit van het College voor Promoties
in het openbaar te verdedigen
op woensdag 8 november 2017 om 16.45 uur

door

Satadal Dutta

geboren op 31 oktober 1990
te Barrackpore, West Bengal, India

Dit proefschrift is goedgekeurd door:

| | | |
|---|---|---|
| prof. dr. | J. Schmitz | (promotor) |
| dr. ir. | R.J.E. Hueting | (co-promotor) |
| dr. ir. | A.J. Annema | (co-promotor) |

To my Parents, and sister
whose support and sacrifices define the existence of this thesis

*"It is in the admission of ignorance and the admission of uncertainty that there is a hope for the continuous motion of human beings in some direction that doesn't get confined, permanently blocked, as it has so many times before in various periods in the history of man."*

(Richard P. Feynman)

# ABSTRACT

Complementary Metal-Oxide-Semiconductor (CMOS) integrated circuit (IC) technology is the most commercially successful platform in modern electronic and control systems. So called "smart power" technologies such as Bipolar CMOS DMOS (BCD), combine the computational power of CMOS with high voltage transistors (~ 20-100 V) to enable the monolithic integration of advanced smart power applications used in e.g. automotive (car) applications, digital audio amplifiers, and integrated analog-digital systems. Many of such systems require data communication or signal transfer with galvanic isolation, for safety and interference reasons or to interface between low voltage digital parts and high voltage (power) components on an IC. Galvanic isolation is nowadays typically realized with discrete optocouplers, transformers, or integrated capacitive couplers; transformers being bulky and only operating at high (RF) frequencies. Optocouplers transfer signals optically across a galvanically isolated channel. They can be operated for a wide range of data rates (including DC), and are less prone to external electromagnetic interference. Discrete optocouplers (having infrared optical sources) not only have a big form factor, but also have limited operating speeds (~ kHz). Monolithic integration of such optocouplers in CMOS ICs require research and development of suitable light emitters and light detectors for an energy efficient, high speed, and cost effective operation of the system.

This PhD thesis covers two broad aspects. Firstly, it deals with the physics, design, and analysis of efficient light emitting diodes (LEDs) in silicon CMOS technology. Silicon LEDs conventionally emit infrared light (~ 1100 nm), which is not compatible with the spectral detection efficiency of silicon photo-detectors. This is because silicon can efficiently detect light having wavelengths of less than ~ 1000 nm. Therefore the focus is on a specific design solution to this problem, where the LED is biased in "avalanche breakdown". In this situation, there exists a high electric field in the device, which is responsible for light being emitted at shorter wavelengths (400 nm-900 nm). Such an emission, if properly guided laterally across the CMOS IC, would be detected by a silicon photodiode with a relatively high quantum efficiency.

Secondly, this thesis analyzes the feasibility of realizing a monolithic

optocoupler (also referred to an optical link) using silicon LEDs in a BCD silicon-on-insulator (SOI) CMOS technology, from a device physics viewpoint. The optical coupling is treated as a conversion process from electrons to photons (in the LED) and back again to electrons (in the detector). Analysis is done from the viewpoint of coupling quantum efficiency (a figure of merit defined in this thesis), where also the effect of parasitic thermal coupling across such a link due to high power dissipation in the avalanche-mode LED has been considered. Optical propagation via built-in waveguides in SOI technologies is also studied using finite difference time-domain (FDTD) simulations in a technology computer-aided design (TCAD) software tool that is suitable for opto-electronic devices. The analysis of this optocoupler is aimed at integrating avalanche-mode LEDs, which have the potential to be driven at high speeds (~ GHz), with single-photon sensitive optical detectors (e.g. using SPADs). These CMOS-compatible detectors have a relatively low leakage current, and operate in Geiger-mode, to compensate for the low output optical power of the silicon LED at the transmitter side.

This thesis is divided into 7 chapters in total comprising an introductory chapter and a concluding chapter that summarizes the main results, the original contributions of this work, and future recommendations. The rest of the 5 chapters are each based on work performed throughout this PhD research, and published in peer-reviewed journals and presented at conferences.

# SAMENVATTING

De Complementaire Metaal-Oxide-Halfgeleider (CMOS) geïntegreerde netwerk (IC) technologie is de meest succesvolle platform voor moderne elektronische en regelsystemen. Zogenaamde "smart power" technologieën zoals BCD, combineren de rekenkracht van CMOS met hoogspanning-transistoren (~ 20-100 V) om monolithische integratie van geavanceerde smart power toepassingen mogelijk te maken in bijvoorbeeld automobiel toepassingen, digitale audio versterkers en geavanceerde analoog-digitale systemen. De meerderheid van zulke systemen vereist datacommunicatie of signaaloverdracht met de juiste galvanische isolatie voor veiligheid en interferentie tussen laagspanning digitale en hoogspanning (vermogen) componenten op een IC. Tegenwoordig wordt galvanische isolatie toegepast doormiddel van discrete "optocouplers", transformatoren of geïntegreerde capacitieve koppelingen. Transformatoren kosten veel oppervlakte (ze zijn volumineus) en ze functioneren alleen bij hoge (RF) frequenties. De "optocouplers" koppelen optische signalen over een galvanisch geïsoleerde aansluiting. Ze kunnen functioneren over een groot bereik in bitsnelheid, en worden minder beïnvloed door externe elektromagnetische interferenties. Discrete "optocouplers" kosten niet alleen veel oppervlakte maar ze hebben ook een lager bereik in snelheid (vanwege de lage schakelsnelheid van infrarood LEDs). Voor de monolithische integratie van dergelijke "optocouplers" in CMOS ICs is er onderzoek en ontwikkeling noodzakelijk aan licht-emitterende en licht-detecterende silicium componenten wegens een kost-effectieve en energie-efficiënte werking van het systeem.

Dit doctoraal proefschrift betreft twee brede onderwerpen. Ten eerste focusseert het zich op de natuurkunde, het ontwerp en analyse van licht-emitterende dioden (LEDs) in silicium CMOS technologie. Silicium LEDs zenden gewoonlijk infrarood licht uit (~ 1100 nm) dat niet verenigbaar is met de spectrale detectie-efficiëntie van silicium licht-detectoren. De oorzaak daarvan is dat silicium alleen licht met korte golflengtes (lager dan ~ 1000 nm) kan detecteren. Daarom focusseren we ons op een specifieke oplossing waarin de LED ingesteld is op "lawine doorslag". In zo'n situatie, ontstaat er een hoog elektrisch veld binnen de diode waardoor er een stoot-ionisatie stroom gevormd wordt en vervolgens licht met kortere golflengtes (400 nm-900 nm) wordt uitgezonden. Als dit licht op een juiste manier door de CMOS IC geleid wordt, kan het gedetecteerd worden met

een redelijk hoge kwantum efficiëntie.

Ten tweede analyseert dit proefschrift de uitvoerbaarheid van een monolithische "optocoupler" via silicium LEDs in een BCD "silicon-on-insulator" (SOI) CMOS technologie met een nadruk op halfgeleider-natuurkunde. De optische signaaloverdracht wordt uitgelegd als de werkwijze waarin elektronen omgezet worden in fotonen (in de LED) en daarna terug omgezet worden in elektronen (in de fotodiode). Er is een analyse uitgevoerd met een nadruk op de "coupling quantum efficiency", waar bovendien de invloed van de parasitaire thermische koppeling op de efficiëntie ook meegenomen is vanwege de typische hoog-vermogen afvoer in de lawine LED. De optische voortplanting via een ingebouwde golfgeleider in SOI technolgie is ook bestudeerd met behulp van numerieke simulatie in een TCAD software omgeving die geschikt is voor opto-elektronische componenten. De analyse van deze "optocoupler" focusseert op de integratie van lawine LEDs (die ook met hoge snelheden bediend kunnen worden) met fotodiodes die enkele fotonen kunnen opsporen (bijvoorbeeld SPADs). Deze bijzondere (toch CMOS-vriendelijk) lawine fotodiodes hebben een lage lekstroom en functioneren in zogenaamde "Geiger-modus" om het lage-optische vermogen uit de silicium LED in de zender te compenseren.

Dit proefschrift is verdeeld in totaal zeven hoofdstukken. Het omvat een inleidende en afsluitende hoofdstuk. Het afsluitende hoofdstuk bestaat uit een overzicht van de belangrijke conclusies, de oorspronkelijke bijdragen van dit proefschrift en aanbevelingen voor de toekomst. De overige vijf hoofdstukken zijn gebaseerd op het werk dat uitgevoerd was tijdens dit onderzoek en ook gepubliceerd werden in gedegen wetenschappelijke tijdschriften en gepresenteerd werden in conferenties.

# Contents

1 Introduction · 3
*1.1 A brief history of "opto-coupling"* · 4
*1.2 Modern advances and applications* · 5
*1.3 Challenges in design of a monolithic Si optical link* · 7
*1.4 Significance of avalanche-mode LEDs* · 8
*1.5 Thesis outline* · 11

Bibliography · 13

2 Modeling the electroluminescence of avalanche-mode Si $p^+n$ junctions · 17
*2.1 Introduction* · 18
*2.2 Impact ionization and avalanche breakdown* · 18
*2.3 Light emission from avalanche breakdown in silicon* · 22
*2.4 Opto-electronic model* · 24
*2.5 Model validation from experiments* · 31
*2.6 Conclusions* · 39

Bibliography · 41

3 Optical power efficiency of CMOS avalanche-mode silicon LEDs · 45
*3.1 Introduction* · 46
*3.2 Opto-electronic model revisited* · 47
*3.3 Experimental results* · 49
*3.4 Conclusions* · 56

Bibliography · 57

4 The Avalanche-Mode Superjunction Light Emitting Diode · 59
*4.1 Introduction* · 60
*4.2 Theory and Design of Device* · 60
*4.3 Analysis and Results* · 63
*4.4 Conclusions* · 74

Bibliography · 77

5 MONOLITHIC OPTICAL LINK IN SOI-CMOS TECHNOLOGY · 79
*5.1 Introduction* · 80
*5.2 Architecture and layout* · 81
*5.3 LED: electrical and optical behavior* · 83
*5.4 PD: photovoltaic behavior* · 84
*5.5 Coupling efficiency and waveguide in FM LED operation* · 87
*5.6 Coupling efficiency and waveguide in AM LED operation* · 89
*5.7 Heating in the AMLED and thermal coupling* · 91
*5.8 Discussion and design recommendations* · 98
*5.9 Conclusions* ·100

BIBLIOGRAPHY ·103

6 WIDE-SPECTRUM OPTICAL WAVEGUIDING IN SOI-CMOS TECHNOLOGY ·107
*6.1 Introduction* ·108
*6.2 Geometrical conditions for waveguiding* ·109
*6.3 Spectral transmission efficiency* ($\eta_t$) ·113
*6.4 Discussion and implications* ·121
*6.5 Conclusions* ·123

BIBLIOGRAPHY ·125

7 SUMMARY & RECOMMENDATIONS ·127

BIBLIOGRAPHY ·133

A OPTO-ELECTRONIC MODEL PARAMETERS ·135

B EXPERIMENTAL STUDY ON THE EL-SPECTRAL RIPPLES: BACK-END INTERFERENCE ·137
*B.1 Method I: Spectral photocurrent technique* ·138
*B.2 Method II: Surface reflectance technique* ·140

C EQUIVALENT THERMAL MODEL OF THE SOI OPTICAL LINK AND FIT PARAMETERS ·143

# Note to the reader

The chapters numbered two to five are expanded versions of peer-reviewed publications. They have been ordered in this thesis in a way that suits the flow for the general reader; from device modeling to design, optimization, and finally to application. This order does not necessarily match the chronological order in which they were published. In addition, because of being an expanded independent publication, each of these chapters contains its own introduction and has an independent definition of variables and parameters, which have been duly defined in each chapter. The reader is thus not bound to read all the chapters preceding the one he/she is particularly interested in. However, for a reader who is not properly acquainted with the topic, it is recommended to read the chapters in order. Also note that chapters 4 and 5 contain multimedia objects (animations), which are only available in the electronic version of the thesis.

Satadal Dutta
29$^{th}$ Sept. 2017.

# CHAPTER 1

# INTRODUCTION

**Abstract**

This chapter presents the motivation and objectives of this research. A brief historical perspective of opto-coupling is given, and prior work in this field is discussed, followed by an introduction to avalanche-mode silicon light-emitting diodes. State-of-the-art applications are also suggested. Finally, the chapter concludes with an outline of the subsequent chapters of the thesis.

*"No problem can be solved from the same level of consciousness that created it."*

(Albert Einstein)

## 1.1 A brief history of "opto-coupling"

Light as a form of energy, propagating at incredibly large speeds has baffled scientists and explorers since time immemorial. The first quantitative estimate of the finite time taken by sunlight to reach the Earth can be seen in the work of the Indian scholar Sayana in the ancient "Rig Veda". It is also known that Archimedes used mirrors to focus light on distant enemy ships to set them on fire [1]. In the modern era, i.e. post-Renaissance, Galileo is one of the well-known pioneers for his attempt to use light from lanterns as a way to signal information between two hill tops, although his motivation was to measure the speed of light [2]. The idea behind using light as a form of energy to exchange information dates back to the late nineteenth century, when flashing dots and dashes from a lantern was put to practice by Philip Colomb, Vice Admiral in the British Royal Navy to communicate with other ships and harbors [3] (Fig. 1.1). Ever since, optical communication has remained ubiquitous for decades to follow. Even today, flashlights and firecrackers are used as an optical way of sending out distress signals from the middle of the ocean.

Although the fundamental research on optics continued to flourish under the leadership of Newton, Huygens, Fresnel and others, the real momentum in the research of optical links gathered in the beginning of the twentieth century, when the interaction between light and matter became the focal point for engineers and physicists, especially in the context of solid-state devices. The discovery of electroluminescence (EL) from silicon carbide crystal in 1907 [4], the invention of the first light-emitting diode (LED) by the Russian inventor Oleg Losev [5], and the invention of the first solid-state phototransistor by Dr. John N. Shive at Bell Labs [6] provided the needed trigger. It should be noted that the photovoltaic effect was already long known beforehand (discovered by H. Bacquerel in 1839 [7]).

Probably the first ever reported experiment of using rudimentary solid-state light-emitting and light-detecting devices to enable non-radio communication across a short distance, was done by Rubin Braunstein of the Radio Corporation of America in 1957, soon after his report on infrared emission from gallium arsenide (GaAs) diodes [8] (Fig. 1.1). As noted by Kroemer [9], " *Music emerging from a magnetic record player was used via suitable electronics to modulate the current in a GaAs diode. The emitted light was detected by a lead sulphide (PbS) diode some distance away. This signal was fed into an audio amplifier and played back by a loudspeaker. Intercepting the beam stopped the music*". By 1961, Texas Instruments demonstrated efficient optical coupling between a GaAs p-n junction LED and a "galvanically isolated" semiconductor-photodiode [10].

## 1.2 Modern advances and applications

With the upsurge in silicon (Si) based transistors and ICs in the 1960s, the spotlight in the technology of information processing fell on transistors with rapid miniaturization, low cost of fabrication, and fast operation being the driving forces. When it came to optics, Si took a back seat. Being an indirect band gap semiconductor, it is a poor light emitter, unlike the other popular III-V semiconductors like GaAs [11]. Integration of these materials with Si technology has been a major roadblock ever since owing to technological challenges and to compete with costs. III-Vs went to niche markets, while Si CMOS took the lion's share in electronic applications due to the economic advantage of scaling. For some time, therefore there has been a technological divide between the electronic and optical research community, until the CMOS industry faced the increasing importance of "More-than-Moore" integration [12], and an increasing demand on bandwidth and power density. Consequently, development of more efficient light sources and detectors compatible with Si CMOS technology emerged strongly in the quest of integrating photonic functionalities, in particular optical interconnects in CMOS technology [13, 14].

Of specific interest are the so-called "smart power" integrated circuit (IC) technologies such as Bipolar-CMOS-DMOS (BCD) [15], that combine standard CMOS with high voltage transistors to enable monolithic integration of power applications with low voltage digital functionality. This is used, for instance in automotive applications, digital audio amplifiers and highly integrated analog-digital systems. Rigorous integration poses a challenge in interfacing between different sections of the electronic system that operate in widely varying voltage levels; communication between them is desired while maintaining full galvanic isolation. Traditionally this is done with on-chip capacitive couplers [16], or transformers [17, 18], both of which suffer from a trade-off between speed and area on the chip. Transformers are bulky and can only be integrated cost-efficiently for RF frequencies. On-chip communication is a microscopic analogue of two ships (circuit blocks) trying to communicate in the sea (Si chip). A crew member (electron) swimming back and forth as the messenger is time-consuming. Message can also be passed on by creating huge splashes in the water or sending sound waves (phonons), which are still slow and require a lot of power. Moreover, mechanical or acoustic disturbances can be harmful for the ship's course and cause interference. Light could help as the messenger in this scenario just like in the good old days. In a chip, not only it travels fast, but it is also far less susceptible to interference with analog signals in the RF or microwave range in modern electronic communication systems. Thus, arises the following curiosity: can we downsize a set-up like the one demonstrated by Braunstein [8] into modern Si microelectronic chips? This leads to the quest for monolithic integration of optical links in CMOS. In

short, monolithically integrated optical links cater to high speed transceiver [19] applications, and to smart-power applications where data needs to be transferred between galvanically isolated voltage domains [20, 21].

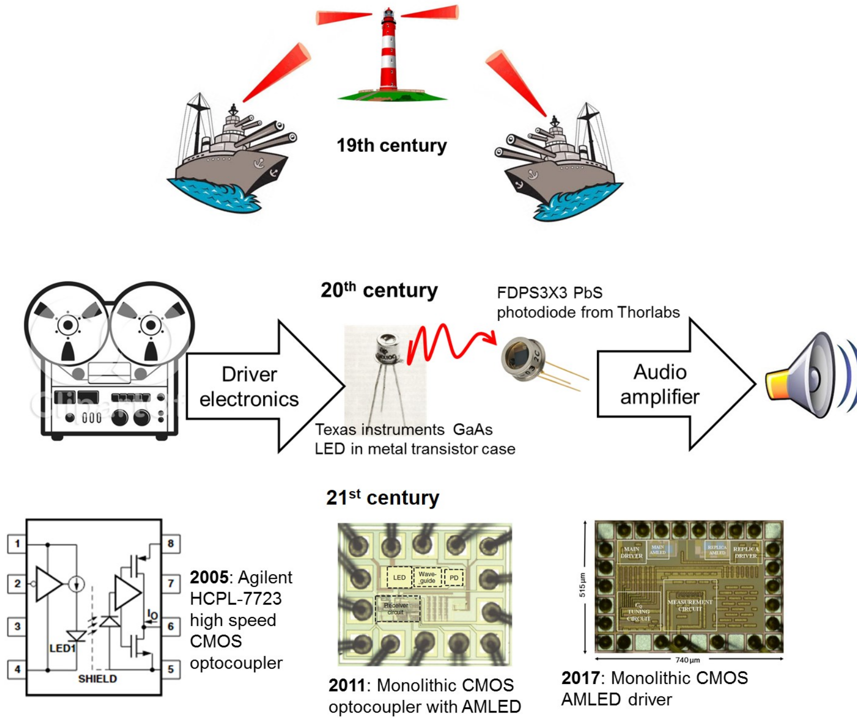


Figure 1.1: A brief overview of the evolution in the applications of optical data transfer.

In electronics, an optocoupler (also called as opto-isolator) is a component that transfers electrical signals between two isolated circuits using light. It prevents high voltages from affecting the low voltage parts of the system. Such a component contains a source (emitter) of light (conventionally a near infrared LED), that converts electrical input signal into light, a closed or guided optical channel, and a photodetector, which converts the light back to electrical energy either directly or by modulating the current from an external power supply. Till date commercial discrete optocouplers are available (e.g. the 4N25 family from Vishay Semiconductors), that combines a GaAs infrared LED and Si phototransistor. Due to the large form factor, although the galvanic isolation is ~ 5 kV, it suffers from large delay times (~ 2 μs) and parasitics. Prior art reported monolithic variants of optocouplers using forward biased Si LEDs [22] and those using avalanche mode Si LEDs in a 0.8 μm [23], 0.35 μm [5, 6], 2 μm [26] and 3 μm [7] bulk CMOS technology with limited galvanic isolation. High isolation voltages (~ 3 kV) have been reported [28], however in an organic opto-coupler

which is not compatible with standard CMOS technology, and a maximum on-off keying speed of only 70 kHz was reached. SOI technology also offers monolithic waveguiding, which has shown potential applications in high-level hybrid integration for cost-effective high-performance computing [29, 30]. Significant advances have been made to integrate optical data communication in the past, but most of them utilized hybrid solutions for inter-chip data transfer [19, 30].

## 1.3 Challenges in design of a monolithic Si optical link

The feasibility of any optical link can be broken down to the individual performance of its three components: the LED, the optical channel (preferably a waveguide), and the photo-detector (see Fig. 1.2). Here lies one fundamental challenge. Although Si is well suited for the implementation of passive optical components such as waveguide and filters at telecommunication wavelengths ($\lambda \geqslant$1550 nm), due to desirably low absorption [31], it is less suited as a light source [11]. Its indirect band gap of 1.12 eV, leads to photon-emission in the infrared (IR) range ($\lambda \geqslant$ 1100 nm) at EL efficiencies (or, internal quantum efficiencies) [32, 33] as high as 0.1% to 1%. Si photo-detectors (PDs) are relatively insensitive [34–36] to these wavelengths. To enable optical links in Si based electronics [37], there must be an appreciable overlap between the spectral responsivity of the photo-detector and the EL-spectrum of the light emitter (see Fig. 1.2).

From a physics point-of-view, one might wonder if it is possible to improve this spectral overlap between the LED and the PD. One way is to red-shift the spectral responsivity by incorporating SiGe based PDs [38, 39], requiring expensive process modifications. The other way is to make the Si LED emit at shorter wavelengths. Techniques such as quantum confinement (Si nanocrystals [40, 41]), rare-earth metal doping [42], cavity LEDs [43] etc. can meet this requirement at the cost of technological complexity. So far, many research groups came up with hybrid solutions, for e.g. to integrate III-V compound semiconductors in CMOS technology [14, 44], which is however, technologically expensive and complex. For example, in 2015, C. Sun et al. published in Nature Communications, reporting an integrated optical interconnect serving as the interface between a processor and digital memory [45]. This was, however realized by modifying the CMOS technology to integrate passive optical components (filters, splitters etc.) coupled to an off-chip high power red laser source. For smart power applications requiring intra-chip data transfer, these existing solutions are not only technologically complex and expensive, but also demand a substantial share of power. A rather simple, yet interesting, way to implement Si LEDs emitting shorter wavelengths ($\lambda <$ 900 nm) in standard CMOS is to operate an Si p-n junction in avalanche breakdown, which is the crux of

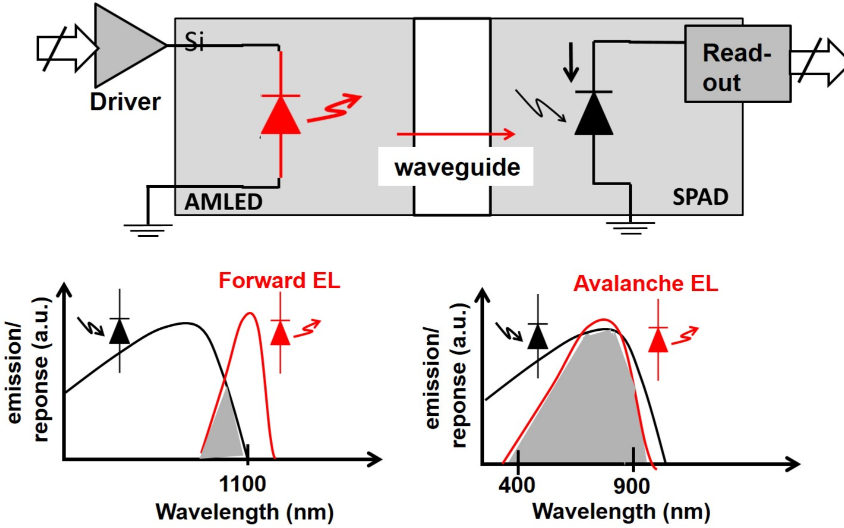


Figure 1.2: (Top): A schematic overview of a basic optocoupler system comprising a light-emitting diode (LED), optical channel (waveguide), and a photodetector (PD). Depending on the mode of operation, the LED and the PD also needs to be interfaced with a suitable driver and read-out circuitry respectively. (Bottom): Schematic plots to illustrate the concept of spectral overlap between the irradiance of the Si LED and the responsivity of the Si PD, the LED being biased in either forward or in reverse bias (avalanche breakdown).

this thesis. This is introduced in the next section.

An additional challenge that creeps in when using short wavelengths for optical coupling in a Si chip is efficient lateral propagation (waveguiding) of light across the Si chip. With link lengths beyond ~ 10 μm, Si can no longer serve as a viable medium to transport photons from the LED to the detector within a single chip due to its high absorption. Thus, from the purview of standard CMOS technology, inter-metal dielectric layers in the back-end (e.g. silica, silicon nitride) and device isolation layers such as the shallow trench isolation (STI) are potential candidates to be employed as low-attenuation paths for photons with $\lambda < 900$ nm. Silicon is viable for optical propagation for link lengths beyond ~ 10 μm only when $\lambda > 900$ nm. This thesis discusses the waveguiding capabilities in the context of SOI-CMOS technology in Chapter 6.

## 1.4 Significance of avalanche-mode LEDs

The phenomenon that an Si p-n junction emits visible light when biased in reverse breakdown was first reported by Newman in 1955 [46]. His work was soon followed by Wolff, Chynoweth, McKay and others [13, 47–52] who also made significant efforts to describe the physics behind such wide-spectrum electroluminescence (EL) from Si and Ge, encompassing

wavelengths much shorter than what is expected from conventional band-edge (or band-to-band) recombination (that happens in forward biased diodes). The basic principle behind this phenomenon is to accelerate the charge carriers in a semiconductor (namely electrons and/or holes) to energies in excess of the band gap, via a high reverse electric field applied to the junction leading to avalanche breakdown. At breakdown, there is a net generation of charge carriers via impact ionization. However, via recombination events a certain fraction of these energetic carriers subsequently undergo higher energy transitions leading to a broad EL-spectrum peaking at shorter wavelengths (in the 600-700 nm range). This spectrum enhances the overlap with the responsivity of an Si PD (see Fig. 1.2). As yet another advantage, avalanche-mode (AM) operation has previously been reported to exhibit high modulation speeds (~ 20 GHz) [50]. Fig. 1.3 shows a brief overview of AMLEDs designed and reported in the past decades.



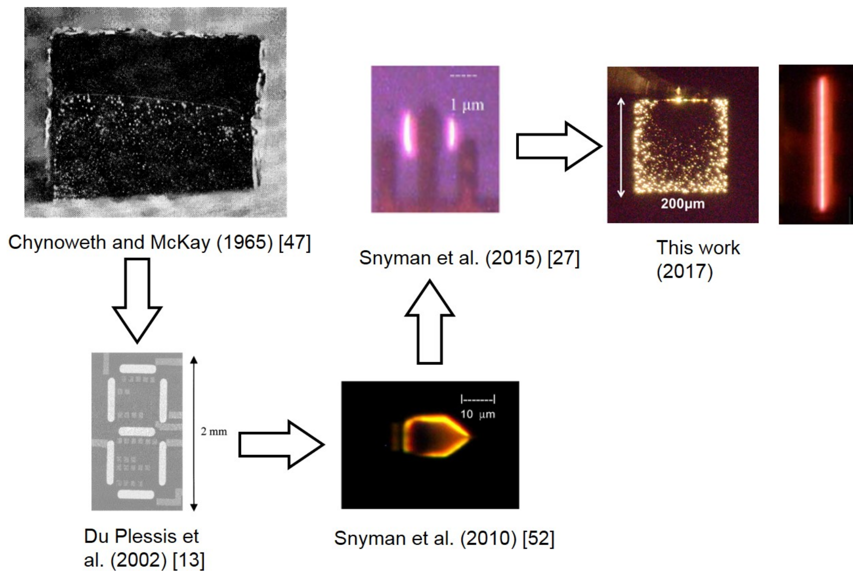


Figure 1.3: Examples of bright-field optical micrographs of avalanche-mode silicon p-n junctions, over the past few decades.

There are mainly two challenges while dealing with such LEDs. Firstly, since the junction has to be biased at relatively high voltages. If operated for long "on" durations, this can result in a high time-averaged electrical power leading to self-heating and parasitic thermal coupling. A robust (to temperature, process, and bias variations), and power-efficient operation of such LEDs therefore requires smart design of the CMOS driver circuitry. Although this thesis does not delve into details of (integrated) circuit design, it deserves mention that such a driver circuit has been recently demonstrated [53] during our collaborative project (Optocoupling-in-CMOS) in a 140 nm silicon-on-insulator (SOI) CMOS technology [15]. The driver works

on a self-quenched principle to control the amount of charge fed to the AMLED. This ensures that just a sufficient number of photons are emitted to operate an optical link without wasting electrical power. This technique is also expected to be beneficial for the device reliability.

Secondly, the internal quantum efficiency of the AMLED is low ($\sim 10^{-5}$) [51]. This can have a major impact in limiting the signal-to-noise (SNR) ratio during data transfer. Consider a system where an LED is used to transmit bits to a PD based receiver, with the LED sustaining an on-state current $I_{LED}$ for a duration of $t_{ON}$ in each data bit. Note that $t_{ON}$ depends on the data encoding scheme employed. For e.g. during on-off keying with non-return zero (NRZ) encoding [54], $t_{ON} = T_{bit}$, while in Manchester encoding [54] $t_{ON} = T_{bit}/2$ where $T_{bit} = f_s^{-1}$ being the bit duration (inverse of data rate $f_s$). The number of charge carriers (say electrons) injected per bit into the LED is therefore [53]:

$$Q_b = I_{LED} \cdot t_{ON} = \frac{E_b}{V_{bias}}, \tag{1.1}$$

where $E_b$ is the energy per bit and $V_{bias}$ is the LED bias voltage required to sustain $I_{LED}$. Let us now assume that photon emission from the LED occurs with an internal quantum efficiency $\eta_e$, that photon propagation from the LED to the PD occurs with an efficiency $\eta_p$, and that photon detection in the PD occurs with an internal quantum efficiency $\eta_d$. Then, the time-averaged PD current (signal received) can be written as [53]:

$$I_{PD} = f_s Q_b \eta_e \eta_p \eta_d. \tag{1.2}$$

Considering shot noise to be the main contributor of noise at high frequencies in semiconductors [29], the signal-to-noise ratio (SNR) for a bandwidth of $f_s$ can be written as

$$SNR = 10 \cdot \log \left[ \frac{I_{PD}^2}{2qI_{PD}f_s} \right]. \tag{1.3}$$

Combining Eq. (1.2) and Eq. (5.9), and using the relation $E_b = Q_b \cdot V_{bias}$ we obtain

$$SNR = 10 \cdot \log \left[ \frac{E_b \eta_e \eta_p \eta_d}{2qV_{bias}} \right]. \tag{1.4}$$

Eq. (1.4) indicates, in simple terms, the dependency between SNR and the internal quantum efficiency of the LED. Although $\eta_e$ in avalanche-mode operation is low, the $\eta_d$ is roughly 2 orders of magnitude higher for visible wavelengths (emitted by an avalanche mode Si LED) as compared to IR wavelengths (emitted by a forward biased Si LED). For a higher $\eta_e \cdot \eta_p \cdot \eta_d$, the same SNR can be achieved for a lower $E_b$ thus lowering the power consumption. Thus, the challenges with an AMLED based optical

link design are mainly two-fold: reducing $V_{bias}$ (close to the breakdown voltage $V_{BR}$) to increase the optical power efficiency, and increase $\eta_e$, $\eta_p$, and $\eta_d$. This thesis deals with these challenges.

One particular CMOS-compatible way to compensate for the low AMLED intensities (and therefore to boost the SNR) is to use highly sensitive PDs, for e.g. Geiger-mode avalanche diodes or Single Photon Avalanche Diodes (SPADs) [28, 35, 57], which exploit the intrinsic phenomenon of avalanche multiplication in a reverse biased diode triggered by photogenerated charge carriers. This provides a big leverage from the viewpoint of SNR in a communication system with fewer transistors, in turn crucial for low bit error rates and higher speeds. In addition, AM EL has recently been utilized by the power electronic device community to set up an optical imaging technique, which helps in studying device reliability in high electric fields without permanent device failure [58]. These topics are well described in literature and prior theses [57, 59], and are not treated in detail in this work.

This thesis broadly deals with the modeling, design, characterization of AM LEDs in Si, and the physical aspects of their monolithic integration to make an optical link in industrial Bipolar CMOS DMOS (BCD) SOI technology. It also touches upon optical propagation mechanisms and scaling properties of such a link from a device-physics viewpoint. The subsequent chapters are outlined in the following section.

## 1.5 Thesis outline

- **Chapter 2:** *Modeling the electroluminescence of avalanche-mode Si $p^+n$ junctions*, based on work published in the Journal of Applied Physics, 2015. This chapter describes an opto-electronic model to derive the relative spectral irradiance and the optical intensity in avalanche breakdown using the electrical bias as an input parameter.

- **Chapter 3:** *Optical power efficiency of CMOS avalanche-mode silicon LEDs*, based on work published in IEEE Electron Device Letters, 2017. This chapter describes the experimental and modeled relationship between the optical power efficiency and breakdown voltage, and subsequently the electric field profiles in different Si diode designs.

- **Chapter 4:** *The Avalanche-Mode Superjunction Light Emitting Diode*, based on work published in IEEE Transactions on Electron Devices, 2017. This chapter presents a novel device design to improve the efficiency of Si AMLEDs adopting field-profile engineering via the well-known Reduced Surface Field (RESURF) effect in a 140 nm SOI CMOS technology.

- **Chapter 5:** *Monolithic optical link in SOI-CMOS technology*, based on work presented at the Conference on Lasers and Electro-Optics

(CLEO), 2016, and later published in Optics Express, 2017. In this chapter an SOI based optical link is presented using standard p-n junction diodes, and having galvanic isolation.

- **Chapter 6:** *Wide-spectrum optical waveguiding in high-voltage SOI-CMOS technology*, based on a publication in the proceedings of the International Conference on Numerical Simulation of Optoelectronic Devices (NUSOD) 2017. This chapter studies the waveguiding capabilities of SOI CMOS technology using numerical raytracing and finite difference time-domain simulations.

- **Chapter 7:** *Summary & Recommendations*, which provides a summary of the important conclusions presented in the aforesaid chapters, followed by recommendations for future work. Finally, a list of the original contributions of this thesis is provided.

# BIBLIOGRAPHY


[1] "Archimedes' Weapon," Time Magazine, Nov. 1973.

[2] A. Al-Azzawi, "*Light and Optics Principles and Practices*," (CRC Press, Taylor & Francis Group, 2006).

[3] C.H. Sterling, "Military communications: From ancient times to the $21^{st}$ century," (ABC-CLIO Inc., 2008).

[4] H.J. Round, "A note on carborundum," Electrical World, no. 19: 309, 1907.

[5] O.V. Losev, "Telegrafiya i telefoniya bez provodov," no. 44: 485-494, 1927.

[6] M. Riordan, and L. Hoddeson, "Crystal Fire: The Invention of the Transistor and the Birth of the Information Age," 1998.

[7] W. Palz, "Power for the World-The Emergence of Electricity from the Sun," (Belgium: Pan Stanford Publishing, 2010).

[8] R. Braunstein, "Radiative transitions in semiconductors," Phys. Rev., vol. 99, no. 6, pp. 1892-1893, 1955.

[9] H. Kroemer, "The double-heterostructure concept: how it got started," Proc. of the IEEE, vol. 101, no. 10, pp. 2183-2187, 2013.

[10] J.R. Biard, E.L. Bonin, W.N. Carr, and G.E. Pittman, "GaAs infrared source," IEEE International Electron Devices Meeting (IEDM) Tech. Digest, vol. 8, pp. 96, 1962.

[11] E.F. Schubert, "Light Emitting Diodes," Cambridge University Press, 2006.

[12] W. Arden, M. Brillouët, P. Cogez, M. Graef, B. Huizing, and R. Mahnkopf, "More-than-Moore," White Paper. [Online]. Available: http://www.itrs.net/Links/2010ITRS/IRC-ITRS-MtM-v2%203.pdf

[13] M. du Plessis, H. Aharoni, and L.W. Snyman, "Silicon LEDs fabricated in standard VLSI technology as components for all silicon monolithic integrated optoelectronic systems," IEEE J. Sel. Topics Quantum Electron., vol. 8, no. 6, pp. 1412-1419, 2002.

[14] D.A.B. Miller, "Device requirements for optical interconnects to silicon chips," Proc. of the IEEE, vol. 97, no. 7, pp. 1166-1189, 2009.

[15] P. Wessels, M. Swanenberg, H. van Zwol, B. Krabbenborg, H. Boezen, M. Berkhout, and A. Grakist, "Advanced BCD technology for automotive, audio and power applications," Solid-State Electronics, vol. 51, pp. 195-211, 2007.

[16] E. Culurciello, and A.G. Andreou, "Capacitive inter-chip data and power transfer for 3-D VLSI," IEEE Trans. Circuits and Systems-II: Express Briefs, vol. 53, no. 12, pp. 1348-1352, 2006.

[17] R. Grezaud, F. Ayel, N. Rouger, and J.-C. Crébier, "A gate-driver with integrated deadtime controller," IEEE Trans. Power Electronics, vol. 31, no. 12, pp. 8409-8421, 2016.

[18] K. Gingerich, and C. Sterzik, "The ISO72x family of high-speed digital isolators," Application Report SLLA198, Texas Instruments, 2006.

[19] X. Zheng, D. Patil, J. Lexau, F. Liu, G. Li, H. Thacker, Y. Luo, I. Shubin,J. Li, J. Yao, P. Dong, D. Feng, M. Asghari, T. Pinguet, A. Mekis, P. Amberg, M. Dayringer, J. Gainsley, H.F. Moghadam, E. Alon, K. Raj, R. Ho, J.E. Cunningham and A.V. Krishnamoorthy, "Ultra-efficient 10 Gb/s hybrid integrated silicon photonic transmitter and receiver," Opt. Express, vol. 19, no. 6, pp. 5172-5186, 2011.

[20] N. Rouger, L.T. Le, D. Colin and J.-C. Crébier, "CMOS SOI gate driver with integrated optical supply and optical driving for fast power transistors," Proc. 28$^{th}$ International Symposium on Power Semiconductor Devices (ISPSD), pp. 427-430, 2016.

[21] N. Van-Sang, L. Thang-Long, F. Sarrafin, T. Ngoc-Duc, D. Colin, N. Rouger, P. LeFranc, Y. Lembeye, J-D. Arnould, B. Allard and J-C. Crebier, "Contributions to dedicated gate driver circuitry for very high switching speed high temperature power devices," Proc. 28$^{th}$ International Symposium on Power Semiconductor Devices (ISPSD), pp. 443-446, 2016.

[22] H.-C. Lee and C-K. Liu, "Si-based current-density-enhanced light emission and low-operating-voltage light-emitting/receiving designs," Solid State Electronics, vol. 49, pp. 1172-1178, 2005.

[23] M. Sergio and E. Charbon, "An intra-chip electro-optical channel based on CMOS single photon detectors," IEEE International Electron Devices Meeting (IEDM) Tech. Digest, Paper no. 822, 2005.

[24] B. Huang, X. Zhang, W. Wang, Z. Dong, N. Guan, Z. Zhang, and H. Chen, "CMOS monolithic optoelectronic integrated circuit for on-chip optical interconnection," Opt. Commun., vol. 284, pp. 3924-3927, 2011.

[25] A. Khanmohammadi, R. Enne, M. Hofbauer, and H. Zimmermann, "Monolithic integrated optical random pulse generator in high voltage CMOS technology," Proc. European Solid State Device Research Conference (ESSDERC), pp. 138-141, 2015.

[26] L.W. Snyman, H. Aharoni, A. Biber, A. Bogalecki, L. Canning, M. du Plessis and P. Maree, "Optical sources, integrated optical detectors, and optical waveguides in standard silicon CMOS integrated circuitry," Proc. SPIE, vol. 3953, Silicon-based Optoelectronics II, pp. 20-36, 2000.

[27] K. Xu, B. Huang, K.A. Ogudo, L.W. Snyman, H. Chen, and G.P. Li, "Silicon light-emitting device in Standard CMOS technology," Proc. 8th International Photonics and OptoElectronics Meetings, paper no. OT1C.3, 2015.

[28] D. Li, W. Li, L. Duan, G. Zhang, S. Liu, and G. Dong, "Highly integrable organic optocouplers on a patterned double-side indium tin oxide substrate with high isolation voltage," IEEE Electron Device Lett., vol. 36, no. 2, pp. 171-173, 2015.

[29] R. Dangel, J. Hofrichter, F. Horst, D. Jubin, A. La Porta, N. Meier, I.M. Soganci, J. Weiss, and B.J. Offrein, "Polymer waveguides for electro-optical integration in data centers and high-performance computers," Opt. Express, vol. 23, no. 4, pp. 4736-4750, 2015.

[30] J. Chen, N. Bamiedakis, P. Vasil'ev, T. Edwards, C. Brown, R. Penty, and I. White, "High-bandwidth and large coupling tolerance graded-index multimode polymer waveguides for on-board high-speed optical interconnects," J. Lightwave Tech., vol. 34, no. 12, pp. 2934-2940, 2015.

[31] M.A. Green, "Self-consistent optical parameters of intrinsic silicon at 300 K including temperature coefficients," Solar Energy Materials & Solar Cells, vol. 92, pp. 1305-1310, 2008.

[32] M. Green, J. Zhao, A.Wang, P. Reece, and M. Gal, "Efficient silicon light emitting diodes," Nature, vol. 412, no. 6849, pp. 805-808, 2001.

[33] T. Trupke, J. Zhao, A.Wang, R. Corkish, and M. A. Green, "Very efficient light emission from bulk crystalline silicon," Appl. Phys. Lett., vol. 82, no. 18, pp. 2996-2998, 2003.

[34] B.P. van Drieënhuizen and R.F.Wolffenbuttel, "Optocoupler based on the avalanche light emission in silicon," Sensors and Actuators A, vol. 31, pp. 229-240, 1992.

[35] S. Mandai, M. W. Fishburn, Y. Maruyama and E. Charbon, "A wide spectral range single-photon avalanche diode fabricated in an advanced 180 nm CMOS technology," Opt. Express, vol. 20, no. 6, pp. 5849-5857, 2012.

[36] L. Shi, S. Nihtianov, L. Haspeslagh, F. Scholze, A. Gottwald and L.K. Nanver, "Surface-charge-collection-enhanced high-sensitivity high-stability silicon photodiodes for DUV and VUV spectral ranges," IEEE Trans. Electron Devices, vol. 59, no. 11, pp. 2888-2894,

2012.

[37] L. Rebohle, J. Von Borany, D. Borchert, H. Fröb, T. Gebel, M. Helm, W. Möller, W. Skorupaa, "Efficient blue light emission from silicon," Electrochemical and Solid-State Lett., vol. 4, no. 7, pp. G57-G60, 2001.

[38] S. Luryi, T.P. Pearsall, H. Temkin, and J.C. Bean, "Waveguide infrared photodetectors on a silicon chip," IEEE Electron Device Lett., vol. 7, no. 2, pp. 104-107, 1986.

[39] A.K. Sood, J.W. Zeller, R.A. Richwine, Y.R. Puri, H. Efstathiadis, P. Haldar, N.K. Dhar, and D.L. Polla, "SiGe based visible-NIR photodetector technology for optoelectronic applications," Advances in Optical Fiber Technology: Fundamental Optical Phenomena and Applications, Dr. Moh. Yasin (Ed.), InTech, 2015, doi: 10.5772/59065.

[40] K.S. Cho, N.-M. Park, T.-Y. Kim, K.-H. Kim, G.Y. Sung, and J.H. Shin, "High efficiency visible electroluminescence from silicon nanocrystals embedded in silicon nitride using a transparent doping layer," Appl. Phys. Lett., vol. 86, no. 7, 071 909, 2005.

[41] J. Carreras, J. Arbiol, B. Garrido, C. Bonafos, and J. Montserrat, "Direct modulation of electroluminescence from silicon nanocrystals beyond radiative recombination rates," Appl. Phys. Lett., vol. 92, no. 9, 091103, 2008.

[42] J. Warga, R. Li, S. Basu, and L.D. Negro, "Erbium-doped silicon nanocrystals in silicon/silicon nitride superlattice structures: Light emission and energy transfer," Phys. E, Low-Dimensional Syst. Nanostructures, vol. 41, pp. 1040-1043, 2009.

[43] J. Potfajova, B. Schmidt, M. Helm, T. Gemming, M. Benyoucef, A. Rastelli, and O.G. Schmidt, "Microcavity enhanced silicon light emitting pn-diode," Appl. Phys. Lett., vol. 96, no. 15, 151 113, 2010.

[44] A.W. Fang, H. Park, O. Cohen, R. Jones, M.J. Paniccia, and J.E. Bowers, "Electrically pumped hybrid AlGaInAs-silicon evanescent laser," Opt. Express, vol. 14, no. 20, pp. 9203-9210, 2006.

[45] C. Sun, M.T. Wade, Y. Lee, J.S. Orcutt, L. Alloatti, M.S. Georgas, A.S. Waterman, J.M. Shainline, R.R. Avizienis, S. Lin, B.R. Moss, R. Kumar, F. Pavanello, A.H. Atabaki, H.M. Cook, A.J. Ou, J.C. Leu, Y.-H. Chen, K. Asanović, R.J. Ram, M.A. Popović, and V.M. Stojanović, "Single-chip microprocessor that communicates directly using light," Nature, vol. 528, pp. 534-538, 2015.

[46] R. Newman, "Visible light from a silicon p-n junction," Phys. Rev., vol. 100, no. 2, pp. 700-703, 1955.

[47] A.G. Chynoweth and K.G. McKay, "Photon emission from avalanche breakdown in silicon," Phys. Rev., vol. 102, no. 2, pp. 369-376, 1956.

[48] P.A. Wolff, "Theory of optical radiation from breakdown avalanches in Germanium," J. Phys. Chem. Solids, vol. 16, pp. 184-190, 1960.

[49] J. Shewchun and L.Y. Wei, "Mechanism for reverse-biased breakdown radiation in p-n junctions," Solid-State Electronics, vol. 8, pp. 485-493, 1965.

[50] A. Chatterjee, B. Bhuva, and R. Schrimpf, "High-speed light modulation in avalanche breakdown mode for Si diodes," IEEE Electron Device Lett., vol. 25, no. 9, pp. 628-630, 2004.

[51] L.W. Snyman, M. du Plessis, and H. Aharoni, "Injection-avalanche-based $n^{+}pn$ silicon complementary metal-oxide-semiconductor light-emitting device (450 - 750 nm) with 2-order-of-magnitude increase in light emission intensity," Jpn. Jrnl. Appl. Phys., vol. 46, no. 4B, pp. 2474-2480, 2007.

[52] L.W. Snyman, M. du Plessis and E. Bellotti, "Photonic transitions (1.4 eV–2.8 eV) in silicon $p^{+}np^{+}$ injection-avalanche CMOS LEDs as function of depletion layer profiling and defect engineering," IEEE J. Quantum Electron., vol. 46, no. 6, pp. 906-919, 2010.

[53] V. Agarwal, S. Dutta, A.J. Annema, R.J.E. Hueting, P.G. Steeneken, and B. Nauta, "Low power wide spectrum optical transmitter using avalanche mode LEDs in SOI CMOS technology," Opt. Express, vol. 25, no. 15, pp. 16981-16995, 2017.

[54] A. L-Garcia, and I. Widjaja, "*Communication Networks*," McGraw-Hill Education, 2004.

[55] S.M. Sze and K.K. Ng, "*Physics of Semiconductor Devices*," 3rd edition, John Wiley & Sons, Inc., USA, 2007.

[56] M-J. Lee, P. Sun and E. Charbon, "A first single-photon avalanche diode fabricated in standard SOI CMOS technology with a full characterization of the device," Opt. Express, vol. 23, no. 10, pp. 13200-13209, 2015.

[57] W.J. Kindt, "Geiger mode avalanche photodiode arrays for spatially resolved single photon counting," PhD thesis, TU Delft, 1999 (ISBN 90-407-1845-8).

[58] T. Matsudai, K. Endo, T. Ogura, T. Matsumoto, K. Uchiyama, and K. Koshikawa, "Direct photo emission monitoring for high power IGBT during avalanche operation," Proc. IEEE International Reliability Physics Symposium (IRPS), p. FA-3, 2016.

[59] C. Veerappan, "Single-photon avalanche diodes for cancer diagnosis," PhD thesis, TU Delft, 2016 (ISBN 978-94-6186-620-2).

CHAPTER 2

# Modeling the electroluminescence of avalanche-mode Si $p^+n$ junctions

**Abstract**

This chapter presents the modeling of light emission from silicon based $p^+n$ junctions operating in avalanche breakdown. The photon emission process under the influence of relatively high electric fields in a reverse biased junction ($> 10^5$ V/cm) is discussed. The photon emission rate is described as a function of the electron temperature, which is computed from the spatial distribution of the electric field. The light emission spectra lie around the visible spectral range ($\lambda \sim$ 350-870 nm), where the peak wavelength and the optical intensity are both doping level dependent. The derived physics-based opto-electronic model is validated using experimental data obtained from ultra-shallow $p^+n$ junctions with low absorption through a nm-thin boron-diffused $p^+$ region, formed by a nm-thin pure boron layer on top. A broad peak in the emission spectra between 580 nm and 650 nm is observed for diodes with breakdown voltages of 7 V and 14 V respectively, consistent with the model.

*"When it is not in our power to follow what is true, we ought to follow what is most probable."* (Rene Descartes)

---

This chapter is an extension of a publication in Journal of Applied Physics [1].

## 2.1 Introduction

Silicon (Si) is well suited for the implementation of optical waveguides at telecommunication wavelengths ($\lambda \geqslant$1550 nm), due to its desirably low absorption [2]. However, Si is less suited as a light source [3]. Its indirect band gap ($E_g$) of 1.12 eV, leads to photon-emission in the infra-red (IR) range ($\lambda \geqslant$ 1100 nm) at electroluminescence (EL) efficiencies (or, internal quantum efficiencies) [4, 5] as high as 0.1% to 1%. Si photo-detectors (PDs) are relatively insensitive [6–8] to these wavelengths. To enable optical links in Si based electronics [9], there must be an appreciable overlap between the spectral responsivity of the photo-detector and the EL-spectrum of the light emitter.

Avalanche mode (AM) Si light emitting diodes (LEDs) [10–13] emit light with shorter wavelengths in the visible range [25, 26, 28] more suitable for such optical links. With these AMLEDs, high-speed ($\sim$ 20 GHz) intensity modulation [11] can be achieved, although at a low power efficiency ($\sim 10^{-6}$) [14, 15].

In this chapter, a one-dimensional (1-D) model is presented that describes the optical output of a reverse-biased silicon LED as a function of the applied bias. It is shown that the (non-local) electric field profile, that defines the electron temperature, is the key parameter which determines the spectral distribution of photon emission. This model could be of aid in opto-electronic circuit design.
Section 2.2 briefly reviews the concept of avalanche breakdown. Then, a review of the phenomenon of light emission in avalanche breakdown is given in section 5.2. In section 3.2 the dependency of photon emission rate and hence the optical power on the electrical inputs is expressed. Modifications to prior modeling efforts are proposed, to account for the effect of electric field on the photon-emission spectrum. In section 3.3, our experimental devices and set-up are reported, and the model-predictions are compared with the measured EL-spectra. Finally, in section 6.5, the findings are summarized.

## 2.2 Impact ionization and avalanche breakdown

Reverse biasing a p-n junction leads to the formation of a depletion region as illustrated in Fig. 2.1. Although depleted, at small bias voltages ($V$) some reverse current flow. The reverse current is contributed mainly by diffusion of minority carriers at very low $V$. A second contribution comes from the drift of thermally generated carriers (also optically if photons of suitable wavelength are present) that is proportional to the depletion width $W_{dep}$. This component dominates as $V$ and thereby the electric field $F$ increases in magnitude. Quantitatively, this component is proportional to the trap-density in the depletion region. For relatively high reverse bias

voltages, the mobile charge carriers (electrons and holes) are accelerated by the field. During this process the charge carriers can scatter within the Si lattice producing electron-hole pairs (EHPs) causing carrier multiplication. This mechanism is called impact ionization [16]. Even at a low bias, there is already a small fraction of carriers on the high energy tail of probability distribution, which can cause ionization. But, this is low enough not to dominate over thermal carrier generation. As the reverse bias is further increased, the maximum electric field at the junction increases thereby increasing the amount of mobile charge carriers. Beyond a certain critical value of the field $F_{crit}$, secondary charge carriers in turn generate EHPs.

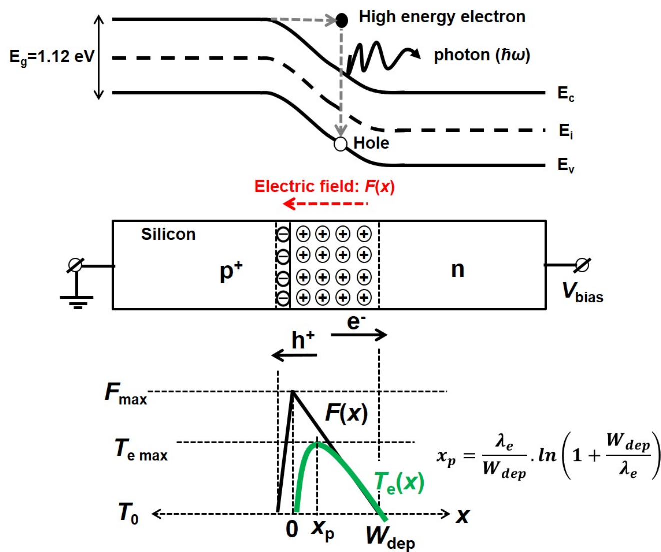


Figure 2.1: An ideal 1-D abrupt p$^+$n junction showing the energy-band diagram ($E_C$, and $E_V$ denote the conduction band minimum and the valence band maximum respectively) and the spatial electric field profile F(x) in the space-charge region. The green curve shows the electron temperature $T_e$ given by Eq. (2.13).

This multiplication produces a domino effect, and the current shoots up by a few orders of magnitude, with a very small change in bias voltage. This is called avalanche multiplication or breakdown, which can be characterized by the breakdown voltage $V_{BR}$, which depends on the doping levels of the p-n junction. The source of charge carriers in a p-n junction is typically the small reverse saturation current attributed to thermally generated EHPs; this generation occurs at a rate independent of the doping levels [16, 17]. In practice, because the high field region is spatially limited, the current doesn't rise infinitely because the multiplication of electrons stops at the end of the high field region. Eventually the current becomes space charge limited [18]. Additionally, the series resistance of the device starts to kick in and limits the avalanche current. The dominant conduction mechanisms in various regimes of the I-V characteristic for a p-n junction

diode are shown schematically in Fig. 2.2. It should be pointed out that in diodes as the doping level (and thereby the electric field) increase, the I-V characteristics is also affected by band-to-band and/or trap-assisted tunneling [19].



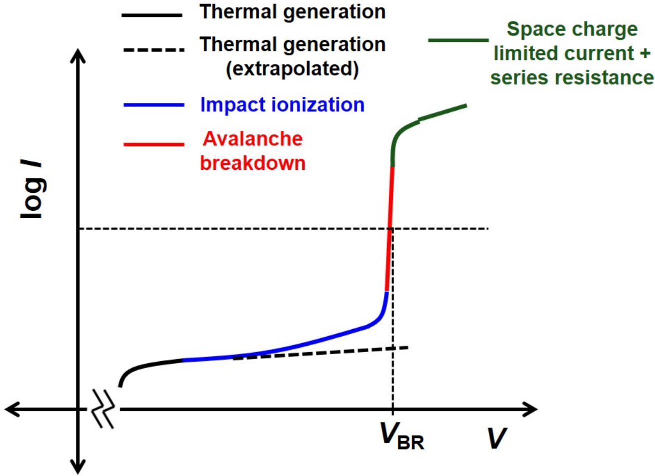


Figure 2.2: Schematic I-V characteristic (on a semi-log scale) of a reverse biased p-n junction, showing the dominant contributor of current in different range of bias voltages. The dashed line is the extrapolated trend considering only thermal generation. Experimentally, the breakdown voltage $V_{BR}$ is defined in the avalanche regime at an arbitrarily chosen current level.

Impact ionization is mathematically described in terms of ionization coefficients. These coefficients represent the average rate of EHP generation per unit length. In Si, the electron and hole ionization coefficients [20] ($\alpha_n$ and $\alpha_p$) are different ($\alpha_n > \alpha_p$). For modeling purposes, the condition for breakdown is however commonly defined by the equating the ionization integral of electrons to unity [17], assuming $\alpha_n = \alpha_p$:

$$\int_0^{W_{dep}} \alpha_n(x)dx = 1, \tag{2.1}$$

where the position $x$ is measured relative to the junction and positive towards the n-side (see Fig. 2.1). $W_{dep}$ is the depletion width on the n-side. The width of depletion region is very thin on the $p^+$ side and hence, can be ignored. The ionization coefficient has been modeled as a function of the local electric field $F(x)$. According to Fulop's approximation [17, 21],

$$\alpha_n(x) = \alpha_0 F^7(x), \tag{2.2}$$

where $\alpha_0$ for Si is $1.8 \times 10^{-35}$ $cm^6V^{-7}$. The choice for this model stems from analytical simplicity.

In this chapter, we consider only a single-sided abrupt $p^+n$ junction, where

the field decreases linearly (Fig. 2.1) from the junction ($x = 0$) to the depletion edge ($x = W_{dep}$) in the lowly-doped region (n-type in our case). The depletion region on the highly doped $p^+$ side is ignored. The critical electric field at breakdown, $F_{crit}$, can be determined by combining equations (2.1) and (2.2) along with the appropriate spatial distribution of electric field in the depletion region. It is assumed that the space-charge region makes a sharp transition to the neutral n-region (depletion approximation). The field in the region $0 \leqslant x \leqslant W_{dep}$ is obtained after solving Poisson's equation [16] as:

$$F(x) = F_{max}\left(1 - \frac{x}{W_{dep}}\right), \tag{2.3}$$

where $F_{max}$ is the peak electric field (see Fig. 2.1).

A simple analytical approximation for $F_{crit}$, i.e. $F_{max}$ at breakdown, can be worked out following Eq. (2.1) while substituting $\alpha_n$ and $F$ from Eq. (2.2), and Eq. (2.3), respectively:

$$F_{crit} \approx \left(\frac{8qN}{\alpha_0 \epsilon_{Si}}\right)^{\frac{1}{8}}, \tag{2.4}$$

where $N$ is the doping level on the n-side, $q$ is the elementary charge, and $\epsilon_{Si}$ is the absolute permittivity of Si, and the following relation between depletion width (at breakdown) and the maximum field at the abrupt junction has been used:

$$W_{dep(crit)} = \frac{\epsilon_{Si} F_{crit}}{qN}. \tag{2.5}$$

Hence, the bias voltage at breakdown ($V_{BR}$), for which $F = F_{crit}$ is :

$$V_{BR} = \frac{\epsilon_{Si} F_{crit}^2}{2qN}. \tag{2.6}$$

In the experiments, the condition 2.1 cannot be used to define $V_{BR}$ due to multiple reasons. Firstly, real devices are never truly 1-D. Secondly, absolute values of the electric field and ionization coefficients are difficult to measure. Thus, we need to define $V_{BR}$ from observable quantities, viz. voltage and current. Experimentally $V_{BR}$ can be defined at a specified current (density), and therefore is not a fixed value [22]. It also has a positive temperature coefficient (PTC) [23]. Fig. 2.3 shows a comparison of the analytical model (Eq. (2.6)), with a numerical one-dimensional (1-D) Technology Computer Aided Design (TCAD) simulation (Sentaurus tool from Synopsys) of an abrupt single-sided junction in Si. Experimental data obtained from our devices (section 3.3) have been indicated as well, showing good agreement. However, for low $V_{BR}$, non-local avalanche plays a role, which is discussed in section 3.2.

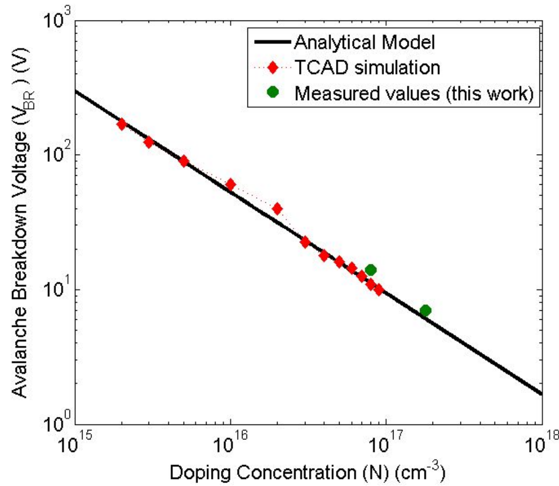


Figure 2.3: Doping dependence of avalanche breakdown voltage for a 1-D abrupt $p^{+}n$ junction: comparison between analytical estimate (Eqs. (2.4), and (2.6)) and TCAD simulation ($T = 300$ K). The measured values in this work are shown by the colored circles (green).

## 2.3 Light emission from avalanche breakdown in silicon

Fig. 2.4 shows a sketch of the energy ($E$)-momentum ($k$) diagram of bulk Si crystal at room temperature, reproduced from the original work of [24], showing its indirect band gap $E_{g1}$ of 1.12 eV. An indirect band gap means that the minimum of the conduction band does not have the same $k$ as the valence band maximum. Hence, there is a momentum mismatch. Photons are emitted when electrons make transitions from the conduction band to the valence band, hence the electrons recombine with holes. Due to the momentum mismatch, such a radiative inter-band recombination has a low probability and requires the help of phonons in the Si lattice, that can account for the required change in momentum $\Delta k$. Note that these phonons also carry a small but finite energy (typically a few meV). In a forward biased Si LED, band-edge recombination leads to a narrow EL-spectrum in the near IR range ($\sim 1100$ nm). A natural curiosity arises: is the EL-spectrum electrically tunable without modifying the material properties ? The answer is yes.

It has been demonstrated earlier [25–30] that during avalanche breakdown in Si, and in other semiconductors like germanium, hot electrons with a wide spread in momentum are generated after being accelerated by the high electric field. The momentum-spread is such that a band-to-band transition with a transition energy pronouncedly higher than the band gap is possible. The energy of photons involved in such an emission process encompasses a broad spectral range: from ultraviolet (UV), till the near IR

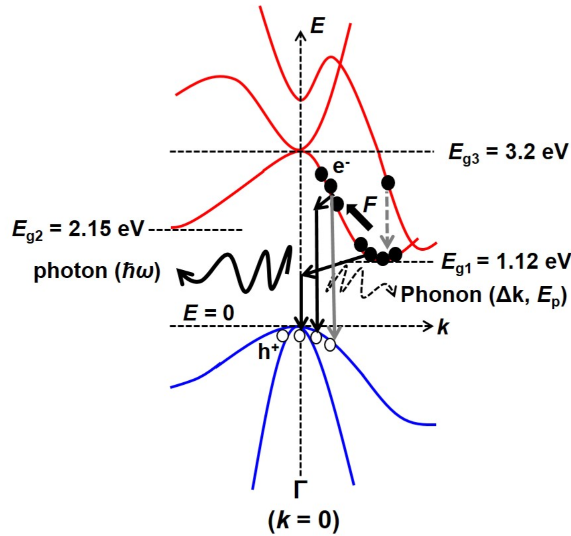


Figure 2.4: Electronic band structure (E-k diagram) of bulk crystalline silicon at $T = 300$ K [24] to illustrate phonon-assisted electron-hole recombination (solid black arrows). Direct recombination and intra-band transition is shown by the solid grey and the dashed grey arrow respectively. The indirect band gap of 1.12 eV is calculated w.r.t. the valence band maximum ($E = 0$, $k = 0$).

range. Thus, the high reverse electric field assists the carriers to occupy higher energy levels prior to a recombination event. However, since the net generation rate at breakdown is high, the relative number of recombination events is low. Consequently, the EL quantum efficiency is low, even less than that for forward-biased band-edge IR emission.

Various mechanisms have been proposed to explain the physical origin of breakdown emission. For Si p-n junctions, it was postulated [28, 29] that indirect inter-band transition is the dominant mechanism producing photons with energies between 1.4 eV and 2 eV, and direct recombination between high energy electrons and holes dominates above 2.3 eV. In another recent work [30], a mix of indirect inter-band, direct inter-band, and low energy intra-band transitions were proposed. In this chapter, indirect inter-band recombination of carriers has been considered as the dominant mechanism to model photon generation [13, 27, 31], because the transition energy involved leads to a peak in the EL-spectrum near 620 nm as observed in our experiments and discussed in section 3.3. Hot carrier intra-band relaxation in Si would lead to a tail of longer wavelength emission [29], which is relatively insignificant in our devices. The fact that carriers are accelerated to high energies, also significantly lowers the probability of the conventional band-edge transition. For initiation of avalanche, it has been debated and derived that conservation principles predict a minimum threshold to be 1.5 times the band gap [16, 33, 34]. Furthermore, it

was also reported earlier [30, 32] that interstitials and dopant impurities that accumulate at structural defect sites, act as capturing and scattering centers for carriers, and assist in indirect recombination processes. These micro-defects (also popularly known as microplasma) act as powerful light emission centers in the Si lattice.

Let us end this section by visualizing the light emission process in Si by an analogy of a big party, with men and women representing electrons and holes respectively or vice versa. We can think of radiative recombination as being the event that a person approaches and talks to his/her crush to eventually result in consummation or a relationship. If he/she can approach his/her mate directly (direct recombination), then there is a higher chance of success (light emission), but this requires the right amount of courage (momentum). Unfortunately he/she is shy enough not to do that so easily. Good friends come to help (phonons) to encourage them or act as a third wheel to pass on his/her message to his/her mate (indirect recombination). This process has its own risk, that the probability of success is low. To stimulate the scenario, we can bring energetic food or beer to everyone (electric field). This increases self-confidence rapidly (avalanche) leading to a higher chance of success among a broad range of people (broad spectrum). However, this comes at the cost of gastronomic resources (electrical power).

## 2.4 Opto-electronic model

In deriving a model that links the optical and electrical behavior of an abrupt, 1-D $p^+n$ junction in avalanche breakdown, we begin by defining the probability distribution of hot carriers as a function of electron temperature $T_e$ which is calculated from the field distribution. Subsequently, the optical emission rate [27] is related to the electric field profile and thereby, to the bias voltage. In the upcoming paragraphs, the individual parameters and functions are addressed that contribute to determining the rate of emission as a function of free space optical wavelength. These are then combined to evaluate the photon emission flux.
As mentioned in section 2.2, we can extract the maximum field at the junction by rearranging Eq. (2.5) and express it in terms of the reverse bias voltage V as:

$$F_{max} = \left(\frac{2qNV}{\epsilon_{Si}}\right)^{\frac{1}{2}}, \tag{2.7}$$

where we have used:

$$W_{dep} = \frac{2V}{F_{max}}. \tag{2.8}$$

### 2.4.1 Electron temperature

To connect the electrical bias with the light emission spectra, we include an energy balance relation for non-equilibrium hydrodynamic transport in silicon [35]. This can be used to establish the relation between $T_e$ and $F(x)$ :

$$\frac{dT_e}{dx} + \frac{T_e(x) - T_0}{\lambda_e} - \frac{2qF(x)}{5k_B} = 0, \tag{2.9}$$

where $T_0$ is the lattice temperature, $k_B$ is the Boltzmann constant, $x$ is the position and $\lambda_e$ is the mean energy relaxation distance for electrons, which is expanded [35] as

$$\lambda_e = \frac{5\nu_{sat}}{3\nu_l}, \tag{2.10}$$

where $\nu_l$ is the collision frequency with lattice atoms (via intra-valley acoustic phonon scattering) [36] and $\nu_{sat}$ is the high field saturation velocity of electrons. From impact ionization studies in thin silicon diodes [37], $\lambda_e$ = 65 nm was reported.
The general solution for Eq. (2.9) is [35]

$$T_e(x) = T_0 + \frac{2q}{5k_B}\int_0^x F(u)\exp\left[\frac{u-x}{\lambda_e}\right]du, \tag{2.11}$$

which can be written as:

$$T_e(x) = T_0 + \Delta T_e(x). \tag{2.12}$$

Evaluating Eq. (2.11) for $F(u)$ as the linear field profile (Eq. (2.3)), we get:

$$\Delta T_e(x) = \frac{2qF_{max}\lambda_e}{5k_B}\left[1 - \frac{(x-\lambda_e)}{W_{dep}} - \left(1 + \frac{\lambda_e}{W_{dep}}\right)\exp\left(\frac{-x}{\lambda_e}\right)\right]. \tag{2.13}$$

The graphical description of Eq. (2.13) is shown in Fig. 2.5. The peak of $T_e(x)$ does not coincide with the position of the peak electric field $F_{max}$ as determined from the classical local avalanche model as in Eq. (2.7). Within $\lambda_e$, the electron temperature is less than the maximum value. The effect of the peak field on the electron temperature is thus space-shifted. This implies that if the depletion width of a junction is too thin, the electrons will not gain sufficient energy needed for avalanche multiplication. Consequently avalanche and hence photon emission will be suppressed for small breakdown voltages.

Note that the total carrier energy is given by $E_g + 1.5k_bT_e$. The analytically computed electron temperature is expected to be slightly higher than in reality. This is because in Eq. (2.9), we ignored any energy term accompanying phonon-emission/absorption during the drift of carriers under a high electric field [38]. For a more accurate analysis, numerical Monte-Carlo based hydrodynamic simulations can be pursued to involve

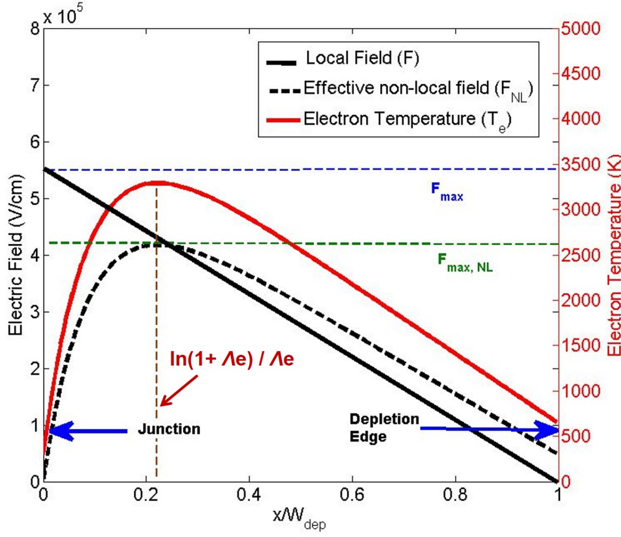


Figure 2.5: Example of the spatial distribution of electrostatic field F (*local and non-local*), and electron temperature $T_e(x)$ (Eqs. (2.12), and (2.13)), along the depletion region at $T_0 = 300$ K and a doping level of $N = 10^{17}$ cm$^{-3}$, $V_{BR} = 14$ V, and $W_{dep} \approx 0.7$ µm.

true carrier distribution functions.

In order to capture the dependence of electron temperature on varying $V_{BR}$ and thereby varying $F_{max}$, either the peak or the spatial average of $T_e(x)$ can be computed to simplify the analysis. The peak $T_e$ can be used to obtain the peak optical intensity, which happens at a specific location in the EL-region. However, in order to compare the total integrated optical power, one needs to take into account the spatial profile of $T_e$. In such a case, defining the average $T_e$ is helpful. This is useful to compare devices with different field profiles, for example a $p^+$-n and a p-i-n diode (as will be discussed in the next chapter). The spatial average of $T_e$ (denoted by $T_e|_{avg}$) is given by:

$$T_e|_{avg} = \frac{1}{W_{dep}} \int_0^{W_{dep}} T_e(x)\,dx, \tag{2.14}$$

which gives us:

$$\Delta T_e|_{avg} = \frac{2qF_{max}\lambda_e}{5\Lambda k_B}\left[\frac{\Lambda}{2} - \frac{1}{\Lambda} + \left(1 + \frac{1}{\Lambda}\right) \cdot \exp\left(-\Lambda\right)\right], \tag{2.15}$$

where

$$\Lambda = \frac{W_{dep}}{\lambda_e}. \tag{2.16}$$

Similarly, one can also obtain the peak $T_e$ by differentiating Eq. (2.13) w.r.t. $x$. This maximum occurs at $x = \lambda_e \cdot \ln(1+\Lambda)$, and we get:

$$\Delta T_e|_{max} = \frac{2qF_{max}\lambda_e}{5k_B}\left[1 - \frac{1}{\Lambda}\left(\ln(1+\Lambda) - 1\right) - \left(2 + \Lambda + \frac{1}{\Lambda}\right)\right]. \quad (2.17)$$

The classical local avalanche model fails to depict this effect, because it considers $dT_e/dx = 0$ in Eq. (2.9). The non-local breakdown voltage ($V_{BR,NL}$) is calculated by first extracting the effective field distribution [37] from Eq. (2.13) and then substituting it in Eq. (2.1) to get the new critical maximum field as:

$$F_{NL}(x) = \frac{5}{2}\frac{k_B \Delta T_e(x)}{q\lambda_e}, \quad (2.18)$$

$$\int_0^{W_{dep}} \alpha_0 F^7_{crit,NL}(x)dx = 1. \quad (2.19)$$

And then evaluating the area bounded by $F_{crit,NL}(x)$:

$$V_{BR,NL} = \int_0^{W_{dep,NL}} F_{crit,NL}(x)dx, \quad (2.20)$$

where $W_{dep,NL}$ is calculated using Eq. (2.5).

Fig. 2.6 shows the variation of the average $T_e$ obtained using Eq. (2.15) with calculated breakdown voltage using Eq. (2.20) for different doping levels. The nonlocal avalanche effect [20, 37] can be noticed, showing that when $V_{BR}$ is lower than a certain value, around 5 V, $T_e|_{avg}$ rises with increasing $V_{BR}$. Beyond 5 V, $T_e|_{avg}$ decreases with increasing $V_{BR}$. A similar curve can be obtained if one calculates the peak $T_e$, in order to analyze the maximum optical intensity within the active EL-region of the device. The dashed curve is the solution obtained from the local avalanche model where the spatial derivative of $T_e$ is zero. From this point onwards, unless explicitly specified, we shall refer to the average electron temperature by simply $T_e$.

### 2.4.2 Carrier distribution function

Since the total energy of the carrier in avalanche breakdown is larger than the thermal energy, $E >> k_B T_e$, a quasi-Maxwellian distribution for holes against energy is assumed as in [27]

$$f_h(E) \approx \exp\left[-\frac{E}{k_B T_e}\right], \quad (2.21)$$

For hot electrons, the Boltzmann equation can be solved approximately, considering the avalanche emission as a plasma discharge phenomenon

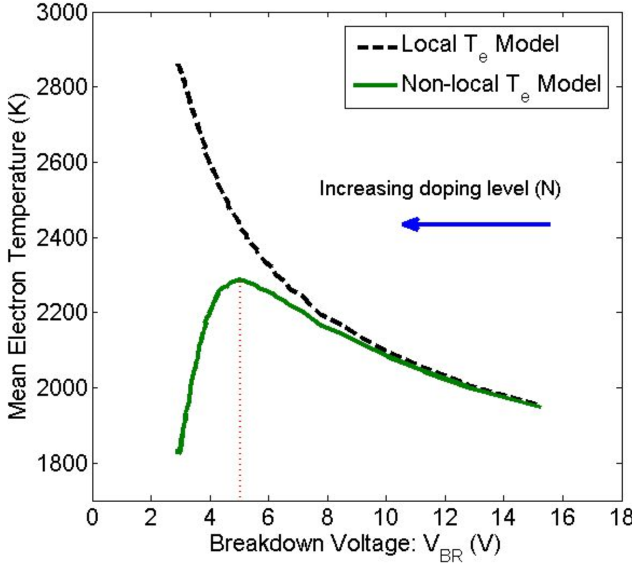


Figure 2.6: The space-averaged electron temperature (in *green*) (Eqs. (2.14), and (2.15)), versus breakdown voltage calculated from Eq. (2.20) at $T_0 = 300$ K. The dashed curve (in *black*) is the solution obtained from the local avalanche model where the spatial derivative of $T_e$ is zero.

[39]. Following Wolff's description [39], and ensuring continuity in electron distribution function over all energies, we have, for electron energies higher than the ionization threshold energy,

$$f_e(E) = \frac{1}{2} \exp\left(\frac{-E}{k_B T_e}\right) \cdot \left[1 + \frac{Ei\left(\frac{E}{k_B T_e}\right)}{Ei\left(\frac{E_{ion}}{k_B T_e}\right)}\right], \tag{2.22}$$

where $E_{ion} \approx 2.3$ eV is the average threshold energy for electrons needed for ionization. $Ei(X)$ represents the exponential integral, which can be approximated [40] when the variable $X > 2$ (valid in our case), as

$$Ei(X) = \int_{-\infty}^{X} \frac{\exp(u)}{u} du \approx \exp(-X) \cdot \ln\left(1 + \frac{1}{X}\right). \tag{2.23}$$

For energies lower than $E_{ion}$, we assume a quasi-Maxwellian distribution for electrons as well, similar to Eq. (2.21) for holes.

It is worth clarifying that the assumption of a quasi-Maxwellian carrier distribution, and in particular Wolff's description, assumes a parabolic band structure, hence assuming isotropic effective masses in both conduction and valence band. Further, it assumes that carriers have thermalized, and thus both momentum and energy relaxation of the carriers have occurred [41], which in turn precedes photon emission. This is a reasonable

approximation only if one considers ionization events below and upto the average (in energy domain) hot electron energy [41]. When applied to this work, this translates to an energy range of $E_g + 1.5k_bT_e = \sim 1.6$ eV. For higher electron energies, however, deviations are expected due to non-parabolic nature of the bands. This would require more intricate analysis for e.g. 1-D Monte-Carlo simulation [42], where it was shown that for $T_e > 5000$ K, $f_e$ falls relatively more rapidly for energies higher than $\sim 1.5$ eV, as compared to that obtained from the quasi-Maxwellian approximation. On the other hand, for circuit simulations, a relatively simple physics-based numerical or closed-form model is needed.

### 2.4.3 Bimolecular recombination coefficient

In order to find out the probability of carrier recombination, the bimolecular recombination coefficient, $B$, must be taken into account. It was found experimentally [26] that emission from breakdown initiates in the form of localized spots in the active region near the junction edge. The recombination spots have been modeled as micro-plasma channels with hot carriers. The value of $B$ can thus be expected to be higher than the bulk standard value [3] since direct energy transitions are possible.
In prior literature, from a theoretical perspective, $B$ has been evaluated as the product of capture cross-section area of the recombination spot and the velocity of free/hot electrons [43].

Hence, for analytical simplicity, we assume that at high fields, the electrons are traversing with saturation velocity $v_{sat}$. The opto-electronic model in this work does not delve any deeper into the quantitative accuracy of $B$, since our experiment does not yield the absolute optical power. Nonetheless, it has been assumed that $B$ is independent of $E$, and $T_e$. The determination of the actual $B$ during avalanche breakdown are open to future research.

### 2.4.4 Photon spectral emission flux

Once the carrier distribution functions are calculated, one can proceed to evaluate the rate of photon emission. The functions $f_e$ and $f_h$ are dependent on $T_e(x)$. So, strictly speaking, different positions along the space-charge region should contribute unequally to photon emission. However, since avalanche breakdown and light emission are only dominant close to the junction, the model can be simplified by using $T_e|_{avg}$ (a function of $V$ and $N$) in defining the effective carrier distribution functions and as a result, the rate of photon emission.

Since the phonon energies are negligible compared to photon energies involved ($\hbar\omega$) in avalanching Si junctions, and photon emission below the indirect band gap $E_{g1}$ is ignored, we can write the emission spectral flux

of photons ($\varepsilon(\omega)$) ($cm^{-2}s^{-1}$), following the work of Lahbabi *et al.* [27] , as:

$$\varepsilon(\omega) = B{\cdot}C{\cdot}W_{dep} \int_{E_{g1}}^{\hbar\omega} \hbar\omega \left[E(\hbar\omega - E_{g1} - E)\right]^{\frac{1}{2}} f_e(E) f_h(\hbar\omega - E_{g1} - E) dE, \tag{2.24}$$

where

$$C = \frac{2(m_e^* m_h^*)^{\frac{3}{2}}}{\pi^4 \hbar^6}, \tag{2.25}$$

where $m_e^*$ and $m_h^*$ are the density-of-states effective masses of the conduction and valence bands, respectively.

The computed emission spectra are compared with experimental data in Fig. 2.10, and Fig. 2.11. Although the spectrum is related to the electron temperature, the photon-emission mechanism is electron-hole recombination. The underlying physics is distinct from thermal continuum emission mechanisms like blackbody radiation, and bremsstrahlung. Firstly, blackbody radiation emanates from oscillating charged particles (e.g. lattice ions and electrons) all in thermodynamic equilibrium, where transitions at every wavelength are allowed. This situation ceases to be valid when electrons are accelerated by a high electric field in a crystalline solid with a well-defined band structure. Secondly, the bremsstrahlung mechanism has been previously shown not to be the origin of avalanche-mode light emission in the context of Si and Germanium p-n junctions [31]. In particular, this mechanism dominates only when $k_B T_e > \hbar\omega$, [44, 45] i.e. the electron energy exceeds the binding energy of the interacting ion in the lattice (equivalently the photonic transition energy). This condition is also not applicable in our case.

### 2.4.5 Photon extraction and optical power

After obtaining Eq. (2.24) between the emission spectrum and V (hence, F), one can obtain the optical intensity $I_{op}$ by integrating the EL-spectrum over all wavelengths. In addition, wavelength-dependent self-absorption in Si, and Fresnel reflections at the Si surface (that interfaces dielectrics like $SiO_2$ or just air) are also incorporated to obtain the following relation:

$$I_{op} = \int_{\hbar\omega} \varepsilon(\omega) \cdot (1 - R(\omega)) \cdot \exp\left(-\alpha_{abs}(\omega) \cdot x_j\right) d(\hbar\omega), \tag{2.26}$$

where $\alpha_{abs}(\omega)$ is the Si-absorption coefficient, $x_j$ is the junction depth and $R(\omega)$ is the reflection coefficient at the interface between Si and back-end layers (like $SiO_2$). In case there is no back-end stack, $R(\omega)$ at the Si-air interface is given by :

$$R(\omega) = \left[\frac{n_{Si}(\omega) - 1}{n_{Si}(\omega) + 1}\right]^2. \tag{2.27}$$

In the model proposed for the absorption coefficient [46], absorption below the band gap has been ignored. Only Transverse (TA) and Transverse Optical (TO) mode phonons have been considered. The experimentally fitted model [46] for the absorption coefficient $\alpha_{abs}(\omega)$ is the piecewise sum of direct transition (Eq. (2.29)) and indirect transition components (Eq. (2.30)) according to

$$\alpha_{abs}(\omega) = \alpha_d(T,\omega) + \alpha_i(T,\omega), \quad (2.28)$$

$$\alpha_d(T,\omega) = A_d \cdot [\hbar\omega - E_{g3}(T)]^{\frac{1}{2}}, \quad (2.29)$$

$$\alpha_i(T,\omega) = \sum_{(i,j=1,2)} C_i \cdot A_j \cdot \left[ \frac{(\hbar\omega - E_{gj}(T) + E_{pi})^2}{\exp(\frac{qE_{pi}}{k_B T}) - 1} + \frac{(\hbar\omega - E_{gj}(T) - E_{pi})^2}{1 - \exp(\frac{-qE_{pi}}{k_B T})} \right] \quad (2.30)$$

where $T = T_0$ is the lattice temperature, $C_i$ is the coupling coefficient and $A_j$ is a normalization factor whose values have been determined [46] by fitting experimental data. $E_{pi}$ denotes the quantum of phonon energy in the $i^{th}$ mode and $\hbar\omega$ is the energy of the photon being absorbed. $E_{g1}$, and $E_{g2}$, represent the two lower indirect band gaps and $E_{g3}$ represents the direct band gap [46].

The optical power (P) can be estimated from the product of intensity, the active EL area of the diode A, and the Lambertian factor to account for Total Internal Reflection (TIR) [3]:

$$P \approx I_{op} \cdot A \cdot \frac{1}{2}\left[1 - \cos\left(\sin^{-1}\left(\frac{1}{n_{Si}}\right)\right)\right]. \quad (2.31)$$

A list of all the fitting and physical model parameters used in the opto-electronic model discussed so far is provided in Appendix A.

## 2.5 Model validation from experiments

Experimental data depicting EL-spectra of p-n junctions in avalanche breakdown, have been presented already in prior literature [27, 47–49]. However, not enough parameters (structural and process-related) of those devices are available to investigate the validity of the present model. Hence, we describe devices with known geometry and process parameters, for model validation.
For an experimental validation of the model, it is desirable to measure light emission from diodes with a uniform breakdown field over the whole

active area and with a low attenuation of the generated photons. This can be achieved when the avalanching point is close to the Si surface and the surface is not covered by absorbing or reflecting layers. These conditions are almost ideally met by using the vertical $p^+n$ diodes reported in [18, 51]. A schematic cross-section of this diode structure is shown in Fig. 3.3. The anode is formed by a pure boron deposition, ~ 3 nm thick, from which a p-doped Si surface region of only about 12 nm deep is formed. This creates an abrupt $p^+$-n junction. A high electric field is thus formed at a depth of ~ 12 nm. For an LED, the non-depleted p-doped layer can have high optical absorption, particularly for wavelengths below 400 nm where the attenuation length goes below 10 nm in Si.

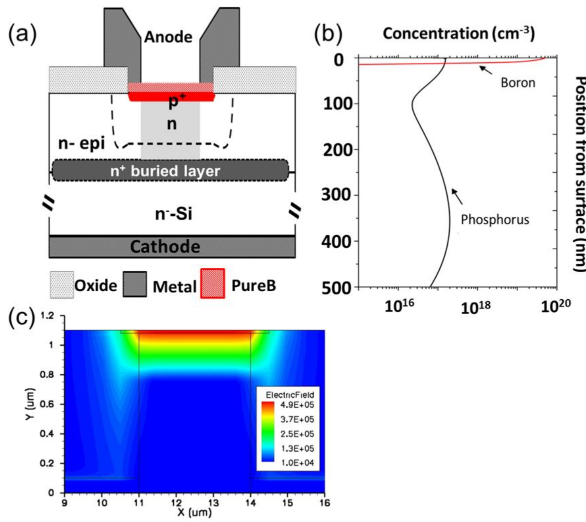


Figure 2.7: (a) Schematic cross-section of the $p^+n$ junction, where the n-enrichment region is shown in light grey below the $p^+$ layer, (b) vertical doping profile obtained from TCAD process simulation, and (c) the field distribution obtained from TCAD device simulation [18].

The central diode area has an n-enrichment implantation as shown in Fig. 3.3. Due to the very light doping around the diode perimeter, the peripheral breakdown voltage is higher. This also means that the electric field and consequently the contribution of interface traps at the depleted Si-$SiO_2$ interface bordering the anode is significantly reduced, which may otherwise cause premature breakdown. A TCAD simulation of a typical electric field distribution in the device is also shown in Fig. 3.3, which depicts that the peripheral field is lower than the central region (enrichment layer). Moreover, at the periphery of the diodes is contacted by a 1-µm-wide ring of the Al interconnect, 675 nm thick, which will strongly reflect and absorb light so that no light emission is expected to be seen in this region. Devices were fabricated with and without an $n^+$-buried layer that increases the effective doping level in the enrichment region, and consequently reduces the $V_{BR}$ from 14 V to 7 V. The diodes have a

circular geometry, and unless explicitly specified, the spectral and optical measurement data (T = 300 K) refer to a device with 40 μm diameter and an anode contact ring, 1 μm wide, along the perimeter.



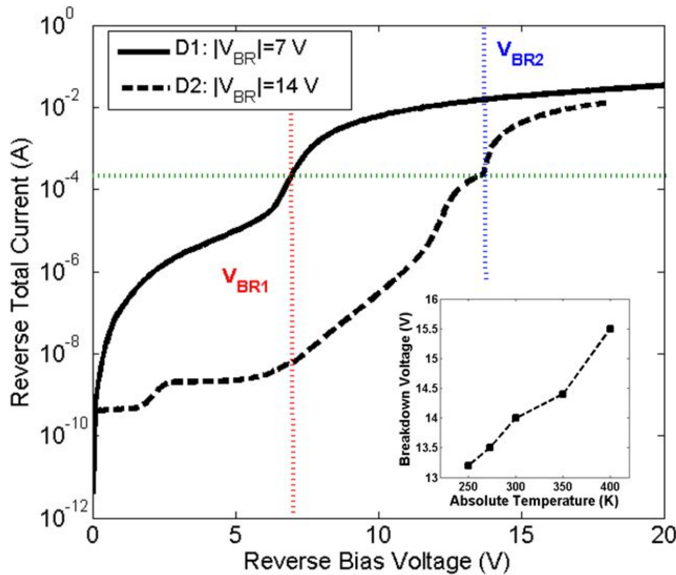


Figure 2.8: Measured *I-V* characteristics of the diodes at T = $T_0$ = 300 K with $V_{BR}$ = 7 and 14 V, each with diameter 40 μm. Breakdown is defined at a current level of 0.5 mA (*green*); *(inset)* Temperature dependence of measured $V_{BR}$ showing a positive temperature coefficient (PTC).

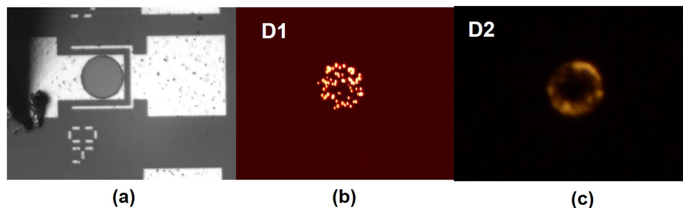


Figure 2.9: (a) Magnified top view of the diode under test (D2) in this work. The active area is a circle of 40 μm diameter. Bright field optical micrographs of (b) D1 and (c) D2 at a current I = 20 mA showing visible light emission in avalanche breakdown observed through cooled XENICS (XEVA-257) camera and integrated over 20 s duration.

Fig. 2.8 shows the current-voltage (I − V) characteristics of two diodes, one (D2) with twice the value of $V_{BR}$ (defined at I = 0.5 mA) than the other (D1). The avalanche mechanism in breakdown can be verified from the inset in Fig. 2.8 which shows a Positive Temperature Coefficient (PTC) in measured $V_{BR}$ for D2. The device D1 has a significantly higher leakage current due to defects introduced by the processing of the buried layer combined with the higher magnitude of electric field, likely leading to

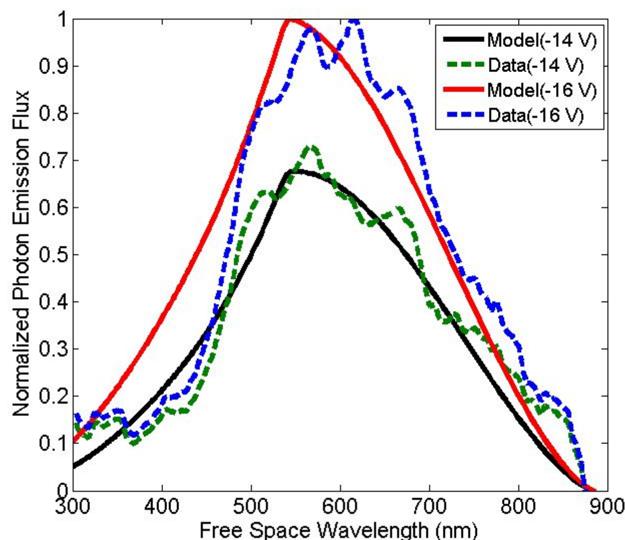


Figure 2.10: Comparison between measured (*dashed*) and modeled (*bold*) spectral variation in photon emission flux at two bias points $V > V_{BR} = 7$ V for diode D1.

trap-assisted band-to-band tunneling [19]. For $V > V_{BR}$, the current gets limited by series resistance. It has been demonstrated earlier [52] that the tunneling component of the total reverse current does not contribute to the optical power output, because the tunnel current carriers do not undergo inter-band energy transitions [53].

Fig. 2.9(a) shows the magnified gray-scale top-view of the diodes, with the bright-field optical micrographs of D1 and D2 in Fig. 2.9(b) and (c) respectively. In D1, microscopic visible light emission spots spread over the circular active area are observed. It is evident that breakdown is within the n-enrichment region and not confined along the edge/perimeter. To the naked eye, the spots appear greenish-white, although the apparent color and brightness depends on the depth of the spots. Similar emission patterns have also been observed in prior literature [48, 49] where it has been claimed that localized defects at the metallurgical junction act as the onset-points (microplasma) for light emission. Furthermore, the location of the spots are the same when the experiment is repeated. It has been observed that with higher voltage levels, more spots become visible [26, 33]. In D1, these defect-based microplasmas are likely the result of the $n^+$ buried layer, which is not present in D2. This difference is evident from Fig. 2.9(c), where light emission is observed in the form of a relatively diffused glow dominating over the peripheral region, and decaying towards the center of the active area. This decay is likely due to current crowding, resulting from the lateral series resistance.

The EL spectra of the diodes are characterized using an ADC-1000-USB spectrometer from Avantes, with a 50 μm multi-mode optical fibre. The spectral line width (resolution) is 0.4 nm. The integration time is chosen as 16 s, which sufficed to get good measurement data. The obtained spectra show the presence of ripples; the origin of which, is not fully understood. In our device (Fig. 3.3), light emerging from Si traverses an optically thin Boron film (~ 3 nm), and then being received by the optical fiber, mounted at an angle. Fabry-Perot resonance can likely cause the ripples, but it is not expected to be significant in our device, since the junction depth is much smaller than the optical wavelengths involved. It is assumed that the ripples are possibly due to interference from the emission spots, or noise in the uncooled electronics in the detector. The latter was observed to reduce with averaging of multiple frames of EL-spectral data.

A comparison between the modeled (integrand of Eq. (2.26)) and measured trends in spectral emission flux and integrated intensity (Eq. (2.26)) for both the diodes is shown in Figs. 2.10-2.14. An absolute quantitative comparison of the light intensity between the model and experimental emission spectrum is difficult due to the laterally non-uniform emission (Fig. 2.9). However, relative intensity comparisons and spectral information can be used to compare the model with experiments of the two diodes D1 and D2 at different bias voltages. An additional empirical pre-factor $\Theta$ has been used to fit the measured data. Thus, $I_{op}$ becomes $\Theta \cdot I_{op}$. The physical justification for $\Theta$ is as follows.

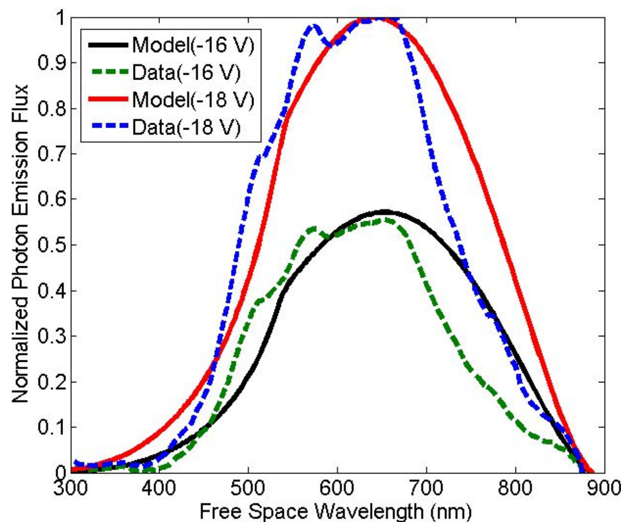


Figure 2.11: Comparison between measured (*dashed*) and modeled (*bold*) spectral variation in photon emission flux at two bias points $V > V_{BR} = 14$ V for diode D2.

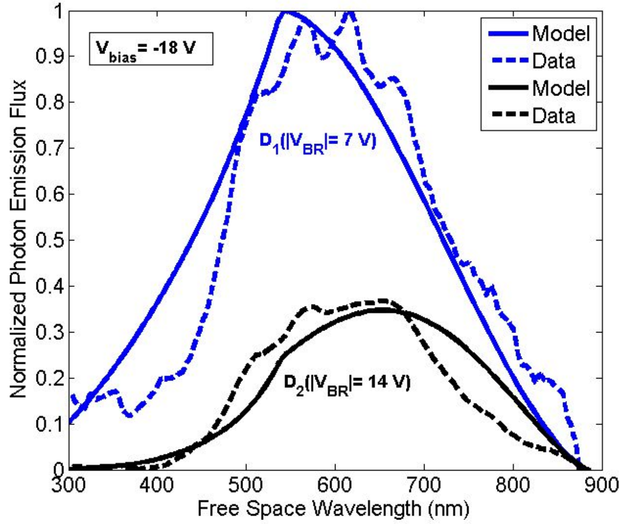


Figure 2.12: Relative Comparison between measured (*dashed*) and modeled (*bold*) spectral variation in photon emission flux at a reverse bias of 18 V for both diodes.

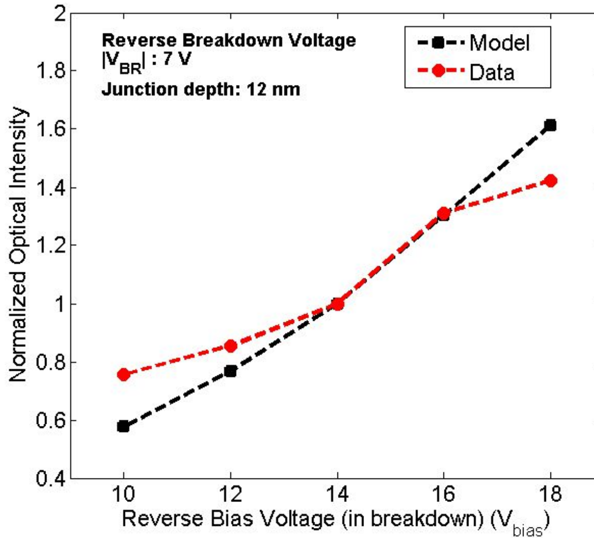


Figure 2.13: Comparison between measured and modeled intensity variation for D1 ($V_{BR} = 7$ V).

With increasing bias voltage V, the steady-state avalanche current increases. However, the efficiency of radiative recombination is injection dependent, which has not been incorporated in the parameter B. High injection levels stimulate an enhanced fraction of Auger recombination [54]. Moreover, since the diodes are biased deep in avalanche, current becomes

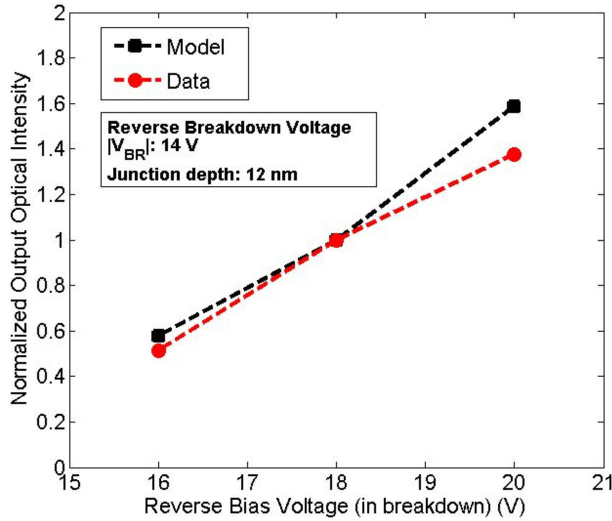


Figure 2.14: Comparison between measured and predicted intensity variation for D2 ($V_{BR} = 14$ V).

space-charge limited [18], and eventually the series resistance kicks in. The internal reverse bias (and maximum field) across (at) the junction, therefore does not increase much beyond $V_{BR}$ ($F_{crit}$).
The effect on the efficiency due to a relative increase in current density (J) (with increasing V for a fixed $V_{BR}$) has been empirically modeled as $J^k$, where k is fitted from experimental results.

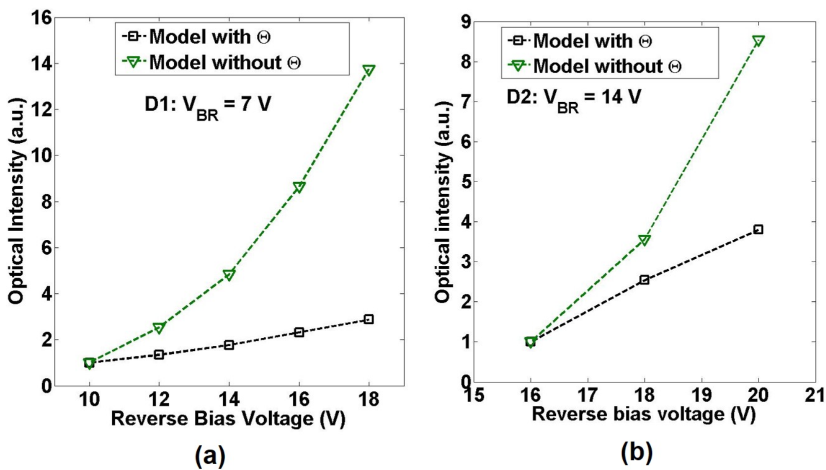


Figure 2.15: Comparison between the modeled intensity variations with bias voltage, including and excluding the parameter Θ for (a) D1 ($V_{BR} = 7$ V), and (b) D2 ($V_{BR} = 14$ V).

In addition, it has been observed from the optical micrographs in Fig. 2.9, that the effective EL-area of D1 and D2 are not the same, and the emission spots are not spread continuously over the active area. Hence, the parameter $A$ in Eq. (2.31) exhibits a variation between the two devices with a different $V_{BR}$, caused by process modification (incorporation of the buried layer). In order to compare the optical outputs of the diodes with different $V_{BR}$, an additional factor is included. Combined, the dimensionless empirical pre-factor $\Theta$ is written as:

$$\Theta = \left( \frac{J(V)}{J(V = V_{BR})} \right)^{k} \cdot \left( \frac{V_{BR}}{V_{ref}} \right)^{m}, \tag{2.32}$$

where $V_{ref}$ = 6.72 V, is a fit parameter. The values of $k$ and $m$ have been estimated from measured relative intensity levels in our experiments (see Appendix A). The fitted value of $k$ = -1 strongly indicates the effect of dynamic resistance in the avalanche regime of J-V characteristics, as reported earlier [55] for diffused junctions. A similar value of -1.02 as the exponent was obtained in [52] while modeling the dependence of the dynamic avalanche diode resistance with current, by analyzing AM-EL measurements. The modeled variations in the optical intensity w.r.t. $V$ for both D1 and D2, with and without including the fitted pre-factor $\Theta$ are compared in Fig. 2.15.

It is observed from Figs. 2.10 and 2.11 that the model is in agreement with the experiments, except for two minor discrepancies: firstly, the ripples as mentioned previously and secondly, the measured spectra falls sharper than predicted using Eq. (2.24) in the low-$\lambda$ regime ($\leqslant$ 550 nm). The latter could be attributed to two reasons. Firstly, from an experimental viewpoint, there is increased scattering at shorter wavelengths, and absorption in the PureB layer, thus photons not reaching the optical fiber. Secondly, for higher photon energies, the quasi-Maxwellian carrier distribution functions are not accurate as discussed earlier in section 2.4.2. Monte-Carlo simulations are required for a more accurate description of $f_e$ and $f_h$. In Fig. 2.12, the relative emission flux for both diodes are compared for the same reverse bias voltage. Due to a higher maximum field in D1, we observe a higher level of photon emission than in D2. Note that the change in curvature of the modeled spectra beyond the ionization threshold ($\lambda < 550$ nm) is the result of a different hot electron distribution function (Eq. (2.22)).

For a higher reverse bias, the peak field at the junction increases, leading to a higher mean (spatial) electron temperature. Hence, the intensity increases. By fitting the measured trends in total intensity (integrated over the spectral domain), we obtain the parameters $m \approx 6.3$ and $k \approx -1$ defined in Eq. (2.32). From the applied bias voltage, the maximum field is calculated using Eq. (2.7), and then substituted in Eq. (2.13). The com-

parisons for some other bias voltages for both D1 and D2 are shown in Figs. 2.13 and 2.14. Both the diodes have the same geometry and size. We increased V, which inherently increases both F and J. Figs. 2.13 and 2.14 show that the intensity increases with increasing V, hence increasing J.

We have discussed so far in this chapter, how the EL-spectrum of an Si diode depends on the electrical bias. The two diodes dealt herein were made in a custom process, suited for optical functionality. However, it was difficult to study the experimental dependence of optical power on $V_{BR}$ alone, because $V_{BR}$ was changed via additional processing. This also affected other material parameters e.g. defects, which altered the effective EL-area of the LEDs significantly. A natural curiosity arises: how does the optical power and its efficiency vary by changing only $V_{BR}$ ? After all, Fig. 2.6 predicts that for a purely triangular field profile, where $V_{BR}$ is tuned by changing N, the electron temperature shows a maximum only around $V_{BR} \approx 5$ V. Does this non-local avalanche effect also affect the optical power ? Moreover, what would happen if the field profile is not triangular, but rectangular as in p-i-n like diodes or trapezoidal as in fully depleted short diodes ? We shall attempt to answer these questions in the next chapter from a theoretical as well as experimental perspective.

## 2.6 Conclusions

In this chapter, a general one-dimensional physics-based model has been demonstrated to establish a relationship of light emission from avalanche breakdown in Si $p^+n$ junctions with the applied reverse bias voltage. The model predicts the primary dependence of emission spectrum on the hot carrier temperature which can be derived from the effective electric field. The effect of bias on the relative increase in emission intensity has been modeled for devices with two different breakdown voltages, which was then validated using experimental trends. The model describes the EL-spectrum arising from indirect inter-band transitions. However, there is some uncertainty in determining the optically active area (due to emission spots), and the radiative recombination coefficient. The optical intensity for a fixed device (and hence fixed $V_{BR}$) is an increasing function of the magnitude of reverse bias voltage. Lowering the breakdown voltage leads to a higher relative optical intensity and current densities at the same reverse bias voltage. The model predicts the existence of a lower limit to breakdown voltage ($\sim 5$ V) for an ideal triangular field profile, below which non-local avalanche effects dominate, and carriers will not gain the high energies required for photon emission. The model serves as a guideline for co-optimization of electrical and optical parameters and as a future scope, can be extended to other semiconductors as well.

# BIBLIOGRAPHY


[1] S. Dutta, R.J.E. Hueting, A.J. Annema, L. Qi, L.K. Nanver and J. Schmitz, "Opto-electronic modeling of light emission from avalanche-mode silicon $p^{+}n$ junctions," J. Appl. Phys., vol. 118, 114506, 2015.

[2] M.A. Green, "Self-consistent optical parameters of intrinsic silicon at 300 K including temperature coefficients," Solar Energy Materials & Solar Cells, vol. 92, pp. 1305-1310, 2008.

[3] E.F. Schubert, "Light Emitting Diodes," Cambridge University Press, 2006.

[4] M. Green, J. Zhao, A.Wang, P. Reece, and M. Gal, "Efficient silicon light emitting diodes," Nature, vol. 412, no. 6849, pp. 805-808, 2001.

[5] T. Trupke, J. Zhao, A.Wang, R. Corkish, and M. A. Green, "Very efficient light emission from bulk crystalline silicon," Appl. Phys. Lett., vol. 82, no. 18, pp. 2996-2998, 2003.

[6] B.P. van Drieënhuizen and R.F.Wolffenbuttel, "Optocoupler based on the avalanche light emission in silicon," Sensors and Actuators A, vol. 31, pp. 229-240, 1992.

[7] S. Mandai, M. W. Fishburn, Y. Maruyama and E. Charbon, "A wide spectral range single-photon avalanche diode fabricated in an advanced 180 nm CMOS technology," Optics Express, vol. 20, no. 6, pp. 5849-5857, 2012.

[8] L. Shi, S. Nihtianov, L. Haspeslagh, F. Scholze, A. Gottwald and L.K. Nanver, "Surface-charge-collection-enhanced high-sensitivity high-stability silicon photodiodes for DUV and VUV spectral ranges," IEEE Trans. Electron Devices, vol. 59, no. 11, pp. 2888-2894, 2012.

[9] L. Rebohle, J. Von Borany, D. Borchert, H. Fröb, T. Gebel, M. Helm, W. Möller, W. Skorupaa, "Efficient blue light emission from silicon," Electrochemical and Solid-State Lett., vol. 4, no. 7, pp. G57-G60, 2001.

[10] M. du Plessis, H. Aharoni, and L.W. Snyman, "Silicon LEDs fabricated in standard VLSI technology as components for all silicon monolithic integrated optoelectronic systems," IEEE J. Selected Top. Quantum Electron., vol. 8, no. 6, pp. 1412-1419, 2002.

[11] A. Chatterjee, B. Bhuva, and R. Schrimpf, "High-speed light modulation in avalanche breakdown mode for Si diodes," IEEE Electron Device Lett., vol. 25, no. 9, pp. 628-630, 2004.

[12] L.W. Snyman, M. du Plessis, and H. Aharoni, "Injection-avalanche-based $n^{+}pn$ silicon complementary metal-oxide-semiconductor light-emitting device (450 - 750 nm) with 2-order-of-magnitude increase in light emission intensity," Jpn. J. Appl. Phys., vol. 46, no. 4B, pp. 2474-2480, 2007.

[13] L.W. Snyman, M. du Plessis and E. Bellotti, "Photonic transitions (1.4 eV–2.8 eV) in silicon $p^{+}np^{+}$ injection-avalanche CMOS LEDs as function of depletion layer profiling and defect engineering," IEEE J. Quantum Electron., vol. 46, no. 6, pp. 906-919, 2010.

[14] L.W. Snyman, J-L. Polleux, K. A. Ogudo, C. Viana, and S. Wahl, "High intensity 100 nW 5 GHz silicon avalanche LED utilizing carrier energy and momentum engineering," *proc. SPIE*, vol. 8990, 89900L, *Silicon Photonics IX*, Mar. 2014, doi:10.1117/12.2038195.

[15] S. Dutta, G.J.M. Wienk, R.J.E. Hueting, J. Schmitz, and A.J. Annema, "Optical power efficiency versus breakdown voltage of avalanche-mode silicon LEDs in CMOS," IEEE Electron Device Lett., vol. 38, no. 7, pp. 898-901, 2017.

[16] S.M. Sze and K.K. Ng, "Physics of Semiconductor Devices," 3$^{rd}$ edition, John Wiley & Sons, Inc., USA, 2007.

[17] B.J. Baliga, "Fundamentals of Power Semiconductor Devices," Springer, 2008.

[18] A. Rose, "Space-charge-limited current in solids," Phys. Rev., vol. 97, no. 6, pp. 1538-1544, 1955.

[19] G.A.M. Hurkx, D.B.M. Klaassen, and M.P.G. Knuvers, "A new recombination model for device simulation including tunneling," IEEE Trans. Electron Devices, vol. 39, no. 2, pp. 331-338, 1992.

[20] G.J. Rees and J.P.R. David, "Nonlocal impact ionization and avalanche multiplication," J. Phys. D: Appl. Phys., vol. 43, p. 243001, 2010.

[21] W. Fulop, "Calculation of avalanche breakdown of diffused silicon p-n junctions," Solid-State Electronics, vol. 10, pp. 39-43, 1967.

[22] Robert F. Pierret, "Semiconductor Device Fundamentals," Addison-Wesley Publ., 1996.

[23] K. Kajiyama and H. Kanbe "Temperature dependence of avalanche breakdown voltage in Si p-n junctions," J. Appl. Phys., 47, p. 2744, 1976.

[24] J.R. Chelikowsky, and M.L. Cohen, "Nonlocal pseudopotential calculations for the electronic structure of eleven diamond and zinc-blende semiconductors," Phys. Rev. B, vol. 14, no. 2, pp. 556-582, 1976.

[25] R. Newman, "Visible light from a silicon p-n junction," Phys. Rev., vol. 100, no. 2, pp. 700-703, 1955.

[26] A.G. Chynoweth and K.G. McKay, "Photon emission from avalanche breakdown in silicon," Phys. Rev., vol. 102, no. 2, pp. 369-376, 1956.

[27] M. Lahbabi,A. Ahaitouf,M. Fliyou,E. Abarkan,J.-P. Charles, A. Bath, A. Hoffmann, S.E. Kerns and D.V. Kerns, Jr., "Analysis of electroluminescence spectra of silicon and gallium arsenide p-n junctions in avalanche breakdown," J. Appl. Phys., vol. 95, no.4, pp. 1822-1828, 2004.

[28] J. Shewchun and L.Y. Wei, "Mechanism for reverse-biased breakdown radiation in p-n junctions," Solid-State Electronics, vol. 8, pp. 485-493, 1965.

[29] N. Akil, S. E. Kerns, D. V. Kerns, Jr., A. Hoffmann, and J. P. Charles, "Photon generation by silicon diodes in avalanche breakdown," Appl. Phys. Lett., vol. 73, no. 7, p. 871, 1998.

[30] L.W. Snyman, K. Xu, J-L. Polleux, K. A. Ogudo, and C. Viana, "Higher intensity SiAvLEDs in an RF bipolar process through carrier energy and carrier momentum engineering," IEEE J. Quantum Electron., vol. 51, no. 7, 3200110, 2015.

[31] S. Yamada and M. Kiato, "Recombination radiation as possible mechanism of light emission from reverse-biased p-n junctions under breakdown condition," Jpn. J. Appl. Phys., part 1, vol. 32, p. 4555, 1993.

[32] V. Kveder, M. Badylevich, W. Schröter, M. Seibt, E. Steinman, and A. Izotov, "Silicon light-emitting diodes based on dislocation-related luminescence," Phys. Status Solidi A, vol. 202, no. 5, pp. 901-910, 2005.

[33] J.H. Swoger, S.J. Kovacic, "Enhanced luminescence due to impact ionization in photodiodes," J. Appl. Phys., vol. 74, no. 4, pp. 2565-2571, 1993.

[34] N. Sano and A. Yoshii, "Impact-ionization theory consistent with a realistic band structure of silicon," Phys. Rev. B, vol. 45, no. 8, pp. 4171-4180, 1992.

[35] J.W. Slotboom, G. Streutker,M.J. van Dort, P.H. Woerlee, A. Pruijmboom, and D.J. Gravesteijn, "Non-local impact ionization in silicon devices," International Electron Devices Meeting (IEDM), pp. 127-130, 1991.

[36] W.E. Krag, "Galvanometric effects in n-type silicon," Phys. Rev., vol. 118, no. 2, pp. 435-450, 1960.

[37] P. Agarwal, M.J. Goossens, V. Zieren, E. Aksen, and J.W. Slotboom, "Impact ionization in thin silicon diodes," IEEE Electron Device Lett., vol. 25, no. 12, pp. 807-809, 2004.

[38] G. Wang, "Phonon emission in germanium and silicon by electrons and holes in applied

electric field at low temperature," J. Appl. Phys., vol. 107, p. 094504, 2010.

[39] P.A. Wolff, "Theory of optical radiation from breakdown avalanches in Germanium," J. Phys. Chem. Solids, vol. 16, pp. 184-190, 1960.

[40] M. Abramovitz, and I. Stegun, "Handbook of Mathematical Functions with Formulas, Graphs, and Mathematical Tables," Dover Publications, ISBN 486-61272-4, 1965.

[41] B.K. Ridley, "Lucky-drift mechanism for impact ionisation in semiconductors," J. Phys. C: Solid State Phys., vol. 16, pp. 3373-3388, 1983.

[42] H. Kurino, H. Kiba, H. Mori, S. Yokoyama, K. Yamaguchi, and M. Koyanagi, "Coupled Monte Carlo-energy relaxation analysis of hot carrier light emission in metal oxide semiconductor field effect transistors's," Jpn. J. Appl. Phys., vol. 30, no. 12B, pp. 3666-3670, 1991.

[43] M. Lax, "Cascade capture of electrons in solids," Phys. Rev., vol. 119, no. 5, pp. 1502-1523, 1960.

[44] E. Haug and W. Nakel, "The Elementary Process of Bremsstrahlung," World Scientific Lecture Notes in Physics, vol. 73, World Scientific Publ. Co. Pte. Ltd., 2004.

[45] M. Bartelmann, "Theoretical Astrophysics: An Introduction," Wiley-VCH Verlag GmbH & Co. KGaA, 2013.

[46] K. Rajkanan, R. Singh, and J. Schewchun, "Absorption coefficient of silicon for solar cell calculations," Solid-State Electronics, vol. 22, pp. 793-795, 1979.

[47] J. Kramer, P. Seitz, E.F. Steigmeier, H. Auderset, and B. Delley, "Light-emitting devices in industrial CMOS technology" Sensors and Actuators A, vol. 37-38, pp. 527-533, 1993.

[48] M. Morschbach, M. Oehme, and E. Kasper, "Visible light emission by a reverse-biased integrated silicon diode," IEEE Trans. Electron Devices, vol. 54, no. 5, pp. 1091-1094, 2007.

[49] L.W. Snyman, M. du Plessis, E. Seevinck, and H. Aharoni, "An efficient low voltage, high frequency silicon CMOS light emitting device and electro-optical interface," IEEE Electron Device Lett., vol. 20, no. 12, pp. 614-617, 1999.

[50] L. Qi, K.R.C. Mok, M. Aminian, E. Charbon, and L.K. Nanver, "UV-sensitive low dark-count PureB single-photon avalanche diode," IEEE Trans. Electron Devices, vol. 61, no. 11, pp. 3768-3774, 2014.

[51] L.K. Nanver, L.Qi, V. Mohammadi, K.R.C. Mok, W.B. de Boer, N. Golshani, A. Sammak, T.L.M. Scholtes, A. Gottwald, U. Kroth, and F. Scholze, "Robust UV/VUV/EUV PureB photodiode detector technology with high CMOS compatibility," J. Sel. Top. Quantum Electron, vol. 20, no. 6, pp. 1-11, 2014.

[52] M. du Plessis, and P. Rademeyer, "Novel electroluminescence technique to analyze mixed reverse breakdown phenomena in silicon diodes," Solid-State Electronics, vol. 54, pp. 433-438, 2010.

[53] K. Xu, L.W. Snyman, and H. Aharoni, "Si light-emitting device in integrated photonic CMOS ICs," Optical Materials, vol. 69, pp. 274-282, 2017.

[54] A. Richter, S.W. Glunz, F. Werner, J.Schmidt, and A. Cuevas, "Improved quantitative description of Auger recombination in crystalline silicon" Phys. Rev. B, vol. 86, pp.165202:1-14, 2012.

[55] H. Weinerth, "Silicon diode breakdown in the transition range between avalanche effect and field emission," Solid-State Electronics, vol. 10, pp. 1053-1062, 1967.

CHAPTER 3

# OPTICAL POWER EFFICIENCY OF CMOS AVALANCHE-MODE SILICON LEDS

**Abstract**

This chapter extends the opto-electronic model described in the previous chapter for diodes with different electric field profiles. The theoretical as well as the experimental dependency of the optical power efficiency $\eta_{opt}$ on the breakdown voltage $V_{BR}$ is presented for silicon avalanche-mode (AM) light-emitting diodes (LEDs). The model that subsumes non-local avalanche is first applied to two distinct ideal scenarios: (i) an abrupt $p^+$-n junction diode with a triangular field profile resulting in a maximum $\eta_{opt}$ for $V_{BR} \sim 5$ V, and (ii) a p-i-n diode with a uniform rectangular field profile resulting in a maximum $\eta_{opt}$ for $V_{BR} \sim 9$ V. Experimental validation of the modeled dependency is done using lateral $p^+$-n-$n^+$ LEDs designed in bulk CMOS technology. The lateral scaling in the active region tunes both the magnitude and the profile of the reverse electric field and hence those of the electron temperature; the latter governs AM electroluminescence. These LEDs have a trapezoidal electric field profile, thus deviating from the ideal scenarios. Experiments show that a maximum $\eta_{opt}$ is obtained for $V_{BR} \sim 6$ V. This trend is further shown to be in agreement with our model, where the TCAD simulated field profile for each LED is used as the model input. A maximum in $\eta_{opt}$ at relatively low voltages is important for monolithic opto-electronic integration in silicon.

*"It is not knowledge, but the act of learning, not possession but the act of getting there, which grants the greatest enjoyment."* (C.F. Gauss)

This chapter is an extension of a publication in IEEE Electron Device Letters [1].

## 3.1 Introduction

The avalanche-mode light-emitting diode (AMLED) is a potential candidate as a silicon (Si) based light source for monolithic opto-electronic integration in standard CMOS technology, e.g. optical links [2, 2–7, 9], primarily due to the significant overlap between its electroluminescent (EL) spectra and the spectral responsivity of Si photodiodes (PDs) [2, 9]. Avalanche-mode electroluminescence (AM-EL) is governed by impact ionization [10] and hence by the electron temperature [11]. The relatively low internal quantum efficiency (IQE) of AMLEDs ($\sim 10^{-5}$) [4] combined with the relatively high p-n junction breakdown voltages $V_{BR}$ make AM-EL to be significantly power-hungry. Thus, maximizing the optical power efficiency $\eta_{opt}$, defined as the ratio of the optical power $P_{opt}$ to the electrical power $P_{LED}$ [12], is highly desired.

The existence of an optimum $V_{BR} \sim 5$ V at which $\eta_{opt}$ is maximum was reported earlier [13], based on devices in a BiCMOS process, where measured values of $\eta_{opt}$ were fitted with an empirical model. However, the underlying physical mechanism was not explained. In addition, experimental data for low $V_{BR}$ are scarce. Given that the model presented in the previous chapter also predicts an efficiency optimum, again around $V_{BR} \sim 5$ V for an abrupt optimized 1-D $p^+$-n junction (i.e. for a single-sided triangular electric field profile), an experimental investigation of AMLED efficiency at low $V_{BR}$ values is attractive.

In this chapter, we continue our discussion on the opto-electronic model to study the dependency of the optical power efficiency on the breakdown voltage for two ideal one-dimensional scenarios: (i) an abrupt $p^+$-n junction diode with a triangular field profile, and (ii) a p-i-n diode with a uniform rectangular field profile. The optical intensity is related to the field-dependent $T_e$-profile using a non-local avalanche model [11, 14–16]. The case of an ideal p-i-n diode is particularly interesting, because a higher optical efficiency is expected than in the case of the abrupt $p^+$-n junction diode due to a more uniform field profile in the former. For example, in superjunction LEDs [17] (described in Chapter 4), increasing the spatial uniformity of the electric field led to an enhancement in the optical power.

In order to validate the modeled result, an experimental relation between $\eta_{opt}$ and $V_{BR}$ is obtained using lateral nanometer-scale $p^+$-n-$n^+$ junction diodes designed in a standard 65 nm bulk CMOS technology. Here, $V_{BR}$ has been varied by geometric scaling of the LED, resulting in a trapezoidal field-profile $F(x)$ for a fixed doping level $N$ determined by the technology. Results are then compared with our model presented in Chapter 2, where the TCAD simulated field profile for each LED is used as the model input. A comparison is also done with the earlier proposed model of [13].

## 3.2 Opto-electronic model revisited

We begin by reproducing the core equation from chapter 2 that relates $T_e(x)$ with the electric field $F(x)$:

$$T_e(x) = T_0 + \frac{2q}{5k_B} \int_0^x F(u) \exp\left[\frac{u-x}{\lambda_e}\right] du, \tag{3.1}$$

where $q$ is the elementary charge, $T_0$ is the lattice temperature, $k_B$ is the Boltzmann constant, and $\lambda_e \propto v_e \cdot \tau_e$ is the mean energy relaxation length for electrons with velocity $v_e$ as defined in [15, 16], where $\lambda_e$ = 65 nm was reported for Si. Here $\tau_e$ is the mean inter-scattering time in Si, which depends on $T_0$ and is governed by acoustic deformation potential (ADP) scattering [18]. In chapter 2, Eq. (3.1) was already solved for a triangular $F(u)$ as in an abrupt $p^+$-n diode with a depletion width $W_{dep}$, which gave us:

$$T_e(x) = T_0 + \frac{2qF_m\lambda_e}{5k_B}\left[1 - \frac{(x-\lambda_e)}{W_{dep}} - \left(1 + \frac{\lambda_e}{W_{dep}}\right)\exp\left(\frac{-x}{\lambda_e}\right)\right]. \tag{3.2}$$

Similarly, Eq. (3.1) can be solved for an ideal p-i-n diode with a uniform field $F_{pin}$ spread across an intrinsic (or active) layer of width $W$, which yields:

$$T_e(x) = T_0 + \frac{2qF_m\lambda_e}{5k_B}\left[1 - \exp\left(\frac{-x}{\lambda_e}\right)\right], \tag{3.3}$$

where $x$ ranges from 0 to $W$.

Fig. 3.1(a) depicts the electron temperature profile for an ideal $p^+$-n diode and a p-i-n diode having the same $V_{BR}$ (chosen to be 12 V as an example). In our model $V_{BR}$ is defined electrostatically from the ionization integral as described in the previous chapter. Moreover, $V_{BR}$ in the $p^+$-n diode is tuned by varying the doping level N, while the same is achieved in the p-i-n diode by varying $W$. In the former case, the applied electric field decreases linearly from $x$ = 0 to $x$ = $W_{dep}$, while in the latter, the applied field is a constant from $x$ = 0 to $x$ = $W$ (as shown in Fig. 3.1(b)). For the same $V_{BR}$, $F_m$ and hence the peak $T_e$ is higher for the $p^+$-n diode. On the other hand, $F(x)$ and $T_e(x)$ are spatially more uniform for the p-i-n diode. Note that $T_e(x)$ governs the optical intensity at $x$ according to our model. Fig. 3.2(a) shows the variation in the peak and average $T_e$ with varying $V_{BR}$ for the p-i-n and the $p^+$-n diodes. The difference in the spatial uniformity of $F(x)$ results in a much smaller average $T_e$ in case of the $p^+$-n diode as compared to that of the p-i-n diode. This difference has a direct impact on the optical power in avalanche-mode operation of the LED. When $P_{opt}$ is calculated using the average $T_e$, the model predicts the dependency of the efficiency $\eta_{opt}$ (= $P_{opt}/P_{LED}$) on the theoretical

$V_{BR}$, as shown in Fig. 3.2(b). It deserves mention that the comparison is done assuming the same current density level for each $V_{BR}$. Moreover, our model only yields a relative comparison. As such, the plotted $\eta_{opt}$ has been normalized w.r.t. its maximum value, for clarity. In both kind of diodes, there exists a certain optimum $V_{BR} = V_p$, at which $\eta_{opt}$ attains its maximum value. This happens at roughly 5 V for the $p^+$-n diode, and at roughly 9 V for the p-i-n diode. The reduction of $\eta_{opt}$ for $V > V_{BR}$ is a consequence of reducing $F_m$, and thereby reducing peak $T_e$. When $V_{BR}$ is reduced below $V_p$, the corresponding $W$ or $W_{dep}$ reduces to a value of the same order as the energy relaxation length $\lambda_e$. Thus the peak $T_e$ drops (as already derived in chapter 2). This translates to a rapid decrease in the optical power. The reason why $V_p$ is different for the $p^+$-n and the p-i-n diode is simply because the dependency of $V_{BR}$ on $W_{dep}$ (for the former) and that on $W$ (for the latter) is different.

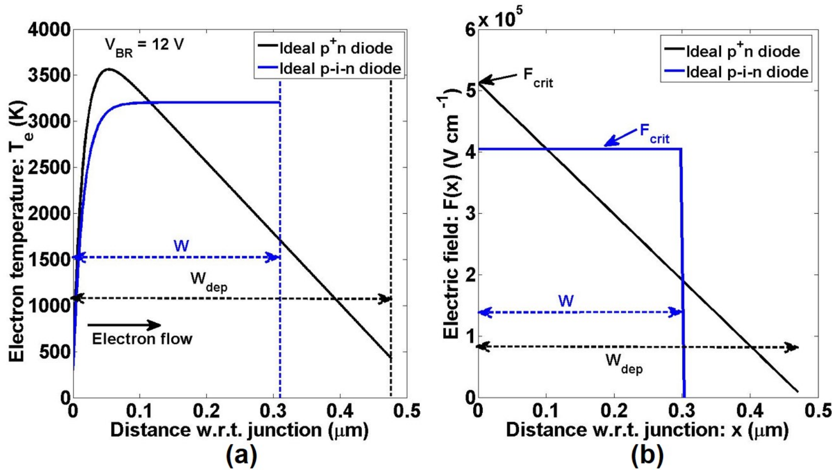


Figure 3.1: Modeled (a) electron temperature profile and (b) electric field profile computed at the same $V_{BR}$ = 12 V for an ideal $p^+$-n diode (Eq. (3.2)) and an ideal p-i-n diode (Eq. (3.3)). The single-sided arrow represents the direction of electron flow.

In order to validate the modeled outcome for abrupt $p^+$-n diodes, one should ideally design an experiment where N is changed to tune $V_{BR}$ in a sufficient number of steps while keeping the EL-area of the diodes the same. This would change the critical field while maintaining a triangular field-profile. Such an experimental validation encounters several challenges, especially when experimentation is limited to the outreach of standard CMOS technology. Firstly, in the case of the abrupt $p^+$-n diode, the model not only considers $V_{BR}$ being varied by varying N, but also assumes that the effective EL-area is more or less constant. In practice, varying N means selecting a wide range of doses of implants for the dopant species. The

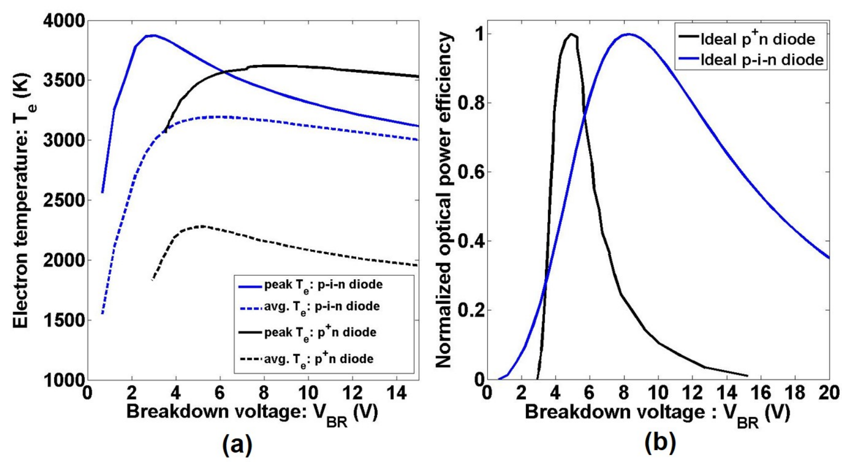


Figure 3.2: Modeled (a) peak and average electron temperature versus $V_{BR}$, and (b) optical power efficiency versus $V_{BR}$ for an ideal $p^+$-n diode and an ideal p-i-n diode, adopting the average $T_e$.

choices for values of N are typically quite limited in CMOS technology. Secondly, as discussed in the previous chapter, changing N also alters the distribution of the EL-area, which complicates the head-on comparison among different test devices. Realizing an ideal p-i-n diode is also not feasible in standard CMOS, because Si is always doped which results in non-uniformity in the electric field profile. One requires advanced technologies for e.g. ultra-thin fully-depleted SOI, to utilize near-intrinsic Si layers.

A simple design solution to validate the model is to realize $p^+$-n-$n^+$ diodes in standard CMOS, where $V_{BR}$ can be tuned by varying the spacing between the $p^+$ and $n^+$ layers, i.e. the length $d$ of the active n-layer. To achieve desirably low values of $V_{BR}$, the allowed precision in $d$ should be high. Moreover, very small values of $d$ ($\sim \lambda_e$) should be allowed by the design rules. This motivated us to choose an advanced 65 nm bulk CMOS technology from TSMC (Taiwan Semiconductor Manufacturing Company). In the next section, we describe the experimental results followed by a discussion on the opto-electronic model.

## 3.3 Experimental results

### 3.3.1 Design of the LED

Fig. 3.3 (a) shows the device top-view and (b) shows the vertical cross-section of the designed $p^+$-n-$n^+$ LEDs. Each LED has a fixed total length $L \approx 6.5$ µm along the $x$-axis, and a fixed width $W = 47.6$ µm along the $y$-axis. The designed spacing $d$ between the $n^+$ and $p^+$ region is varied

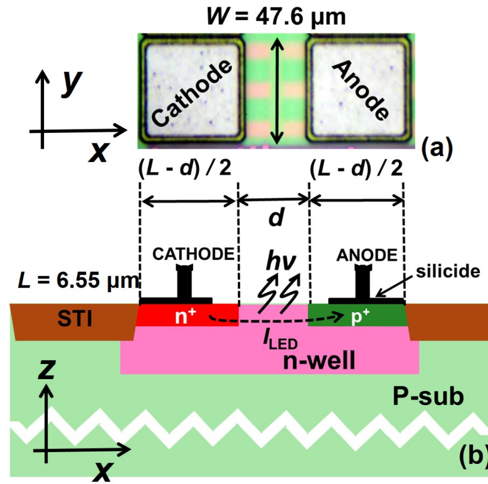


Figure 3.3: Schematic (a) top-view and (b) cross-section of the $p^+$-n-$n^+$ LED. The spacing d between the $p^+$ and $n^+$ regions has been varied in steps of 20 nm.

from d = 0 in LED D1 to d = 280 nm in LED D15, in steps of 20 nm. D1 is a special case of a $p^+$-$n^+$ junction. The silicide layer is avoided along the active region except at the electrode contacts. This is required for two reasons. Firstly, the silicide provides an ohmic contact at the individual electrodes. Since there is no shallow trench isolation between the $p^+$ and $n^+$ layers, a silicide break between them prevents shorting of the junction. Secondly, the silicide break also enables vertical emergence and detection of light. The small values of d together with the small depth of the junction (~ 100-200 nm) ensures breakdown and hence light emission to occur close to the Si surface, which in turn ensures a low absorption of light within the Si LED.

### 3.3.2 Electrical behavior

Fig. 5.2(a) shows the measured dc reverse I-V characteristics of the LEDs D1 to D6, D8, D10, and D12 with an increasing d, in dark conditions and at ambient temperatures $T = T_0$ = 25 $^{O}$C and 75 $^{O}$C. The I-V curves for the rest of the diodes are not shown for figure clarity. For $d \leqslant 60$ nm (D1 to D4), the reverse current $I_{LED}$ has a negligible T-dependence, and a sub-unity ideality factor (as low as ~ 0.38 for D1 at 0.2 V corresponding to a slope of 23 mV/decade) indicating the presence of band-to-band tunneling (BTBT) [19, 20]. This leads to a "soft" transition into breakdown. For $d > 80$ nm (D6 onwards), the I-V curves show a progressively sharper transition into breakdown, and a more pronounced T-dependence, indicating impact ionization and avalanche breakdown [21]. For D12, the lowest observed swing at breakdown is ~ 25 mV/decade.

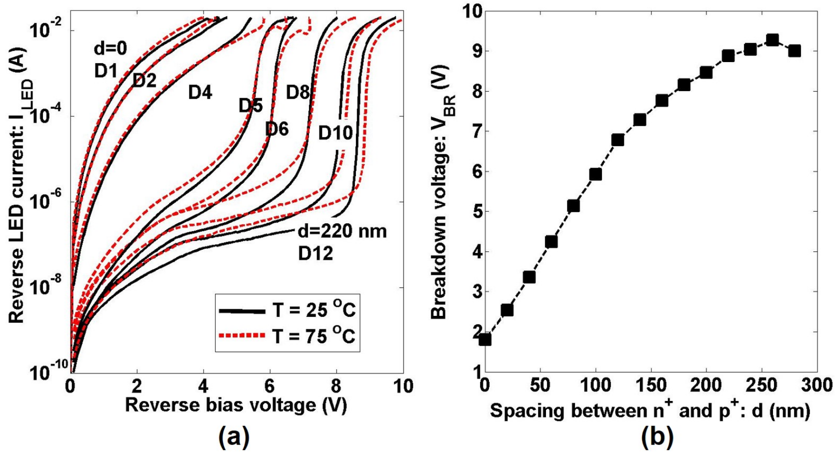


Figure 3.4: (a) Measured dc I-V characteristics (in dark) of the LEDs D1 to D6, D8, D10, and D12 at T = 25 $^{O}$C and 75 $^{O}$C. Measurements were done using a Keithley 4200 Semiconductor Characterization System (SCS). (b) $V_{BR}$ versus d defined from the measured I-V characteristics.

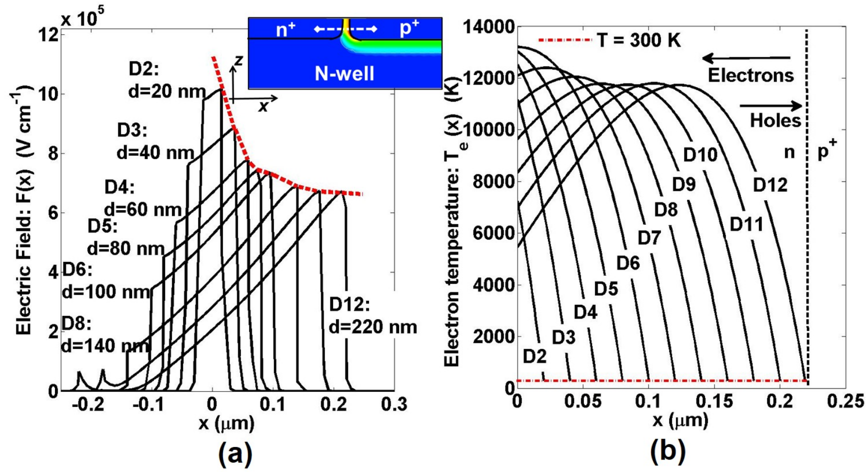


Figure 3.5: (a) TCAD simulated field profiles F(x) at breakdown for the indicated LEDs along the white dashed cut-line (z = -0.1 μm) shown in the inset. The red dashed line is a guide to the eye for the peak field trend. (Inset): 2-D TCAD simulated electric field profile at breakdown, for d = 40 nm. (b) Calculated electron temperature profiles $T_e(x)$ following Eq. (3.1) for the indicated LEDs. The arrows indicate the direction of the electron and hole current flow.

The $V_{BR}$ of the LEDs is defined (arbitrarily) at a fixed current $I_{LED}$ = 1 mA for each LED, and plotted against d in Fig. 5.2(b). The trend in $V_{BR}$ is explained by the two dimensional (2-D) TCAD simulated [22] F(x) at $V \approx V_{BR}$, as shown in Fig. 3.5(a). The inset of Fig. 3.5(a) shows a snapshot of the 2-D field profile for d = 40 nm. An effective $N \sim 10^{17}$ cm$^{-3}$ has

been obtained by fitting the measured $V_{BR}$ in TCAD for the largest diode D15. $F(x)$ is trapezoidal for fully depleted short diodes. With increasing $d$, the peak field $F_m$ rapidly reduces to a value corresponding to that of an abrupt $p^+$-n junction, while the depletion width increases to its maximum, where $F(x)$ becomes roughly triangular. The AM-EL is dependent on $T_e$ as expressed by the model, which is computed by using the TCAD simulated $F(x)$ in Eq. (3.1).

The calculated $T_e(x)$ is shown for the indicated LEDs in Fig. 3.5(b). From D2 to D6 ($d < 2\ \lambda_e$), the peak $T_e$ first rapidly increases due to non-local avalanche, and then for $d > 2\ \lambda_e$ it gradually reduces from D7 onwards due to the gradual reduction in $F_m$.

The peak $T_e$ is used to evaluate the carrier probability distribution functions, which are then used to calculate the total optical power $P_{opt}$ by integrating all the electron transitions to the valence band edge [11, 23], as done in the previous chapter. Next, we discuss the optical properties of the LEDs.

### 3.3.3 Optical behavior

Fig. 3.6 shows the AM-EL micrographs of the LEDs at $I_{LED}$ = 5 mA, captured vertically using a visible range camera. Light emission appears along the line of the junction oriented along the $y$-axis. The brightness is observed to increase rapidly from D1 to D6, and then saturates from D7 onwards.

Fig. 3.7 shows the measured spectral irradiance of D6 ($V_{BR} \approx 6$ V) at various $I_{LED}$. These EL-spectra (observed in the spectral range of 400 nm $< \lambda <$ 900 nm) have been corrected for the effect of Fabry-Perot interference in the multi-layer back-end dielectric stack, which has been characterized by its spectral transmittance using a broad-spectrum halogen lamp from Bausch and Lomb. This procedure is described in Appendix B. The EL-spectra exhibit a broad peak centered at $\lambda \sim 620$ nm that can be attributed to phonon-assisted (indirect) inter-band recombination. The emission at $\lambda \gtrsim 700$ nm can also be contributed by intra-band electron transitions, while emission at $\lambda \lesssim 480$ nm can be partly contributed by direct inter-band recombination [24–26]. A significant lowering in the relative irradiance has also been observed in the range 500 nm $< \lambda <$ 550 nm in all the LEDs irrespective of the electrical bias. The reason behind this phenomenon is not clear yet, and also requires further study.

A linear increase in $P_{opt}$ emitted by the LEDs with increasing $I_{LED}$ is observed, as shown for D6 in Fig. 3.9(a), with an internal $\eta_{opt} \approx 1.7 \times 10^{-6}$, corresponding to a mean intensity of $\sim 28$ nW $\mu$m$^{-2}$ at $I_{LED}$ = 10 mA. $P_{opt}$ has been measured using an ultra-sensitive, off-chip calibrated photodi-

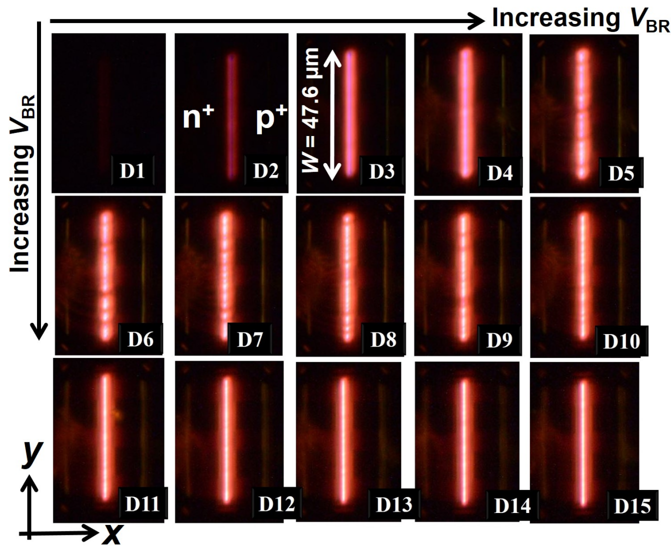


Figure 3.6: AM-EL micrographs of the LEDs D1 to D15, each at $I_{LED}$ = 5 mA (to the same scale and resolution). Light is captured vertically (out of plane along the *z*-axis). The images are captured by a visible range camera with a 20 s integration time.

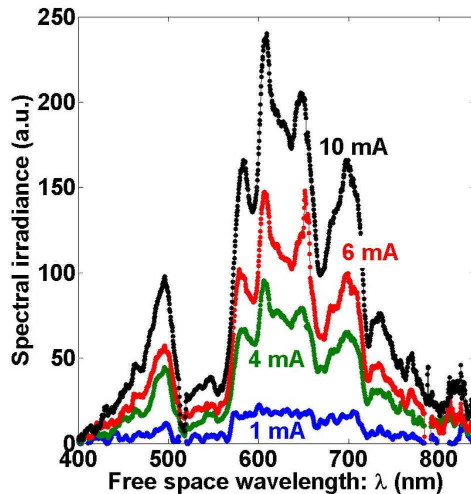


Figure 3.7: Vertically measured EL-spectra of D6 for various $I_{LED}$, measured using a multi-mode optical fiber feeding an ADC-1000-USB spectrometer from Avantes, with an integration time of 20 s.

ode (PD) [27], mounted vertically above the die (see Fig. 3.8), which is done by extracting the emission-specific responsivity of the PD [9]. The concept of emission-specific responsivity will be discussed in chapter 5. The external and internal quantum efficiencies (EQE and IQE) of D6 have

been estimated to be $\sim 2.0\times10^{-8}$ and $\sim 6.0 \times 10^{-6}$, respectively, assuming isotropic light emission [10]. The obtained IQE and EQE values match well with prior results [4, 24, 28].

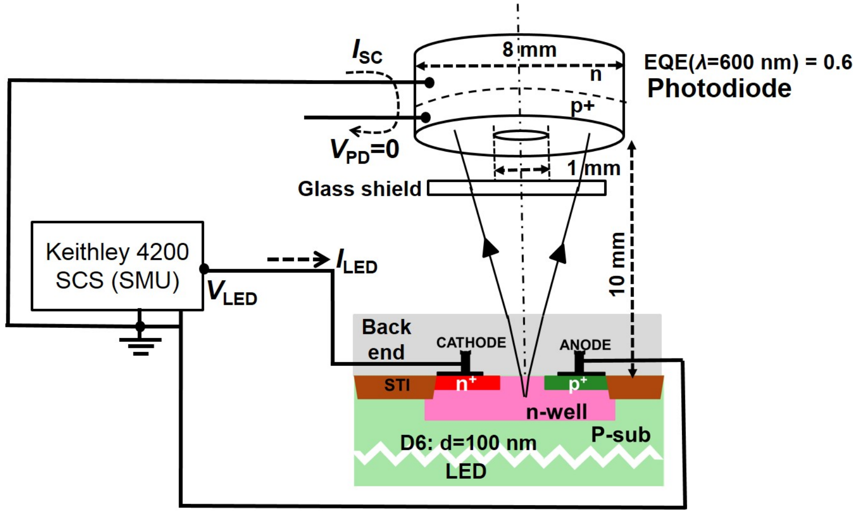


Figure 3.8: Schematic of the measurement set-up to measure $P_{opt}$ using an off-chip calibrated photodiode.

The same linear variation in $P_{opt}$ versus $I_{LED}$ has been observed by integrating the measured EL-spectra over $\lambda$. In Fig. 3.9(b), $\eta_{opt}$ is plotted against $V_{BR}$ of the LEDs, where it is normalized w.r.t. its maximum value (for D6). The normalization is done for comparison with the modeled trends.

The trends in $\eta_{opt}$ versus $V_{BR}$ for the LEDs, as predicted by our opto-electronic model [11], along with the one predicted by the previously published model of [13] are also shown in Fig. 3.9(b). Our model for $\lambda_e = 65$ nm [15] is in better agreement with the measured trend, where trapezoidal field profiles have been considered. A maximum $\eta_{opt}$ is obtained in our experiment for $V_{BR} \sim 6$ V. For $V_{BR} < 6$ V, non-local avalanche leads to a rapid decrease in $\eta_{opt}$ with decreasing $V_{BR}$ (thus decreasing d) despite an increasing $F_m(d)$. This can be understood as follows: when $d \lesssim \lambda_e$, the electrons do not have sufficient space to be accelerated to high energies. Hence, the peak $T_e$ drops, leading to a drop in $P_{opt}$.

For $V_{BR} > 6$ V (LEDs D7 to D15), a continuous reduction in $\eta_{opt}$ with increasing $V_{BR}$ is obtained. This is mainly due to the fact that $F_m$ reduces for increasing d as $F(x)$ changes from being trapezoidal to triangular. This is reflected in the increase of $V_{BR}$, and hence $P_{LED}$.

The discrepancies between the modeled and measured $\eta_{opt} - V_{BR}$ curves are likely due to the uncertainties in N, d, and the assumption of a 1-D EL-region in the optical model. Further, BTBT [19, 20, 29] has not

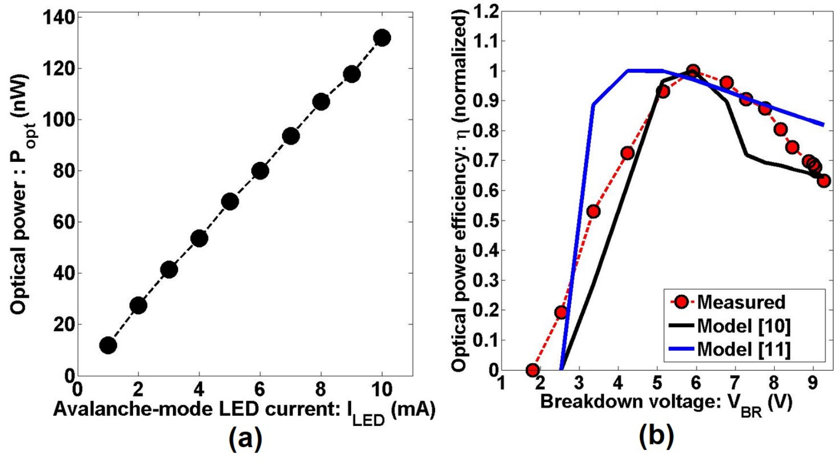


Figure 3.9: (a) Emitted optical power of the avalanche-mode LED D6 versus $I_{LED}$. (b) Normalized optical power efficiency versus $V_{BR}$, where the experimental trend is compared with those predicted using the 1-D opto-electronic model (with peak $T_e$) [11] and the previously reported model [13].

been taken into account in the model. BTBT is the most pronounced in D1 (explaining its low $P_{opt}$), being a $p^+$-$n^+$ junction.

At this point, in order to make sense out of our analysis, we revisit our modeled predictions for the ideal scenarios (p-i-n and $p^+$-n diode) in the light of the experimental results. Fig. 3.10 helps us in developing an insight for the same. The figure combines Fig. 3.2(b) with the measured trend in $\eta_{opt}$ in one plot. The modeled curves for the ideal $p^+$-n and the ideal p-i-n diode can be considered as two extreme scenarios, whereas the experimental devices dealt herein have trapezoidal field profiles, which can be visualized as something intermediate to the two ideal scenarios. Consequently, the experimental $\eta_{opt}$-$V_{BR}$ curve also shows an intermediate behavior with a maximum $\eta_{opt}$ occurring at $V_{BR}$ = 6 V.

As a side remark, the LEDs were tested for their reliability via an accelerated stress of 30 hours operation at a dc bias of $I_{LED}$ = 10 mA and 100 $^{o}$C ambient. No degradation in the total $P_{opt}$ has been observed, in line with previous reports of bulk CMOS AMLEDs [30]. However, one can expect hot-carrier induced electrical degradation, due to the high field near the Si-$SiO_2$ interface [31, 32], resulting in higher leakage currents and reduced $V_{BR}$.

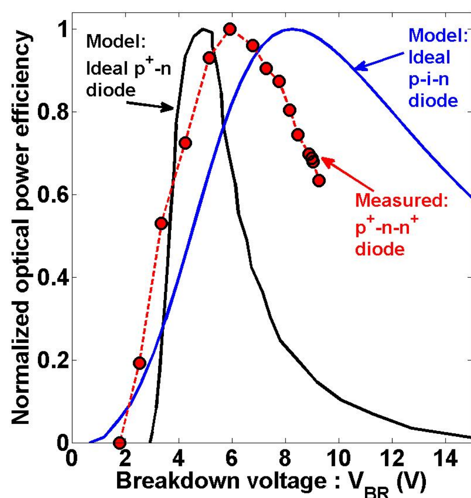


Figure 3.10: Modeled optical power efficiency versus $V_{BR}$ for an ideal $p^+$-n diode and an ideal p-i-n diode, shown alongside the measured trend for the $p^+$-n-$n^+$ LEDs.

## 3.4 Conclusions

The dependency of optical power efficiency $\eta_{opt}$ on the breakdown voltage $V_{BR}$ of avalanche-mode (AM) $p^+$-n-$n^+$ junction LEDs in silicon, designed in a standard 65 nm bulk CMOS technology, has been shown experimentally and compared with models. Measurements show a maximum $\eta_{opt}$ at $V_{BR} \sim 6$ V. For $V_{BR} < 6$ V, a rapid decrease in $\eta_{opt}$ is obtained for decreasing $V_{BR}$ despite an increase in the peak electric field. For $V_{BR} > 6$ V, a reduction in $\eta_{opt}$ with increasing $V_{BR}$ is obtained due to a gradual reduction in both the magnitude and the spread of the electric field. The measurements are explained with our opto-electronic model that relates AM electroluminescence from Si LEDs to the field-dependent electron temperature based on the non-local avalanche effect.

# BIBLIOGRAPHY


[1] S. Dutta, G.J.M. Wienk, R.J.E. Hueting, J. Schmitz, and A.J. Annema, “Optical power efficiency versus breakdown voltage of avalanche-mode silicon LEDs in CMOS,” IEEE Electron Device Lett., vol. 38, no. 7 , pp. 898-901, 2017.

[2] B.P. van Drieënhuizen and R.F. Wolffenbuttel, “Optocoupler based on the avalanche light emission in silicon,” Sensors and Actuators A, vol. 31, no. 1-3, pp. 229-240, 1992.

[3] M. du Plessis, H. Aharoni, and L.W. Snyman, “Silicon LEDs fabricated in standard VLSI technology as components for all silicon monolithic integrated optoelectronic systems,” IEEE J. Sel. Topics Quantum Electron., vol. 8, no. 6, pp. 1412-1419, 2002.

[4] L.W. Snyman, M. du Plessis, and H. Aharoni, “Injection-avalanche-based $n^{+}pn$ silicon complementary metal oxide semiconductor light-emitting device (450 - 750 nm) with 2-order-of-magnitude increase in light emission intensity,” Jpn. J. Appl. Phys., vol. 46, no. 4B, pp. 2474-2480, 2007.

[5] B. Huang, X. Zhang, W. Wang, Z. Dong, N. Guan, Z. Zhang, and H. Chen, “CMOS monolithic optoelectronic integrated circuit for on-chip optical interconnection,” Opt. Commun., vol. 284, no. 16-17, pp. 3924-3927, 2011.

[6] A. Khanmohammadi, R. Enne, M. Hofbauer, and H. Zimmermann, “Monolithic integrated optical random pulse generator in high voltage CMOS technology,” Proc. 45th ESSDERC, pp. 138-141, 2015.

[7] K. Xu, “Silicon light-emitting device in standard CMOS technology,” Proc. 8th International Photonics and OptoElectronics Meetings, OSA Tech. Digest, p. OT1C.3, 2015.

[8] S. Dutta, R.J.E. Hueting, V. Agarwal, and A.J. Annema, “An integrated optical link in 140 nm SOI technology,” Proc. Conference on Lasers and Electro-Optics, Session JW2A, p. 132, 2016.

[9] S. Dutta, V. Agarwal, R.J.E. Hueting, J. Schmitz, and A.J. Annema, “Monolithic optical link in silicon-on-insulator CMOS technology,” Optics Express, vol. 25, no. 5, pp. 5440-5456, 2017.

[10] A.G. Chynoweth and K.G. McKay, “Photon emission from avalanche breakdown in silicon,” Phys. Rev., vol. 102, no. 2, pp. 369-376, 1956.

[11] S. Dutta, R.J.E. Hueting, A.J. Annema, L. Qi, L.K. Nanver and J. Schmitz, “Opto-electronic modeling of light emission from avalanche-mode silicon $p^{+}n$ junctions,” J. Appl. Phys., 118, 114506, 2015.

[12] E.F. Schubert, “*Light Emitting Diodes*,” (Cambridge University Press, 2006).

[13] P.I. Kuindersma, T. Hoang, J. Schmitz, M.N. Vijayaraghavan, M. Dijkstra, W. van Noort, T. Vanhoucke, W.C.M. Peters, and M.C.J.C.M. Kramer, “The power conversion efficiency of visible light emitting devices in standard BiCMOS processes,” Proc. $5^{th}$ IEEE International Conf. on Group IV Photonics, pp. 256-258, 2008.

[14] G.J. Rees and J.P.R. David, “Nonlocal impact ionization and avalanche multiplication,” J. Phys. D: Appl. Phys., vol. 43, p. 243001, 2010.

[15] J.W. Slotboom, G. Streutker, M.J. van Dort, P.H. Woerlee, A. Pruijmboom, and D.J. Gravesteijn, “Non-local impact ionization in silicon devices,” Proc. IEEE International Electron Devices Meeting (IEDM), pp. 127-130, 1991.

[16] P. Agarwal, M.J. Goossens, V. Zieren, E. Aksen, and J.W. Slotboom, "Impact ionization in thin silicon diodes" IEEE Electron Device Lett., vol. 25, no. 12, pp. 807-809, 2004.

[17] S. Dutta, P.G. Steeneken, V. Agarwal, J. Schmitz, A.J. Annema, and R.J.E. Hueting, "The avalanche-mode superjunction LED," IEEE Trans. Electron Devices, vol. 64, no. 4, pp. 1612-1618, 2017.

[18] M. Lundstrom, "*Fundamentals of carrier transport*," 2$^{nd}$ edition, Cambridge University Press, 2000.

[19] G.A.M. Hurkx, D.B.M. Klaassen, and M.P.G. Knuvers, "A new recombination model for device simulation including tunneling," IEEE Trans. Electron Devices, vol. 39, no. 2, pp. 331-338, 1992.

[20] J.J. Liou, "Modeling the tunneling current in reverse-biased p/n junctions," Solid-State Electronics, vol. 33, no. 7, pp. 971-972, 1990.

[21] R. van Overstraeten and H. de Man, "Measurement of the ionization rates in diffused silicon p-n junctions," Solid-State Electronics, vol. 13, no. 1, pp. 583-608, 1970.

[22] "Sentaurus TCAD," version L-2016.03, Synopsys Inc., Mountain View, CA, USA, 2016.

[23] M. Lahbabi, A. Ahaitouf, M. Fliyou, E. Abarkan,J.-P. Charles, A. Bath, A. Hoffmann, S.E. Kerns and D.V. Kerns, Jr., "Analysis of electroluminescence spectra of silicon and gallium arsenide p-n junctions in avalanche breakdown," J. Appl. Phys., vol. 95, no.4, pp. 1822-1828, 2004.

[24] L.W. Snyman, J-L. Polleux, K. A. Ogudo, C. Viana, and S. Wahl, "High intensity 100 nW 5 GHz silicon avalanche LED utilizing carrier energy and momentum engineering," proc. SPIE, vol. 8990, 89900L, Silicon Photonics IX, 2014.

[25] L.W. Snyman, K. Xu, J-L. Polleux, K. A. Ogudo, and C. Viana, "Higher intensity SiAvLEDs in an RF bipolar process through carrier energy and carrier momentum engineering," IEEE J. Quantum Electron., vol. 51, no. 7, 3200110, 2015.

[26] L.W. Snyman, and K. Xu, "Stimulation of 450, 650 and 850 nm optical emissions from custom designed silicon LED devices by utilizing carrier energy and carrier momentum engineering," proc. SPIE, vol. 10036, 1003603, 2017.

[27] K.R.C. Mok, L. Qi, A.H.G. Vlooswijk, and L.K. Nanver, "Self-aligned two-layer metallization with low series resistance for litho-less contacting of large-area photodiodes," Solid-State Electronics, vol. 111, pp. 210-217, 2015.

[28] K. Xu, Q. Yu, and G. Li, "Increased efficiency of silicon light-emitting device in standard Si-CMOS technology," IEEE J. Quantum Electron., vol. 51, no. 8, 3000106, 2015.

[29] S.M. Sze and K.K. Ng, "*Physics of Semiconductor Devices*," 3$^{rd}$ edition, John Wiley & Sons, Inc., USA, 2007.

[30] A. Chatterjee, and B. Bhuva, "High speed, high reliability Si-based light emitters for optical interconnects," proc. IEEE International Interconnect Technology Conference, pp. 86-88, 2002.

[31] P.K. Gopi, G.P. Li, G.J. Sonek, J. Dunkley, D. Hannaman, J. Patterson, and S. Willard, "New degradation mechanism associated with hydrogen in bipolar transistors under hot carrier stress," Appl. Phys. Lett., vol. 63, no. 9, pp. 1237-1239, 1993.

[32] B.K. Boksteen, S. Dhar, A. Ferrara, A. Heringa, R.J.E. Hueting, G.E.J. Koops, C. Salm, and J. Schmitz, "On the degradation of field-plate assisted RESURF power devices," proc. IEEE International Electron Device Meeting, pp. 311-314, 2012.

CHAPTER 4

# The Avalanche-Mode Superjunction Light Emitting Diode

**Abstract**

Avalanche-mode light-emitting diodes (AMLEDs) in silicon (Si) are potential light sources to enable monolithic optical links in standard CMOS technology, due to the large overlap of their electro-luminescent (EL) spectra with the responsivity of Si photo-diodes. These EL spectra depend on the reverse electric field. In this chapter, AMLEDs employing the superjunction (SJ) assisted reduced surface field (RESURF) effect are presented, which increases the uniformity of their electric field profile. Consequently, the EL area of these lateral devices is significantly enlarged as compared to conventional AMLEDs. Electrical and optical measurements demonstrate RESURF, as confirmed by TCAD simulations, and show a direct link between EL-intensity (optical power per unit device area) and the field-profile. Contrary to a conventional AMLED, the breakdown voltage of the avalanche-mode SJ-LED scales with the device length. Further, the brightest SJ-LED, with a lateral intensity of ~ 30 mW cm$^{-2}$ at an electrical power ($P_{AMLED}$) of 0.1 W, shows a 2-fold higher internal quantum efficiency and a 3-fold higher EL-intensity compared to the conventional AMLED for the same $P_{AMLED}$. This particular SJ-LED further shows an optimum radiative recombination efficiency at a current density of around ~ 800 A cm$^{-2}$.

*"For a successful technology, reality must take precedence over public relations, for Nature cannot be fooled."* (R.P. Feynman)

This chapter is an extension of a publication in IEEE Transactions on Electron Devices [1].

## 4.1 Introduction

The electro-luminescence in avalanche-mode (AM-EL) silicon p-n junctions is governed by impact ionization [2] and hence, by the reverse electric field $F$ [3]. The main challenge, however, has been the relatively lower radiative efficiency of AMLEDs (~$10^{-5}$) [4] as compared to that of forward biased LEDs (~$10^{-3}$) [5], which can be compensated by integrating them with single photon avalanche diodes (SPADs) [6] as detectors, which are sensitive to a few photons. SPADs can offer high speed optical data communication [6] if sufficient number of photons are received per (data) bit. To increase both power efficiency and attainable bandwidth, the EL-intensity (optical power per unit device area) and hence the internal quantum efficiency (IQE) of the LEDs should be enhanced [7]. Earlier, enhanced AM-EL was demonstrated through enhanced injection (current density) [4, 8], carrier momentum and carrier energy engineering [7] with reported intensities of up to 200 nW $\mu m^{-2}$.

In the previous chapter, we discussed that as long as the breakdown voltage ($V_{BR}$) of an AMLED is above ~ 6 V, the EL-intensity is strongly dependent on both the magnitude and the spatial distribution of the electric field, while below 6 V the non-local avalanche effect becomes important and mainly the magnitude of the field governs the EL-intensity. However, this discussion was limited to a 1-D field profile (triangular and trapezoidal). In this chapter, we show an alternative way to engineer the field profile in 2-D, and investigate how it affects $V_{BR}$ and thereby the EL-intensity. We improve the spatial uniformity of $F$ and consequently the IQE of the LED in a standard 140 nm silicon-on-insulator (SOI)-CMOS technology [9]. This is achieved using the superjunction (SJ) assisted reduced surface-field (RESURF) concept [10–13]. Although the SJ concept has been used in Si power devices [14–18] to overcome the $V_{BR}$ versus on-resistance ($R_{ON}$) trade-off, it has not yet been used in LEDs. The proposed avalanche-mode SJ-LEDs are lateral multi-finger diodes.

The chapter is organized as follows. Section 4.2 describes the theoretical background and the structural design of the SJ-LEDs. Section 4.3 discusses the electrical and optical behavior of the SJ-LEDs along with an implementation example of a monolithic lateral optical link designed in the same technology. Section 6.5 provides the main conclusions.

## 4.2 Theory and Design of Device

### 4.2.1 Background

Fig. 4.1 (a) shows the schematic top-view and the sketch of the triangular field-profile $F(x)$ of an abrupt, symmetric p-n junction [19]. The SJ diode consists of alternate p- and n-doped fingers as shown in Fig. 4.1 (b), where

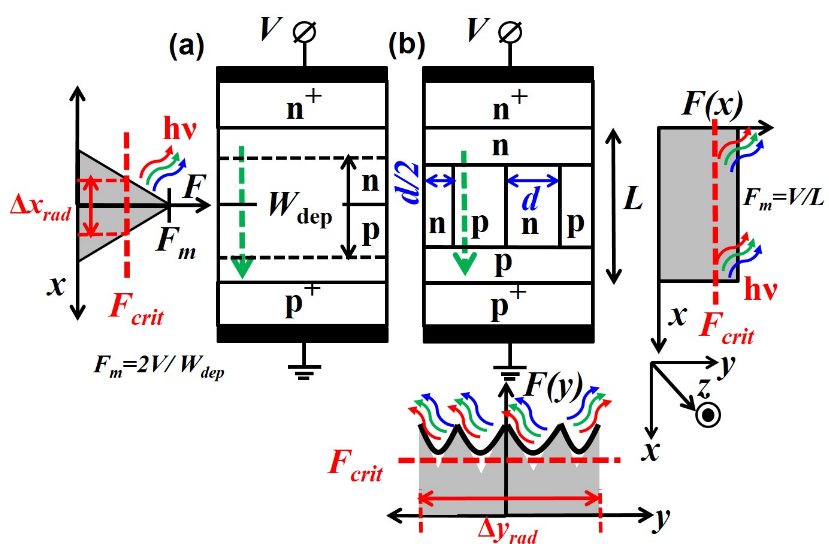


Figure 4.1: Schematic top-view of device and field profiles for (a) an abrupt symmetric p-n junction, and (b) a superjunction diode, which increases the uniformity of the magnitude of $F(x,y)$. The direction of current $I_{AMLED}$ flow is indicated by the dashed arrows.

the SJ-layer has a length L along the x-axis. Optimal RESURF is obtained when the charge in the p-type and n-type fingers is balanced (assuming uniform doping in the p-type and n-type fingers [10]:

$$q \cdot d_D \cdot N_D + (-q) \cdot d_A \cdot N_A = 0, \tag{4.1}$$

where $q$ is the elementary charge, $d$ is the finger width, $N$ is the doping concentration, and the subscripts A and D represent the acceptor and donor species respectively. To simplify the design procedure, we choose a symmetric SJ with $N_A$=$N_D$=$N$, and thereby equal finger widths $d_A$=$d_D$=$d$ to satisfy eq. (4.1). Moreover, a more uniform field-profile $F(x)$ is obtained when the fingers are fully depleted along the $y$-axis at a reverse bias $V < V_{BR}$. This ideally leads to a triangular fully depleted field profile $F(y)$. The fingers at the edges are terminated at a width of 0.5d, to ensure charge balance and symmetry. At full depletion, the following condition holds:

$$W_{dep} \approx \sqrt{\frac{4 \cdot \epsilon_{Si} \cdot V}{qN}} = d, \tag{4.2}$$

where $W_{dep}$ is the depletion width, and $\epsilon_{Si}$ is the silicon permittivity. Although Eq. (4.2) looks very simple, it is not straightforward to determine $N$, $d$, and the resulting $V_{BR}$ for full depletion. A rigorous 2-D model was derived earlier [20], where simple analytical relations were obtained to relate $N$, $d$ and $V_{BR}$ assuming that Eq. (4.2) is satisfied at $V = V_{BR}$. The relations are

$$L(\mu m) = 1.62 \times 10^{-5} V_{BR} (1.66d)^{\frac{1}{7}},$$
$$N(cm^{-3}) = 7.98 \times 10^{11} (1.66d)^{-\frac{8}{7}}, \quad (4.3)$$

which have been used as the design guideline for the SJ-LEDs in this chapter, where d is in μm.

Avalanche breakdown initiates via impact ionization, that generates electron-hole pairs. The electrons and holes are swept apart by the high reverse electric field and are accelerated to energies in excess of the band-gap. A certain fraction of these high energy electrons in the conduction band recombine with holes in the valence band leading to isotropic AM-EL [2, 3]. AM-EL occurs from a point (x,y) if $|F(x,y)|$ exceeds the critical field $F_{crit}$ as indicated by the regions $\Delta x_{rad}$ and $\Delta y_{rad}$ in Fig. 4.1.

### 4.2.2 Design

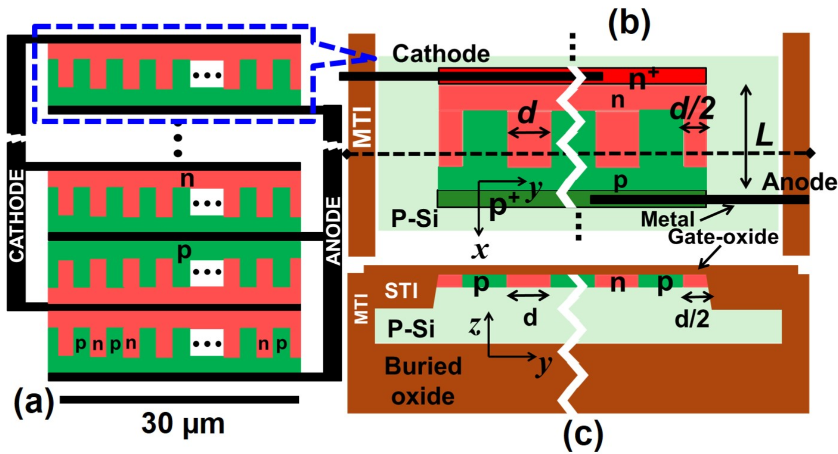


Figure 4.2: (a) Schematic top-view of the SJ-LEDs showing the location of the fingers and the electrodes. (b) Blow-up of the top-view of a single diode segment showing the symmetric p-n finger pairs terminating at a width of 0.5d on both ends of the y-axis, and (c) the vertical cross-section. The figures are not to scale.

Fig. 4.2 (a) shows the schematic top-view of the designed SJ-LEDs, (b) shows a blown-up schematic top view, and (c) shows the vertical cross-section of the SJ-LEDs, designed in a 140 nm silicon-on-insulator (SOI) CMOS technology [9]. The design consists of an array of identical diode segments. Each segment is made of symmetric p- and n-type doped layers with an implant dose of $5\times10^{12}$ cm$^{-2}$ that penetrate to a depth of ~0.25 μm into a 1.5 μm thick p-type (~ $10^{15}$ cm$^{-3}$) Si layer. This results in an effective doping N of ~ $2\times10^{17}$ cm$^{-3}$ in the p- and n-layers. The medium trench

Table 4.1: List of test-devices showing geometrical design parameters, breakdown voltages (defined at $I_{LED}$ = 1 μA) and variance across different (four) dies.

| **Device** | L **(μm)** | d **(μm)** | **Area:** A **(μm$^2$)** | $V_{BR}$ **(V): Measured (TCAD)** | **Die variance (%)** |
|---|---|---|---|---|---|
| D1 (pn) | 2 | – | 780 | 29.0 (30.1) | 3.6 |
| D2 (SJ-LED) | 2 | 0.384 | 780 | 50.0 (50.2) | 3.9 |
| D3 (pn) | 1 | – | 510 | 25.8 (26.0) | 2.2 |
| D4 (SJ-LED) | 1 | 0.384 | 510 | 28.4 (29.2) | 2.6 |
| D5 (SJ-LED) | 1 | 0.576 | 510 | 27.6 (28.0) | 4.8 |
| D6 (SJ-LED) | 1 | 0.768 | 510 | 26.6 (27.1) | 1.8 |

isolation (MTI) encloses the device, which along with the buried oxide (BOX) layer, provides galvanic isolation from neighboring devices. The $n^+$ and $p^+$ regions are a length L apart, and are also separated from the SJ region by an n and p layer respectively, in order to prevent the formation and premature breakdown of $n^+p$ or $p^+n$ junctions. In the SJ-LEDs named, D2, D4, D5 and D6, d and L have been varied as listed in Table 4.1. Lateral conventional p-n diodes D1 and D3 have been designed as reference devices having a single p-n junction along the x-axis for each diode segment (see Fig. 4.1(a)). The shallow p and n implants provide low attenuation for the vertically emerging light. Further, silicide protection masks were used on the entire active area except the electrodes to facilitate the off-chip vertical measurement of the EL-spectra via a spectrometer. Light can also be detected via an on-chip integrated photodiode (PD), which will be discussed in section 4.3.3.
It must be mentioned here that in this particular technology, the minimum value of d allowed by the design rule was 0.384 μm. From Eqs. (4.2) and (4.3), we can observe that the smaller the value of d for a given N, the lower is the value of V at which full depletion occurs. Thus, a stronger RESURF effect can be obtained in a more advanced CMOS technology which allows narrower mask spacing.

## 4.3 Analysis and Results

### 4.3.1 Electrical characteristics

Fig. 4.3 shows the TCAD [21] simulated 3-D profiles of the magnitude of the electric field in the designs, while Figs. 4.4, and 4.5 show the profiles along the x and y axis respectively. The peak field $F_m$ is at the junction in a

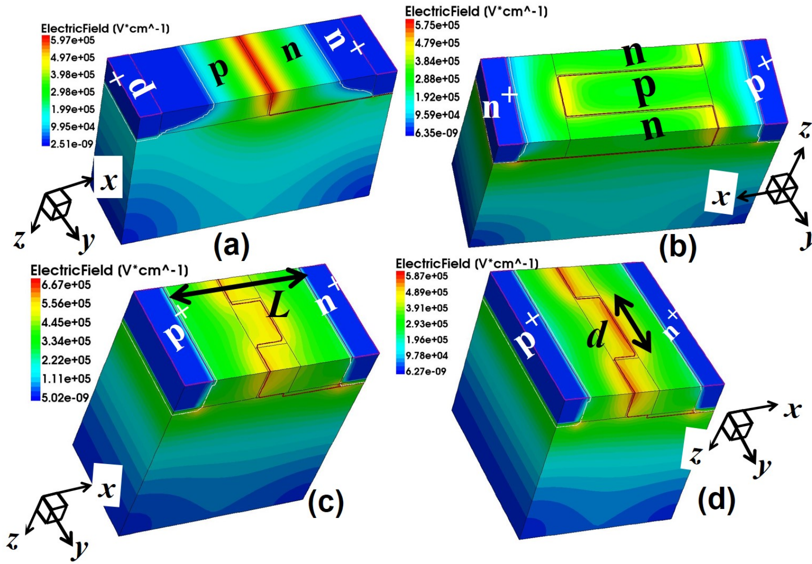


Figure 4.3: TCAD simulated field profiles $|F(x,y,z)|$ for (a) D1 at V = 35 V, showing a peak field at the junction (similar to D3 with L = 1 μm), (b) D2 at V = 52 V: SJ diode with L = 2 μm and d = 0.384 μm, showing RESURF, (c) D4 at V = 40 V with L = 1 μm and d = 0.384 μm, and (d) D6 at V = 35 V with L = 1 μm and d = 0.768 μm. Similar profiles have been obtained for D5 and D6, hence D5 is omitted for brevity. The coordinate axes are shown for each device separately for clarity. The BOX layer beneath the structures are omitted in the simulation.

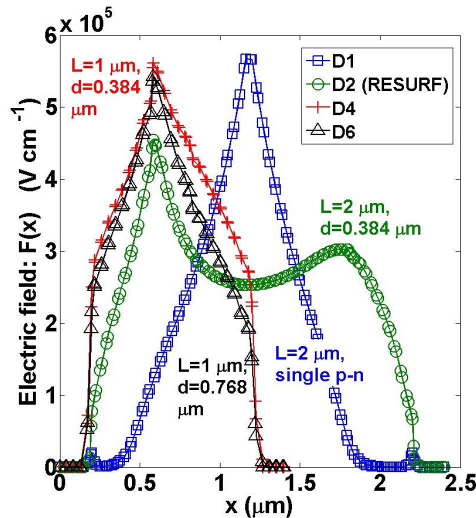


Figure 4.4: TCAD simulated profiles of the electric field magnitude along the $x$-axis $F(x)$ at V = 35 V for D1 (blue), showing a peak field at the junction, at V = 52 V for D2 (green), where full depletion is obtained. In D4 (red) and D6 (black), as $d$ reduces, $F(x)$ becomes more uniform. The $p^+$ edge is at $x = 0$.

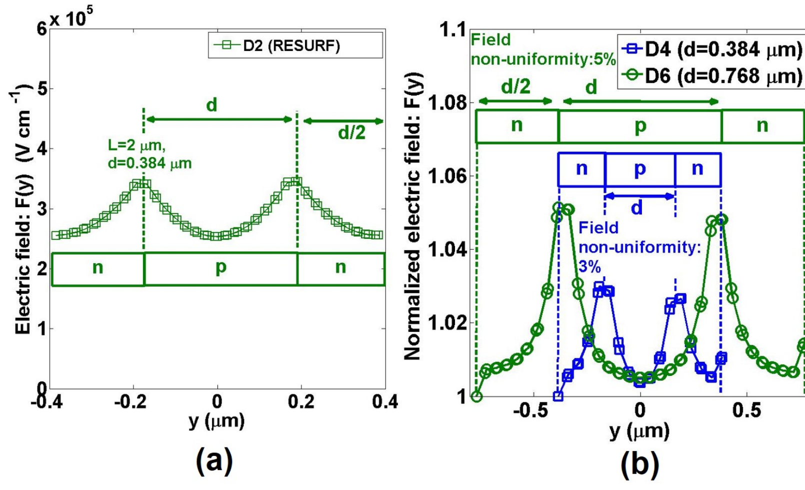


Figure 4.5: TCAD simulated profiles of the electric field magnitude along the y-axis $F(y)$ : (a) for D2 at V = 52 V, showing its hyperbolic shape and a uniform spread. Pinch-off of the depletion regions in the fingers (eq. (4.2)) occurs at $V < V_{BR}$; (b) for D4 at V = 40 V (blue), and at V = 35 V for D6 (green). Values are normalized w.r.t. the individual minimum $F(y)$ for comparison.

conventional p-n diode (Fig. 4.3 (a)), while in an SJ-diode, with suitably chosen $d$ and $L$ [20] (using Eqs. (4.2) and (4.3)), for a given V, the fingers deplete along $y$ faster than along $x$, leading to full depletion (Fig. 4.3 (b)), obtained for $L = 2$ μm and $d = 0.384$ μm. Charge balance results in field peaking at the opposite corners [20] of the p and n fingers. The spread in $F(x,y)$ expands the region where $F(x,y) > F_{crit}$, thereby expanding the EL-region. Full depletion along the $y$-axis also increases the spatial field-uniformity as shown in Fig. 4.5. Animated movies showing the evolution of the electric field profile in an SJ-diode can be viewed in the supplementary information section at the end of the chapter of the electronic version of this thesis. For a fixed $L$, as $d$ reduces, $F(y)$ becomes more uniform and spreads more as shown in Figs. 4.3 (c), (d), and 4.5. Full depletion of the fingers along the $y$-axis in D2 occurs at a bias $V \approx 5$ V when condition (4.2) is satisfied. This leads to a sharp drop in the capacitance C [22] as observed from the measured C-V characteristics in Fig. 4.6. Also C (V = 0) is about 2.5 times higher in D2 than in D1 owing to a higher number of junctions ($\approx$ 25) for the same device area $A$. The TCAD simulated 2-D field profiles for the SJ-LED D2 are shown in the insets at V = 2 V (partial depletion), and at V = 20 V (full depletion).

As reported in literature, RESURF also leads to a change in the $V_{BR}$ of the devices. Fig. 4.7 shows the TCAD simulated versus measured I-V characteristics of the reference lateral p-n LED D1 and SJ-LED D2 at an ambient temperature of 300 K. TCAD models include impact ionization

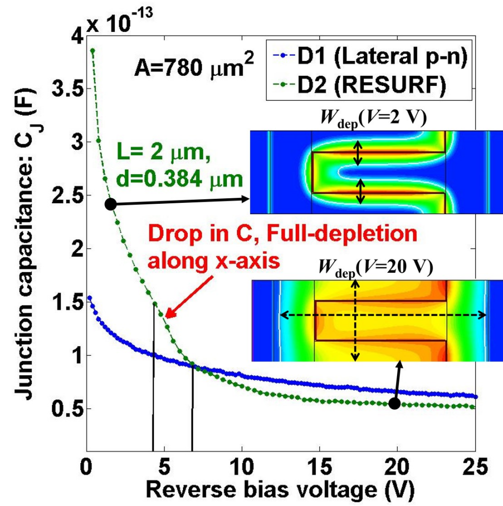


Figure 4.6: Measured reverse C-V characteristics of D1 (blue) and D2 (green). The insets show the TCAD simulated 2-D view of the field profile F(x,y) of D2 at V = 2 V (partial depletion) and V = 20 V (full depletion).

[23] along with doping dependent and field-enhanced SRH recombination [24]. A good agreement in the $V_{BR}$ is obtained, which has been defined [25] at I =1 μA, for both TCAD and experiment. With more RESURF in D2, $V_{BR}$ is higher than in D1, while both have the same doping levels and device area. A $V_{BR}$ of about 50 V is also in agreement with the 2-D analytical model in [20] with L = 2 μm and d = 0.384 μm. The reverse leakage current is higher in D1 than in D2 (with RESURF), which could be attributed to a lower effective carrier lifetime ($\tau_{eff}$ ~0.1 μs) in D1 than in D2 (~10 μs). This is possibly due to the different edge termination of the p-n junction in D1 (and also in D3), where the shallow trench isolation (STI) layer directly interfaces the junction along the x-axis leading to a higher chance of trap-assisted recombination.

Fig. 4.8 shows the measured and TCAD simulated DC I-V characteristics for the reference lateral p-n LED D3 and the SJ-LEDs D4 to D6, where also $\tau_{eff}$ of ~0.1 μs has been used. For a fixed L = 1 μm, as d reduces from 0.768 μm in D6 to 0.384 μm in D4, $V_{BR}$ increases by ~2 V. The (minor) discrepancies between the measured and TCAD simulated I-V characteristics may be caused by the non-uniformities at the oxide-silicon interface (see Fig. 4.2(c)), non-uniformities in the Si doping profiles, self-heating, defects in the depletion region, and/or series resistance effects, which were not included in TCAD. Further, D3 has a lower $V_{BR}$ than that of D1, although both of them are single p-n junctions with the same doping levels. This is due to the edge termination of the junctions with STI layers in both D1 (L = 2 μm) and D3 (L = 1 μm), as shown in Fig. 4.9 (a) and (b). This results in a non-zero field at the Si-$SiO_2$ interface as shown via the TCAD simulated F(x,y) in Fig. 4.9 (c), which in turn introduces an L-dependency

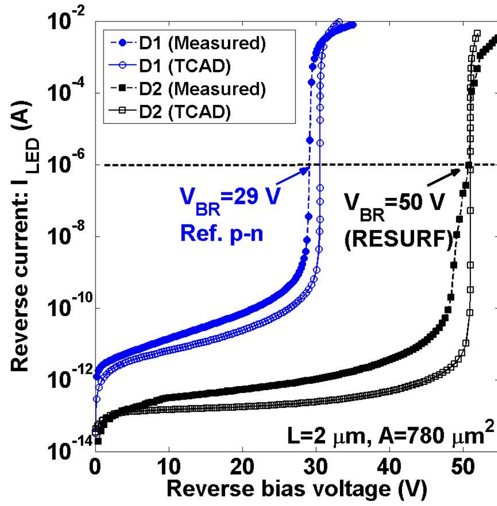


Figure 4.7: TCAD simulated and measured reverse I-V characteristics of D1 and SJ-LED D2 at 300 K. Measurements are done using a Keithley 4200 SCS. $V_{BR}$ has been defined [25] at I = 1 μA.

of the $V_{BR}$.

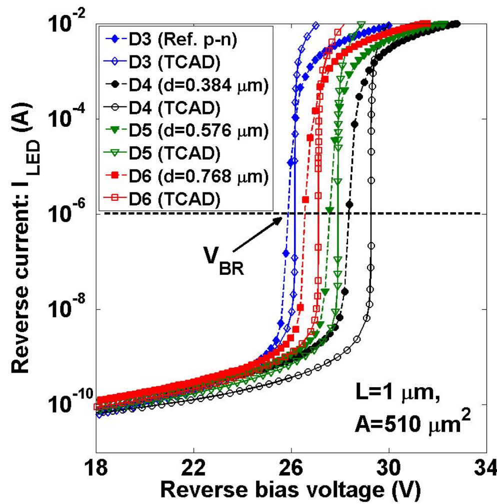


Figure 4.8: TCAD simulated and measured reverse I-V characteristics of the reference LED D3 and the SJ-LEDs D4, D5 and D6, all with L = 1 μm, at 300 K. Measurements are done using a Keithley 4200 SCS. $V_{BR}$ has been defined [25] at I = 1 μA.

Fig. 4.10 (a) summarizes the measured and TCAD simulated $V_{BR}$ for the SJ-LEDs. For d = 0.384 μm, as L is halved from 2 μm in D2 to 1 μm in D4, $V_{BR}$ also reduces nearly by a factor of 2. An increase in measured $V_{BR}$ is also observed as d reduces for a given L = 1 μm, as observed in

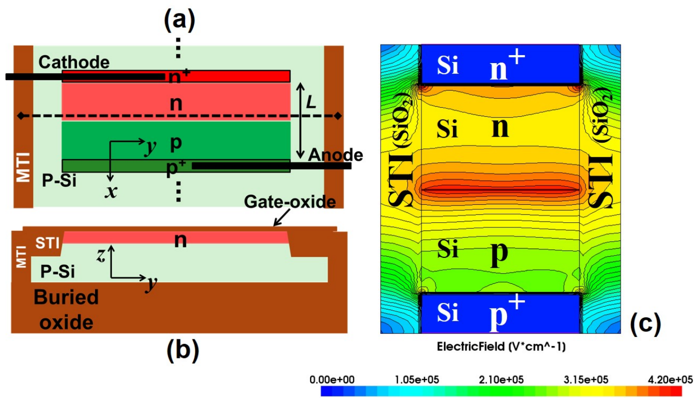


Figure 4.9: (a) Top-view of a single diode segment of the lateral symmetric p-n junctions D1 and D3, (b) the vertical cross-section, and (c) TCAD simulated 2-D profile of the magnitude of electric field $F(x,y)$ (top-view) for D3 at V = 33 V, showing the edge termination of the junction with STI layers with ideal Neumann boundary conditions.

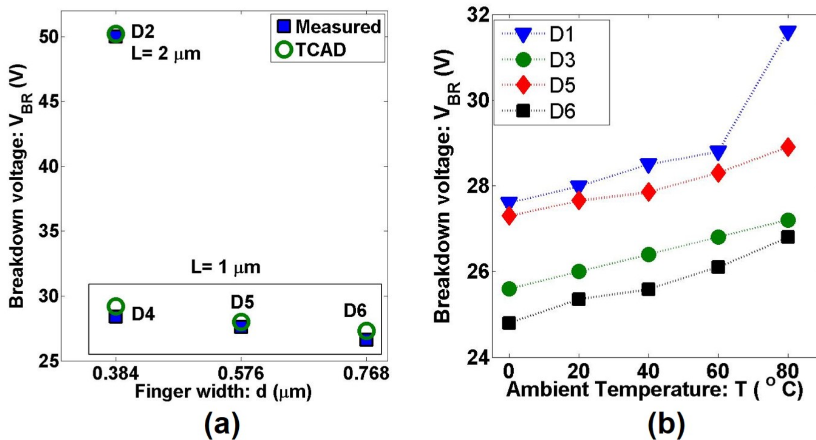


Figure 4.10: (a) TCAD simulated and measured $V_{BR}$ for the SJ-LEDs D2, D4, D5 and D6 at 300 K. (b) Measured $V_{BR}$ for the indicated LEDs at different ambient temperatures, showing a positive temperature coefficient.

diodes D4, D5 and D6, due to increasing field uniformity. This trend is also explained by the analytical model in [20]. Note that in all diodes, a positive temperature coefficient of the measured $V_{BR}$ was observed, which is consistent with avalanche breakdown [26]. The measured $V_{BR}$ at various temperatures for some of the LEDs are shown as examples in Fig. 4.10 (b).

### 4.3.2 Electroluminescent characteristics

The measured AM-EL spectra of D1 and D2 at 300 K for $I_{AMLED}$ = 4 mA and 8 mA are shown in Fig. 4.11(a). The light is coupled vertically from the

die into a multi-mode optical fiber with a diameter of ~ 50 μm feeding an ADC-1000-USB spectrometer from Avantes. Similar spectra for the LEDs D3, D4, and D6 are shown in Fig. 4.11(b). Emission is observed in the range 400 nm $< \lambda <$ 870 nm with a peak at $\lambda \approx$ 650 nm, where $\lambda$ is the free space photon wavelength. In order to compare the relative EL-intensity among the different LEDs, the optical fiber was kept at a fixed vertical position w.r.t. the die surface, while the lateral position of the LEDs was controlled by the $x$ and $y$ movement of the vacuum chuck that holds the die; until the active area of the LED is covered by the fiber tip. Ripples are observed in the spectra, in particular, in the range 600 nm $< \lambda <$ 800 nm. This is predominantly due to Fabry-Perot interference in the ~10 μm thick inter-metal dielectric (IMD) present on the top of the devices, which has been experimentally confirmed by measuring the transmission spectrum of the IMD (see Appendix B for further details).

In addition, one can observe in Fig. 4.11 that for a fixed $I_{AMLED}$, the increase in the spectral irradiance from D1 to D2 (both having $L$ = 2 μm) is dominant only for $\lambda \gtrapprox$ 620 nm, and negligible for $\lambda \lessapprox$ 600 nm. On the other hand the increase in spectral irradiance from D3 to D4 ($L$ = 1 μm) at a fixed $I_{AMLED}$ occurs more evenly at all values of $\lambda$. A possible hypothesis behind this observation can be made based on the extensive experimental findings and theoretical study of [27]. Indirect (phonon-assisted) recombination between high energy electrons and holes is the main mechanism for photon emission. High-energy transitions ($\lambda \lessapprox$ 620 nm) require a higher field with reduced impurity or phonon scattering within the EL-region as compared to the lower energy transitions ($\lambda \gtrapprox$ 620 nm). From Fig. 4.4, we observe firstly that for LEDs with $L$ = 2 μm, the reduction in the peak electric field (as one goes from D1 to D2) is more significant than for LEDs with $L$ = 1 μm (from D3 to D4). Secondly, the increase in spatial uniformity of $F(x,y)$ is more significant as one goes from D1 to D2, compared to when one goes from D3 to D4. Thus, electrons and holes traverse a longer distance in the EL-region for $L$ = 2 μm than in the case of $L$ = 1 μm, which increases the probability of phonon or impurity scattering in the former scenario. Both of these observations are likely to selectively increase the intensity of only lower energy transitions ($\lambda \gtrapprox$ 620 nm) when comparing D1 and D2; the intensity is enhanced from D3 to D4 more evenly for all $\lambda$.

Fig. 4.12 shows the relative comparison of the AM-EL intensity (i.e. optical power per unit device area) w.r.t. electrical power $P_{AMLED}$ for the SJ and reference AMLEDs, evaluated at a fixed $I_{AMLED}$ = 4 mA. For $L$ = 1 μm, as $d$ is progressively reduced from D6 to D5 and to D4, a nearly 50 % increase in the EL-intensity is obtained. This can be attributed to an increased spreading in $F(x,y)$. This also leads to an increase in $V_{BR}$ and thereby $P_{AMLED}$ (=$I_{AMLED} \cdot V_{BR}$). The increasing uniformity in $F(x,y)$ results in a greater fraction of $P_{AMLED}$ being utilized for AM-EL. Similar reasoning holds for $L$ = 2 μm. For the same $A$, the EL-intensity is observed

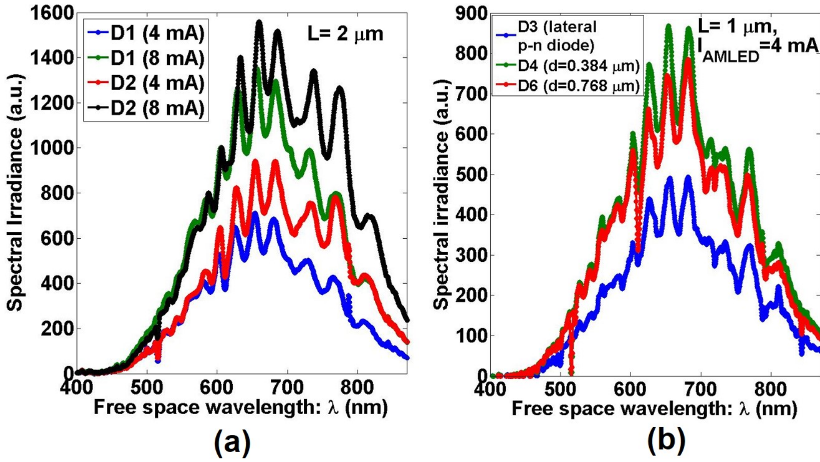


Figure 4.11: Measured AM-EL spectral irradiance at 300 K for (a) D1 and D2 at $I_{AMLED}$ = 4 mA and 8 mA, and (b) for D3, D4, and D6 at $I_{AMLED}$ = 4 mA. D5 is omitted for figure clarity. The spectra are measured vertically using a 50 μm multi-mode optical fiber feeding an ADC-1000-USB spectrometer from Avantes.

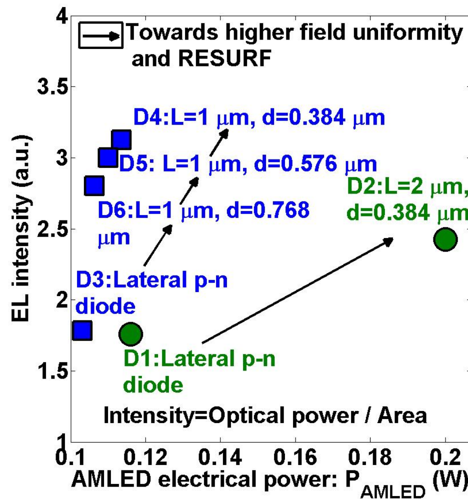


Figure 4.12: Relative comparison of AM EL-intensity w.r.t. electrical power $P_{AMLED}$ for the SJ and reference AMLEDs, at $I_{AMLED}$ = 4 mA. $P_{AMLED}$ scales proportionally with $V_{BR}$.

to be higher in D2 than in the reference lateral p-n LED D1, due to a higher field uniformity in D2. Further, the EL-intensity of D2 is less than that of D4, which can be explained by the lower value of $F_m$ [3] as seen from TCAD simulated field profile (see Fig. 4.4). The effect of a more uniform field profile on the optical intensity can be understood with the help of the 1-D opto-electronic model discussed in Chapter 3 (see Fig. 3.2), if we relate the

behavior of an SJ-LED to that of a p-i-n diode. If a p-n junction and a p-i-n diode have the same $V_{BR}$, this means that the area under the triangular field profile for the p-n junction is the same as that under the rectangular field profile for the p-i-n diode. But, the different spatial distribution of the field results in a different mean electron temperature in the two scenarios. Consequently, in a given device area, the optical power in a p-i-n diode (and therefore in our SJ-LEDs) is expected to be higher.





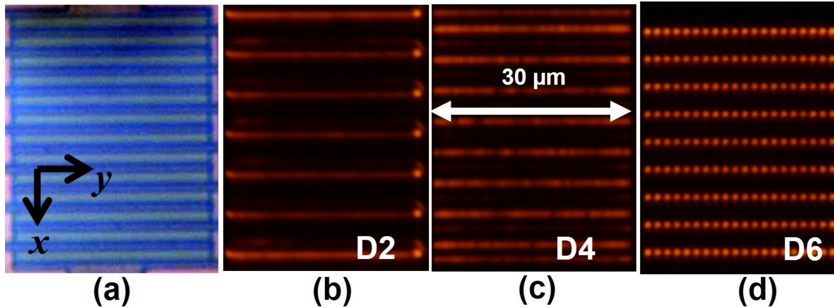


Figure 4.13: (a) Die micrograph of the SJ-LED D2 (as an example). AM-EL micrographs (to the same scale) at a fixed $I_{AMLED}$ = 4 mA at 300 K with a visible range camera and an integration time of 25 s are shown for (b) D2, (c) D4 and (d) D6. Light is received along the *z* axis (vertically). Note that the metal lines on the electrodes screen the light. The EL micrograph of D5 is similar to that of D6 and hence omitted for brevity.

The connection between the spatial uniformity in $F(x,y)$ and AM-EL is further evident from Figs. 4.13 (b), (c) and (d). In D4 (and also in D2), RESURF leads to a more uniform light emission along the $y$-axis. The increase in the EL-area is likely caused by the increasing field-uniformity. As such, a greater fraction of $P_{AMLED}$ is utilized for AM-EL, thereby yielding a higher power conversion efficiency for the SJ-LED. In D6, $F(y)$ is less uniform than in D4 (see also Fig. 4.5(b)). Under a given optical resolution, the non-uniformity in field results in a discontinuous array of EL-spots in D6. Each spot corresponds to a junction between a p-type and n-type finger.

### 4.3.3 Implementation in an integrated lateral optical link

Since AM-EL is isotropic, photons can be detected laterally by an integrated PD (with a geometry-limited extraction efficiency $\eta$), which is a standard vertical $n^+p$ junction separated from the AMLED by 20 µm along the $y$-axis via a shallow trench isolation (STI) layer as shown in Fig. 4.14(a). Self-heating in the LEDs is reduced significantly due to the presence of the handle wafer contact that serves as a heat sink [28]. The STI layer along with the IMD stack provides a low-attenuation optical path [29, 30], as will

be treated in detail in Chapters 5 and 6.

A quantitative measure of the EL-intensity ($I_{opt}$) of an AMLED in the lateral direction (y-axis) is obtained from the measured short-circuit current $I_{SC}$ and open-circuit voltage $V_{OC}$ of the PD at various $I_{AMLED}$. Both $I_{SC}$ and $V_{OC}$ increase with increasing $I_{AMLED}$ and hence, increasing $I_{opt}$, as shown in Fig. 4.14(b). The maximum photovoltaic power delivered to a load is given by $I_{SC} \cdot V_{OC}$ [19]. Considering the high detection IQE of an Si PD for visible-range photons, $I_{SC} \cdot V_{OC}$ is a lower bound estimate for the optical power $P_{opt}$ intercepted by the PD. Therefore, $I_{opt}$ of the LED along the y-axis is $\approx [I_{SC} \cdot V_{OC}] / [A_{SW} \cdot \eta]$, where $A_{SW}$ is the sidewall area of the EL-region of the AMLED normal to the optical propagation (y-axis).



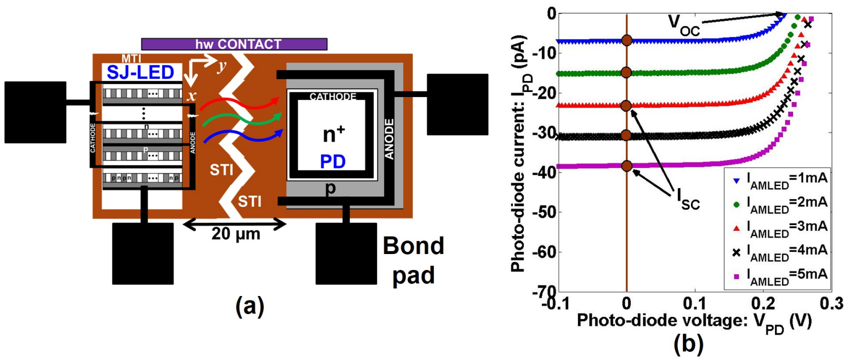


Figure 4.14: (a) Schematic top-view of the test optical link used in the measurement. The active areas of D4 and the PD are separated by 20 µm. (b) Measured I-V characteristics of the on-chip PD consisting of a vertical abrupt $n^+p$ junction when illuminated with the avalanche-mode SJ-LED D4 at various $I_{AMLED}$.

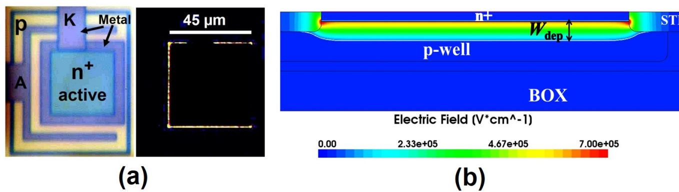


Figure 4.15: (a) Top-view (left) and the AM-EL micrograph (right) of the conventional $n^+p$ AMLED at $I_{AMLED} = 4$ mA. (b) TCAD simulated electric field profile beyond breakdown at $V_{AMLED} \approx 18$ V. The field and hence EL dominated over the perimeter of the $n^+$ active area.

Now we can compare $I_{opt}$ of our brightest SJ-LED D4 with a conventional $n^+p$ AMLED in the same technology. The die micrograph and the EL-micrograph of the conventional AMLED are shown in Fig. 4.15(a), where we observe that photon emission dominates only at the periphery of

the $n^+$ active area, which is close to the anode ($p^+$) contact. This is because of two reasons: electric field enhancement along the $n^+$ periphery (see Fig. 4.15(b)) and current crowding, which were verified by TCAD simulations.

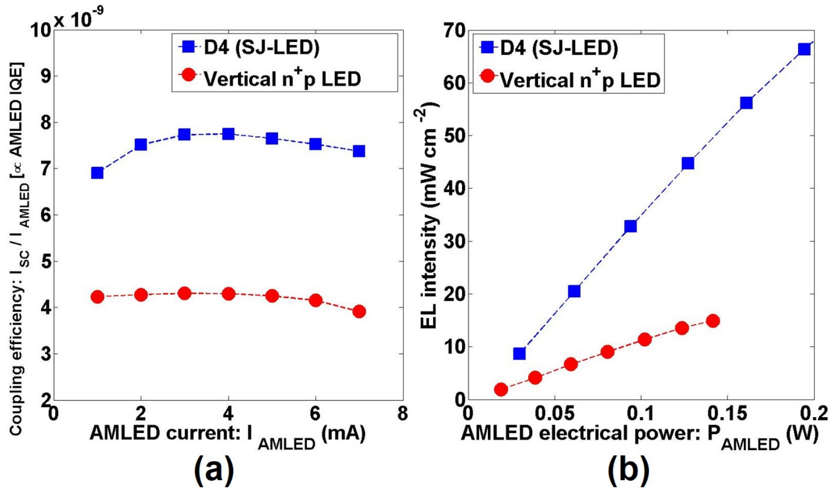


Figure 4.16: Comparison between (a) the internal quantum efficiency (IQE) of the SJ-LED D4 (blue) and a conventional $n^+p$ AMLED (red) in the same technology with a $V_{BR}$ of 16.8 V; (b) the AM-EL intensity along y-axis of the SJ-LED D4 (blue) and the conventional $n^+p$ AMLED (red) versus $P_{AMLED}$.

Fig. 4.16(a) shows the measured coupling efficiency [29, 30] defined as $I_{SC}/I_{AMLED}$ when the PD is illuminated by the SJ-LED D4 and the conventional $n^+p$ AMLED in the same technology with a $V_{BR}$ of 16.8 V. Since $I_{SC}$ is proportional to the EL-intensity, therefore the IQE of each LED [31] is proportional to the ratio $I_{SC}/I_{AMLED}$. At $I_{AMLED}$ = 4 mA, a 2 times higher IQE is obtained from the SJ-LED D4 (with an active device area A = 510 $\mu m^2$) as compared to the conventional AMLED (with a ~ 4 times larger active device area than D4). Note that the same PD separated by the same distance from the LED is used to detect photons from both the LEDs. The IQE of both the LEDs reaches its respective maximum in the range of $I_{AMLED}$ ~3 - 4 mA, which represents the regime of maximum efficiency of avalanche-mode radiative recombination in the SJ-LED D4 with an effective current density of ~ 800 A cm$^{-2}$. For a higher $I_{AMLED}$, a slight reduction in the IQE is observed, which could be caused by series resistance, or an increase in the non-radiative Auger recombination [31].

Fig. 4.16(b) compares the AM-EL intensity along the y-axis of the SJ-LED D4 with that of the conventional $n^+p$ AMLED versus $P_{AMLED}$. For the same $P_{AMLED}$, the EL-intensity of D4 is ~ 3 times higher than that of the conventional AMLED. This is the result of enhancement of the AM-EL region that is linked to the field-profile over the device area and the different $V_{BR}$ of the two LEDs.

The estimation of lateral intensity using an on-chip PD forms the basis of

realizing a monolithic optical link, which will be discussed in more detail in the next chapter.

## 4.4 Conclusions

Avalanche-mode (AM) superjunction (SJ) light-emitting diodes (LEDs) employing the reduced surface field (RESURF) effect have been presented. The devices have been optimized for a higher uniformity in the electric field profile that increases their internal quantum efficiency (IQE). The main take-away messages from this chapter are: 1) RESURF is obtained in a standard SOI technology, where $V_{BR}$ can be tuned by the designer via device scaling; 2) a more uniform electric field-profile directly translates into more uniform AM-EL over the device area ($A$); 3) the EL-intensity (optical power per unit area) increases for a more uniform field distribution; 4) a higher IQE and a higher EL-intensity can be achieved with the SJ-LED for the same electrical power ($P_{AMLED}$) as compared to a conventional AMLED.

## Supplementary Information: TCAD field profile versus increasing reverse bias (Movie)

# BIBLIOGRAPHY


[1] S. Dutta, P.G. Steeneken, V. Agarwal, J. Schmitz, A.J. Annema, and R.J.E. Hueting, "The avalanche-mode superjunction LED," IEEE Trans. Electron Devices, vol. 64, no. 4, pp. 1612-1618, 2017.

[2] A.G. Chynoweth and K.G. McKay, "Photon emission from Avalanche Breakdown in Silicon," Phys. Rev., vol. 102, no. 2, pp. 369-376, 1956.

[3] S. Dutta, R.J.E. Hueting, A.J. Annema, L. Qi, L.K. Nanver and J. Schmitz, "Opto-electronic modeling of light emission from avalanche-mode silicon $p^+n$ junctions," J. Appl. Phys., 118, 114506, 2015.

[4] L.W. Snyman, M. du Plessis, and H. Aharoni, "Injection-Avalanche-Based $n^+pn$ Silicon Complementary Metal Oxide Semiconductor Light-Emitting Device (450 - 750 nm) with 2-Order-of-Magnitude Increase in Light Emission Intensity," Jpn. J. Appl. Phys., vol. 46, no. 4B, pp. 2474-2480, 2007.

[5] M.A. Green, J. Zhao, A. Wang, P.J. Reece and M. Gal, "Efficient silicon light-emitting diodes," Nature 412, pp. 805-808, 2001.

[6] M. Sergio and E. Charbon, "An intra-chip electro-optical channel based on CMOS single photon detectors," IEEE International Electron Devices Meeting Tech. Digest, Paper no. 822, 2005 (doi: 10.1109/IEDM.2005.1609481).

[7] L.W. Snyman, K. Xu, J-L. Polleux, K.A. Ogudo, and C. Viana, "Higher Intensity SiAvLEDs in an RF Bipolar Process Through Carrier Energy and Carrier Momentum Engineering," IEEE J. Quantum Electron., vol. 51, no. 7, Art. ID 3200110, 2015.

[8] K. Xu, "On the design and optimization of three-terminal light-emitting device in silicon CMOS technology," IEEE J. Sel. Topics Quantum Electron., vol. 20, no. 4, Art. ID 8201208, 2014.

[9] P. Wessels, M. Swanenberg, H. van Zwol, B. Krabbenborg, H. Boezen, M. Berkhout, and A. Grakist, "Advanced BCD technology for automotive, audio and power applications," Solid-State Electronics, vol. 51, pp. 195-211, 2007.

[10] J.A. Appels, and H.M.J. Vaes, "High Voltage thin layer devices (Resurf devices)," IEDM technical digest, vol. 25, no. 2, pp. 238-241, 1979.

[11] T. Fujihira, "Theory of Semiconductor Superjunction Devices," Jpn. J. Appl. Phys., vol. 36, no.10, part 1, pp. 6254-6262, 1997.

[12] F. Udrea, A. Popescu and W. Milne, "The 3D RESURF junction," in Proc. International Semiconductor Conference, vol. 1, pp. 141-144, 1998.

[13] A.W. Ludikhuize, "A Review of RESURF Technology," in Proc. 12th International Symposium on Power Semiconductor Devices, pp. 11-18, 2000.

[14] D.J. Coe, "High voltage semiconductor device," U.S. Patent 4 754 310 A, 1988.

[15] J. Tihanyi.Power mosfet. U.S. Patent 5 438 215, Aug. 1995.

[16] F. Udrea, A. Popescu, and W.I. Milne, "3D RESURF double-gate MOSFET: A revolutionary power device concept," Electron. Lett., vol. 34, no. 8, pp. 808-809, 1998.

[17] L.Lorenz, G. Deboy, A. Knapp, and M. Marz, "COOLMOS$^{TM}$–a new milestone in high voltage Power MOS," in Proc. 11th International Symposium on Power Semiconductor Devices, pp. 3-10, 1999.

[18] M-J. Lin, T-H. Lee, F-L. Chang, C-W. Liaw and H-C. Cheng, "Lateral Superjunction Reduced Surface Field Structure for the Optimization of Breakdown and Conduction Characterisitcs in a High-Voltage Lateral Double Diffused Metal Oxide Field Effect Transistor," Jpn. J. Appl. Phys., vol. 42, pp. 7227-7231, 2003.

[19] S.M. Sze and K.K. Ng, "*Physics of Semiconductor Devices*," 3rd edition, John Wiley & Sons, Inc., USA, 2007.

[20] A.G.M. Strollo, and E. Napoli, "Power superjunction devices: an analytical model for breakdown voltage," Microelectron. J., vol. 32, no. 5-6, pp. 491-496, 2001.

[21] "Sentaurus TCAD," version L-2016.03, Synopsys Inc.

[22] M. Bobde, L. Guan, A. Bhalla, F. Wang and M. Ho, "Analyzing Superjunction C-V to Estimate Charge Imbalance," in Proc. 22nd International Symposium on Power Semiconductor Devices, pp. 321-324, 2010.

[23] R. van Overstraeten and H. de Man, "Measurement of the Ionization Rates in Diffused Silicon p-n Junctions," Solid-State Electronics, vol. 13, no. 1, pp. 583-608, 1970.

[24] A. Schenk, "A Model for the Field and Temperature Dependence of Shockley-Read-Hall Lifetimes in Silicon," Solid-State Electronics, vol. 35, no. 11, pp. 1585-1596, 1992.

[25] Robert F. Pierret, "Semiconductor Device Fundamentals," Addison-Wesley Publ., 1996.

[26] R. Hall, "Temperature Coefficient of the Breakdown Voltage of Silicon p-n Junctions," International Journal of Electronics, vol. 22, no. 6, pp. 513-519, 1967.

[27] L.W. Snyman, J-L Polleux, and K. Xu, "Stimulation of 450, 650 and 850 nm optical emissions from custom designed silicon LED devices by utilizing carrier energy and carrier momentum engineering," Proc. SPIE, vol. 10036, 1003603, 2017.

[28] L. Yan, G. Koops, P. Steeneken, A. Heringa, R. Surdeanu, L. van Dijk, "Integrated heat sinks for SOI power devices," in Proc. 25th International Symposium on Power Semiconductor Devices, pp. 285-288, 2013 (doi: 10.1109/ISPSD.2013.6694465).

[29] S. Dutta, R.J.E. Hueting, V. Agarwal and A.J. Annema, "An integrated optical link in 140 nm SOI technology," Proc. Conference on Lasers and Electro-Optics, Session JW2A, no. 132, 2016.

[30] S. Dutta, V. Agarwal, R.J.E. Hueting, J. Schmitz, and A.J. Annema, "Monolithic optical link in silicon-on-insulator CMOS technology," Optics Express, vol. 25, no. 5, pp. 5440-5456, Mar. 2017.

[31] E.F. Schubert, "*Light Emitting Diodes*," Cambridge University Press, 2006.

# CHAPTER 5

# MONOLITHIC OPTICAL LINK IN SOI-CMOS TECHNOLOGY

**Abstract**

This chapter presents a monolithic laterally-coupled wide-spectrum (350 nm < $\lambda$ < 1270 nm) optical link in a silicon-on-insulator CMOS technology. The link consists of a silicon (Si) light-emitting diode (LED) as the optical source and a Si photodiode (PD) as the detector; both realized by vertical abrupt $n^+p$ junctions, separated by a shallow trench isolation consisting of silicon dioxide. Medium trench isolation around the devices along with the buried oxide layer provides galvanic isolation. Optical coupling in both avalanche-mode and forward-mode operation of the LED are analyzed for various designs and bias conditions. From both DC and pulsed transient measurements, it is further shown that heating in the avalanche-mode LED leads to a slow thermal coupling to the PD with time constants in the ms range. An integrated heat sink in the same technology leads to a ~ 6 times reduction in the change in PD junction temperature per unit electrical power dissipated in the avalanche-mode LED. The analysis paves the way for wide-spectrum optical links integrated in smart power technologies.

*"It is wrong to think that the task of physics is to find out how Nature is. Physics concerns what we say about Nature."* (Niels Bohr)

---

This chapter is an extension of a publication in Optics Express [1]. A part of the results was also presented in the proceedings of Conference on Lasers and Electro Optics 2016 [2].

## 5.1 Introduction

In the previous chapters, we have discussed how silicon (Si) based avalanche-mode light-emitting diodes (AMLEDs) can emit photons in avalanche breakdown that encompass a broad range of wavelengths (peaking in the visible range). The light emitted by an Si AMLED appears to be greenish-white to the naked eye. This is in contrast with photon-emission from conventional forward-biased Si diodes, which leads to infra-red electroluminescence (EL). In either scenario, photon emission carries "information" of an "event" where radiative recombination took place. It is interesting to investigate how and to what degree of efficiency these photons can be detected at some distance to read "information". This brings in the concept of an optical link. In chapter 4, we already introduced this feature without going into much detail, for estimating the lateral intensity of an AMLED quantitatively. In this chapter, the design and physical behavior of such an optical link will be discussed in depth from a device-physics point of view.

Monolithically integrated optical links cater to high speed transceiver [3] applications, and to smart-power applications where data needs to be transferred between galvanically isolated voltage domains [4, 5]. The viability of an integrated optical link in Si demands a high coupling efficiency (that encompasses the combined efficiencies of the light-emitter, waveguide and the detector) in conjunction with proper galvanic isolation and sufficiently high data rates.

Operating an Si LED in forward mode (FM) yields infrared (IR) EL ($\lambda \sim$ 1000-1270 nm) [6–9]. This emission spectrum has a small overlap with the spectral responsivity of Si photodiodes (PDs) [10] resulting in a low internal quantum efficiency (IQE) of the PD. Modulation speeds up to ~ 1 MHz have been reported for Si FMLEDs [11].

Operating an Si AMLED yields broad-spectrum EL ($\lambda \sim$ 350-900 nm) [12–15] with a reported IQE of $\sim 10^{-5}$ [14]. This EL spectrum has a significant overlap with the spectral responsivity of Si (PDs) [10] resulting in a high IQE of the PD. Optical modulation speeds as high as a few tens of GHz have been reported in Si AMLEDs [16].

Galvanic isolation can be obtained using silicon-on-insulator (SOI) technology. Prior art reported FM optocoupling [17] and AM optocoupling in a 0.8 μm [18], 0.35 μm [19, 20], 2 μm [21] and 3 μm [22] bulk CMOS technology with limited galvanic isolation. High isolation voltages (~ 3 kV) have been reported [23], however in an organic opto-coupler which is not compatible with standard CMOS technology, and a maximum on-off keying speed of only 70 kHz was reached. SOI technology also offers monolithic waveguiding, which has shown potential applications in high-level hybrid

integration for cost-effective high-performance computing [24, 25]. Significant advances have been made to integrate optical data communication in the past, but most of them utilized hybrid solutions for inter-chip data transfer [3, 25].

In this chapter:

1. A fully integrated wide-spectrum (350 nm $< \lambda <$ 1270 nm) optical link in a commercial 0.14 µm SOI-CMOS technology [26] is demonstrated, which provides ~ 100 V galvanic isolation. The link has three components: The light-emitter, the optical channel (waveguide) and the detector. The LED and the PD are implemented as vertical $n^+p$ junctions in Si.
2. Opto-coupling is shown with the LED biased both in FM and in AM, the two yielding considerably different link properties with respect to link efficiencies in DC operation, parasitic thermal coupling effects and scaling properties.
3. The focus is on integrated optical interconnects for smart power applications (e.g. level shifters) which requires highly sensitive photodetectors (e.g. SPADs [27, 28]) given the inherently low light intensity emitted by the LEDs. However, to demonstrate and benchmark our design, we use regular PDs.

The rest of the chapter is outlined as follows. Section 5.2 presents the design and layout of the optical link. Here the main parameters that contribute to the overall link efficiency are defined. Section 5.3 describes the DC electrical and EL properties of the LED. Section 5.4 describes the spectral responsivity of the PD and its I-V characteristics. Sections 5.5 and 5.6 demonstrate optical coupling in DC operation of FM and AM operation of the LED. Section 5.7 addresses the heating in the AMLED, and thermal coupling to the PD. Section 5.8 presents a comparison between FM and AM operation of our optical link, followed by design recommendations for further improvement of the coupling quantum efficiency. Finally, section 6.5 concludes this chapter.

## 5.2 Architecture and layout

Fig. 5.1(a) shows a schematic top-view of the optical link consisting of the LED, the dielectric channel (as a waveguide) and the PD. We use the ratio of the LED current $I_{LED}$ to the short-circuit current ($I_{SC}$) of the PD [29] (the latter defined as photo-generated current at zero bias voltage) as a measure for the lateral optical coupling. We introduce the coupling quantum efficiency $\eta$ as a figure-of-merit (FOM) of our designs, defined as:

$$\eta(\lambda, D) = \frac{I_{SC}}{I_{LED}} = \eta_{LED}(\lambda) \cdot \eta_{WG}(\lambda, D) \cdot \eta_{PD}(\lambda), \quad (5.1)$$

where $\eta_{LED}$ and $\eta_{PD}$ represent the IQE of the LED and the PD respectively. $\eta_{WG}$ is a lumped representation of the overall efficiency of the waveguide (WG) which depends on the mode of LED operation (and hence on $\lambda$), and on the link length D. $\eta_{WG}$ can be expressed as the product of various components: $\eta_{WG}(\lambda,D) = \eta_{in}(\lambda) \cdot T_{Fresnel}(\lambda) \cdot \eta_{prop}(\lambda,D) \cdot \eta_{out}(\lambda)$. Here, $\eta_{in}$ and $\eta_{out}$ are the efficiencies of optical transmission from the LED to the WG, and that from the WG to the PD respectively. $T_{Fresnel}$ represents the effective transmission efficiency due to Fresnel reflections [30] at the Si-WG interfaces. Note that the values of $\eta_{in}$, $\eta_{out}$ and $T_{Fresnel}$ are independent of D, and specific to our design (geometry, refractive indices, angle of incidence etc.) and to the mode of LED operation, and these parameters will be addressed in the next chapter. $\eta_{prop}$ is the D-dependent propagation efficiency and takes into account the absorption losses in the WG and the effective angular aperture of the PD along the direction of propagation. $\eta_{prop}$ will be further discussed in sections 5.5 and 5.6.

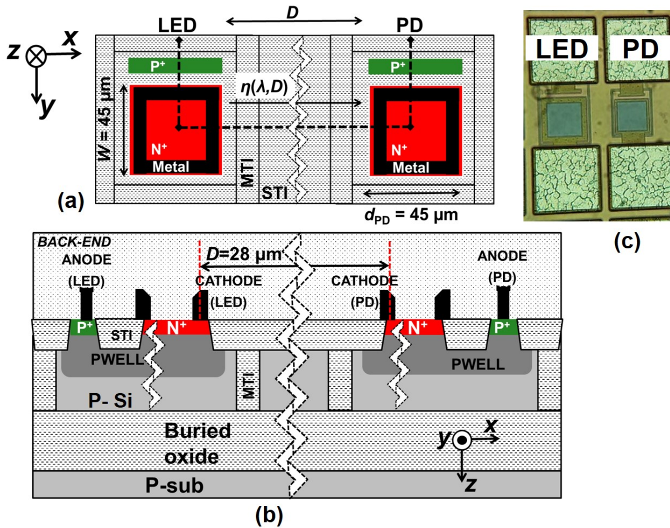


Figure 5.1: (a) Schematic layout of the optical link. (b) Schematic vertical cross section of the default design of the link along the indicated dashed line in the layout. (c) Die micrograph (top-view) of the default design of the optical link. Figures (a) and (b) are not to scale.

The optical link in context involves relatively low values of $\eta$ (primarily due to a low IQE obtained from the Si LED), thereby demanding high electrical power, in particular during AM operation of the LED. This leads to a significant electrical power dissipation, and thereby heating in the AMLED.

Fig. 5.1(b) shows the schematic vertical cross section of the default design of the optical link along the dashed line in Fig. 5.1(b). Fig. 5.1(c) shows the die-micrograph. The LED and the PD consist of vertical abrupt $n^+p$ junctions enclosed by medium trench isolation (MTI) for galvanic

isolation (of ~ 100 V) down to the buried oxide (BOX) layer. The substrate is lowly p-doped Si. A vertical window is opened in the cathode ($n^+$) contact and silicidation is suppressed in the active areas (except at the contacts) to enable vertical measurement of the EL-spectra through an optical fiber. The LED and PD are separated using STI (composed of $SiO_2$). In addition, a variation of the link has been designed by placing a heat sink to its vicinity. This heat sink is a handle wafer contact [31], which is a vertical polysilicon column extending from the active SOI layer down to the handle wafer. In this design, D is varied from 10 μm to 60 μm in steps of 10 μm.

## 5.3 LED: electrical and optical behavior

The optical link is operated with the Si LED either in FM or AM. Figure 5.2 shows the I-V characteristics of the LED on a semi-log scale, measured at an ambient temperature $T_0$=300 K. An almost unity ideality factor is obtained for forward bias voltages $< 0.8$ V, while the series resistance becomes prominent at a higher bias. In reverse bias, the current rises sharply near the avalanche breakdown voltage ($V_{BR}$). Using the definition of breakdown at an arbitrarily chosen current [32] I=1 μA, we find $V_{BR}$ = 16.8 V.

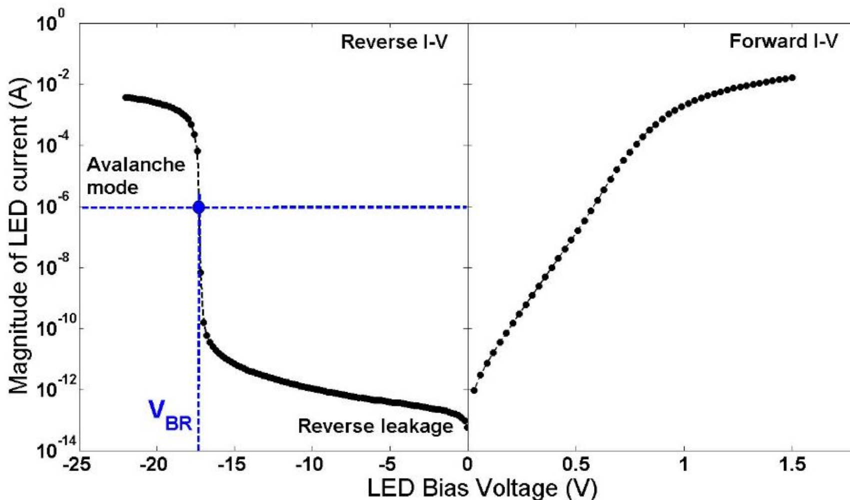


Figure 5.2: Measured I-V characteristics of the LED at $T_0$ = 300 K in reverse and forward bias on a semi-log scale. Measurements are done using a Keithley 4200 Semiconductor Characterization System (SCS).

The EL micrographs in AM and FM LED operation are depicted in Figs. 5.3(a) and 5.3(b), respectively. In particular for the AMLED, the emission is prominent only along the $n^+$ edge closest to the $p^+$ contact due to current crowding and field enhancement (as was discussed in Chapter 4). In Fig. 5.3(b), we see the IR light emission extending well outside

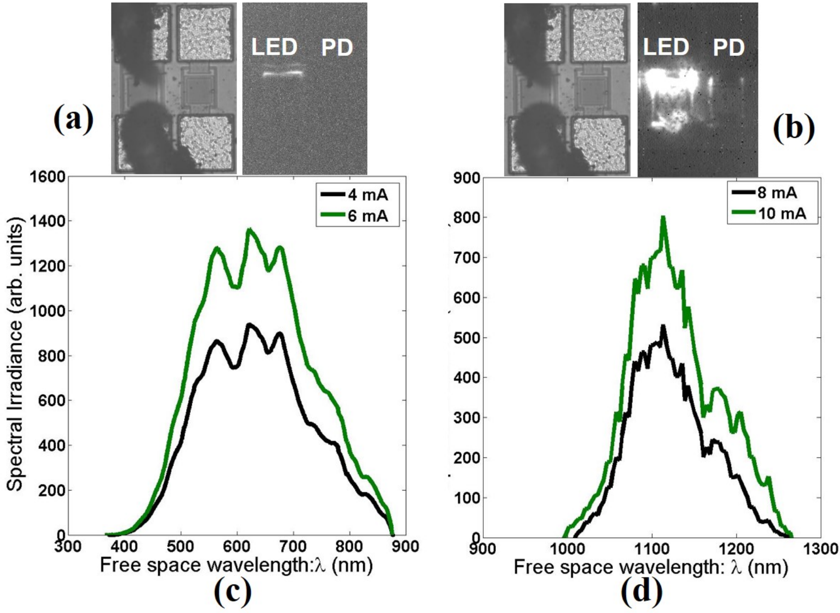


Figure 5.3: Magnified die top-view along with the corresponding EL-micrographs for (a) the AMLED captured with a XEVA-257 camera and (b) for the FMLED captured vertically (out of plane) with a XEVA-320 InGaAs camera from Xenics. (c) EL-spectra of the LED at various current levels at $T_0$ = 300 K for avalanche mode and (d) forward mode operation, measured vertically by a 50 μm multi-mode optical fiber feeding an ADC-1000-USB spectrometer (for AM-EL) and an AvaSpec-NIR256-1.7 spectrometer (for FM-EL) from Avantes. The arbitrary unit scales in (c) and (d) are not related and cannot be used for comparison.

the diode's junction area, in line with the longer absorption length for IR light in Si. Figures 5.3(c) and 5.3(d) show the EL-spectra of the AMLED and the FMLED respectively at various current levels at $T_0$=300 K. The FMLED emits in the IR (~1000-1270 nm) [6–9]. The AMLED exhibits broad-spectrum (~350-900 nm) EL, similar to the ones reported earlier [15, 33]. The optical intensity increases linearly with increasing $I_{FMLED}$ or $I_{AMLED}$.

## 5.4 PD: photovoltaic behavior

The PD current ($I_{PD}$) is sensitive to both EL-intensity L (that depends on λ), and the junction temperature $T_j$ [29]. It is the sum of the regular junction current and the photo-generated current (equal to $I_{SC}$):

$$I_{PD} = I_0(T_j) \cdot \left[\exp\left(\frac{qV_{PD}}{k_B T_j}\right) - 1\right] - I_{SC}(L, \alpha_{Si}(\lambda, T_j)), \tag{5.2}$$

where $I_{SC}(L, \alpha_{Si}(\lambda, T_j)) = -I_{PD}$ at $V_{PD} = 0$, with the negative sign representing current flow from the cathode to the anode. $I_{SC}$ depends on L and

on the Si absorption coefficient $\alpha_{Si}(\lambda, T_j)$. Also, q is the elementary charge and $k_B$ is the Boltzmann constant, and $I_0$ is the dark current of the PD. Upon rearranging Eq. (5.2), the open-circuit voltage $V_{OC}$ can be expressed in terms of $I_{SC}$:

$$V_{OC}(L, T_j) = \left(\frac{k_B T_j}{q}\right) \cdot \ln\left[1 + \frac{I_{SC}(L, \alpha_{Si}(\lambda, T_j))}{I_0(T_j)}\right]. \quad (5.3)$$



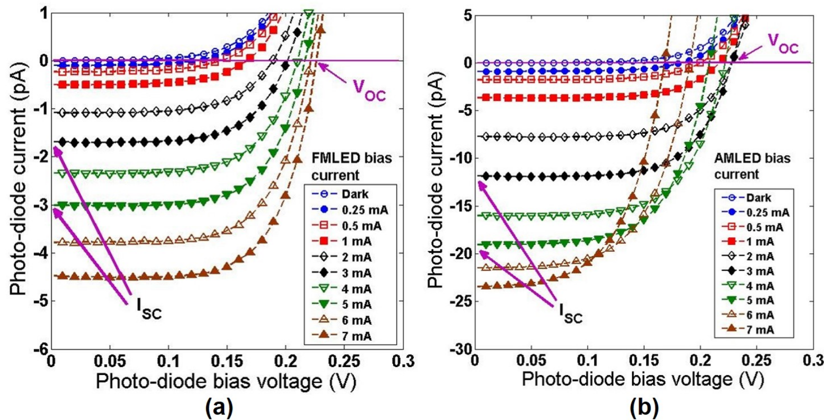


Figure 5.4: I-V characteristics of the PD under (a) FMLED operation for various $I_{FMLED}$, and (b) under AMLED operation for various $I_{AMLED}$ at $T_0$ = 300 K for the default design without heat sink. Measurements are done using a Keithley 4200 SCS.

An increase in only L at a fixed $T_j$ leads to an increase in both $I_{SC}$ and $V_{OC}$. This is valid in the case when the LED is in FM operation (ensuring that the electrical power is not very high), as shown in Fig. 5.4(a). An increase in only $T_j$ at a fixed L also results in an increase in the $I_{SC}$ since $\alpha_{Si}(\lambda, T_j)$ increases with temperature [34], but $V_{OC}$ decreases with increasing $T_j$. In AM operation of the LED, the higher electrical power leads to heating in the AMLED. This in turn leads to a rise $T_j$, not observed in FM operation. This is reflected from the I-V characteristics of the PD for various $I_{AMLED}$ in our default design (without heat sink) as shown in Fig. 5.4(b).

The PD $I_{SC}$ is strongly dependent on the spectral distribution of emission of the LED. Along the same lines of the "matching factor" as introduced in [35], this dependence can be expressed by an emission-specific responsivity S defined as:

$$S = \int E(\lambda) \cdot \frac{I_{SC}(\lambda)}{P_{opt}} d\lambda, \quad (5.4)$$

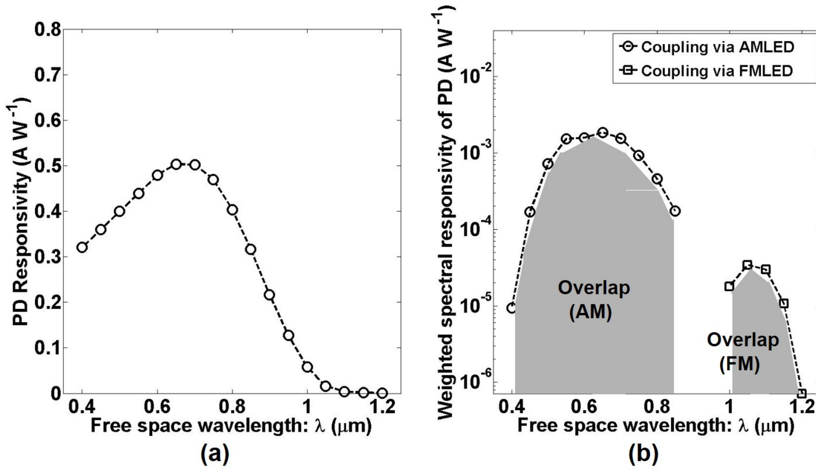


Figure 5.5: (a) TCAD simulated PD responsivity at $T_0$ = 300 K as a function of photon wavelength when the junction is illuminated by a monochromatic, unpolarized and unidirectional light source at a fixed optical power $P_{opt}$. (b) Calculated responsivity of the PD weighted by the normalized spectral irradiance of the LED in AM and FM. Note that heating effects are not included in this calculation.

where $E(\lambda)$ is the normalized spectral irradiance of the LED, such that $\int E(\lambda)\, d\lambda = 1$. $I_{SC}(\lambda)$ is the PD $I_{SC}$ when illuminated by a unidirectional monochromatic source having a fixed optical power $P_{opt}$. In Fig. 5.5(a) the TCAD simulated (in Sentaurus vL-2016.03) spectral responsivity of the PD, defined as $I_{SC}(\lambda)\ /\ P_{opt}$, is shown at $T_0$ = 300 K, excluding any heating effect. Default λ-dependent values of $\alpha_{Si}$ (= $4\pi k/\lambda$) at a fixed $T_0$ = 300 K were used in Sentaurus, with the extinction coefficient $k$ corresponding to the data of [36]. Fig. 5.5(b) plots the integrand in the right hand side of Eq. (5.4) as a function of λ. Here $E(\lambda)$ has been obtained from the measured EL spectra. The value of the emission specific responsivity S in AMLED operation is 100 times higher than in FMLED operation. This is expected due to a higher $\alpha_{Si}(\lambda, T_j)$ of the PD junction [34, 37, 38] for shorter λ. Note that the effect of the transmission efficiency of the optical waveguide between the LED and the PD are not (yet) included in this calculation. We will revisit this calculation once again in the next chapter, where the waveguide transmission efficiencies for isotropic and wide-spectrum emission will be dealt with in further detail using TCAD simulation.

Note that one can enhance the responsivity of the PD by applying a reverse bias. However, in such a case, $\Delta I_{PD}(V_{PD}) = I_{SC} \cdot M(V_{PD})$, with $V_{PD} < 0$. This introduces an unknown bias-dependent multiplication factor M [39]. Hence, to analyze the optical signal intercepted by the PD, we characterize the coupling quantum efficiency in our system by measuring only $I_{SC}$ to eliminate the unknown parameter M. Let us now describe the overall measured link efficiency η in the next two sections.

## 5.5 Coupling efficiency and waveguide in FM LED operation

In forward mode operation, the IQE of Si FMLEDs is reported to be $\sim 10^{-3}$ [6]. Fig. 5.6 shows the measured coupling quantum efficiency η versus $I_{FMLED}$ for different values of D at $T_0$ = 300 K. A gradual increase in η is observed with increasing $I_{FMLED}$. This trend indicates that the current is mainly diffusion-dominated [40], that Auger recombination in the LED is not significant, and that the non-radiative recombination process is mainly Shockley-Read-Hall [37], the rate of which decreases with increasing $I_{FMLED}$.

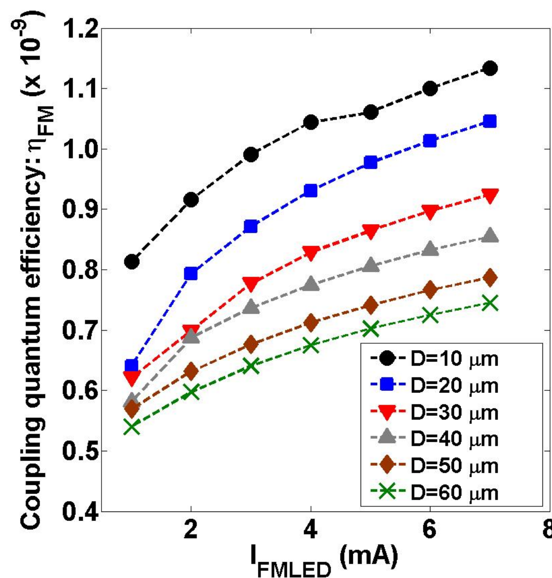


Figure 5.6: Measured $\eta_{FM}$ versus $I_{FMLED}$ for different values of D at $T_0$ = 300 K.

Fig. 5.7(a) shows the measured $I_{SC}$ of the PD versus D for three values of $I_{FMLED}$. $I_{SC}$ decreases monotonically with increasing D. The mean rate of attenuation $\gamma_{FM}$ is low: $\approx 0.072$ dB $\mu m^{-1}$. Pure isotropic transmission cannot explain this D-dependence because it would have resulted in a sharper attenuation ($\propto D^{-2}$), which is not observed. The trend can be explained by the formation of two lateral slab waveguides in our design as shown in Fig. 5.7(b). The back-end waveguide has a high refractive index $Si_3N_4$ core sandwiched between a lower and an upper $SiO_2$ cladding layer formed by the STI and the inter-metal dielectric respectively. These dielectrics have a low absorption in the entire spectral range of interest [41, 42]. The high refractive index SOI layer forms an additional waveguide with low absorption losses for photons with $\lambda > 1$ μm [34]. For simplicity, we assume that propagation occurs at near critical angles of incidence ($\theta_c$).

Hence, the effective index of the combined waveguide along the propagation direction (x-axis) is $n_{core} \cdot \sin\theta_C \approx n_{SiO2}$, where $n_{core}$ represents the refractive index of the nitride or the SOI core layer. Consequently, the observed D-dependence is captured in the propagation efficiency $\eta_{prop}$ and is primarily due to the reduction in the lateral aperture of the PD as derived using geometrical ray optics as follows.

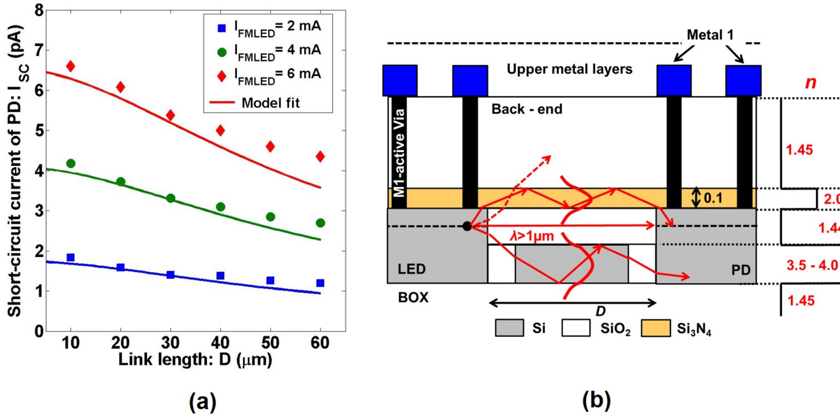


Figure 5.7: (a) Measured and modeled $I_{SC}$ of the PD versus D for three values of $I_{FMLED}$. $I_{SC}$ decreases with increasing D as the angular aperture of the PD reduces. (b) Simplified cross-section of the link showing the position of two possible waveguides in FM coupling and the refractive indices for each material. An exemplary ray diagram and a fundamental mode wavefront are shown in each waveguide for a point source of light at the LED junction.

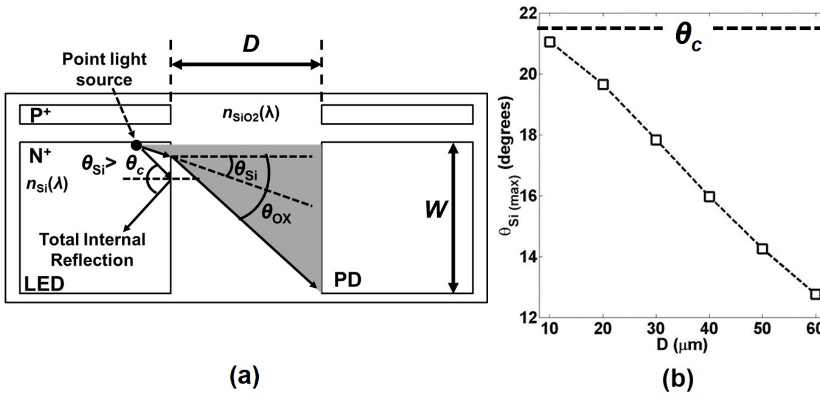


Figure 5.8: (a) Simplified 2-D ray diagram of the top-view of our design, with $W \approx 45$ μm. Photons that are incident below the critical angle $\theta_C$ can emerge into $SiO_2$ prior to being guided through the nitride or the SOI layer. (b) Calculated maximum angular aperture of the PD for increasing D.

Fig. 5.8(a) shows a simplified 2-D ray diagram of the top-view of our

design for a point source of light. According to Snell's law, the effective 2-D aperture $\theta_{Si(max)}$ of the PD can be defined as the largest angle of incidence at the Si-$SiO_2$ interface for which the emergent ray is intercepted by the PD active area:

$$\theta_{Si(max)}(D, W) = \sin^{-1}\left[\frac{n_{SiO2}}{n_{Si}\cdot\sqrt{1+\left(\frac{D}{W}\right)^2}}\right], \tag{5.5}$$

where $n_{SiO2}$ and $n_{Si}$ are the average refractive indices over the spectral range of $SiO_2$ and Si respectively. Note that $\theta_{Si(max)}$ has an upper bound of $\theta_C \approx 21^o$, which is the critical angle at the Si-$SiO_2$ interface. A TCAD based 2-D raytracing animation of the top-view can be found in the supplementary material section at the end of this chapter (only in the electronic version of the thesis) to illustrate the aperture given by Eq. (5.5), where $\theta_{Si}$ increases from zero to $\theta_{Si(max)}$ beyond which the ray is totally internally reflected back to the Si LED.

As D increases for a fixed $W$ (as in our experiment), $\theta_{Si(max)}$ decreases (as shown in Fig. 5.8(b)), leading to a proportional reduction in the optical coupling. In addition, the absorption losses in the core and cladding are also D-dependent [43]. We can model these combined effects using the following relation:

$$I_{SC}(D) = a \cdot \theta_{Si(max)} \cdot \exp(-b \cdot D), \tag{5.6}$$

where $a$ and $b$ are fit parameters obtained using the least squares method. A good agreement is obtained between the modeled and measured trends as shown in Fig. 5.7(a). The fit value of $a$ is proportional to $I_{SC}$(D = 10 μm). The fit value of $b \approx 10$ $cm^{-1}$ is in good agreement with the reported [34] $\alpha_{Si}$(λ = 1.1 μm). This indicates that the SOI waveguide is dominant in FM coupling.

## 5.6 Coupling efficiency and waveguide in AM LED operation

The avalanche mode EL spectrum of the LED peaks in the visible range as shown in Fig. 5.3(a). The IQE of Si AMLEDs is reported to be ~ $10^{-5}$ [14]. Fig. 5.9 shows the measured $\eta$ versus $I_{AMLED}$ for different values of D. Note that a heat sink is present in these designs. The dependency of $\eta$ on $I_{AMLED}$ reflects the efficiency of radiative recombination in the AMLED, which is sensitive to the current level. We observe a weakly increasing $\eta$ with increasing $I_{AMLED}$, indicating that the injection level is moderate enough not to cause a droop in the radiative efficiency owing to Auger recombination [37]. Further, $\eta$ is observed to be relatively less sensitive to $I_{AMLED}$ as compared to the situation in forward mode. This is because

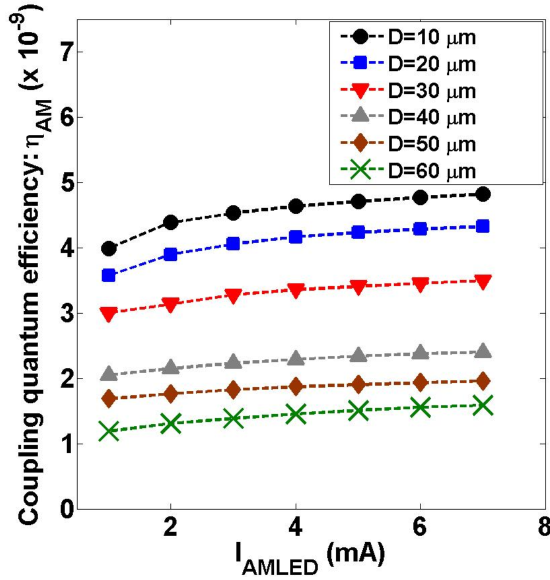


Figure 5.9: Measured $\eta_{AM}$ versus $I_{AMLED}$ for different values of D at $T_0$ = 300 K. A heat sink is present in these designs.

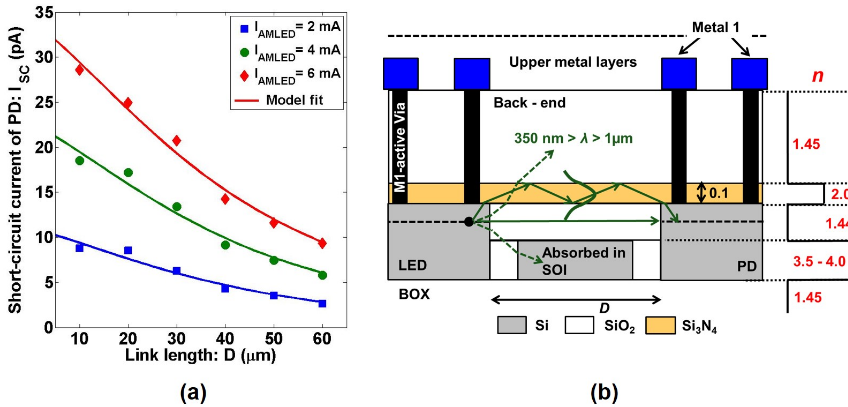


Figure 5.10: (a) Measured and modeled $I_{SC}$ of the PD versus D for three values of $I_{AMLED}$. $I_{SC}$ decreases with increasing D as the angular aperture of the PD reduces. (b) Simplified cross-section of the link showing the position of the back-end waveguide in AM coupling.

$I_{AMLED}$ is dominated by impact ionization, which has a stronger bias dependence [39] as compared to that of forward mode diffusion current.

Comparing Fig. 5.9 with Fig. 5.6, we also observe that for a given D and LED current, the coupling quantum efficiency in AM is always higher than in FM. This is mostly due to the combined effect of a lower AMLED

IQE and a stronger AMLED-PD spectral overlap as compared to that of the FMLED (see Fig. 5.5(b)).

Fig. 5.10(a) shows the measured and modeled $I_{SC}$ of the PD versus D for three values of $I_{AMLED}$. $I_{SC}$ decreases monotonically with increasing D. The mean rate of attenuation $\gamma_{AM} \approx 0.195$ dB $\mu m^{-1}$. Due to the small absorption lengths ($\sim 1$ μm) in Si for short wavelengths emitted by the AMLED, the SOI layer does not serve as a WG. Thus, only the back-end WG formed by the high index $Si_3N_4$ core and the surrounding $SiO_2$ cladding can serve as the waveguide as shown in Fig. 5.10(b). The observed attenuation in AM coupling can also be modeled by Eq. (5.6) using fit parameter $a \propto I_{AMLED}$, and $b \approx 130$ $cm^{-1}$. Note that $\gamma_{AM} > \gamma_{FM}$, because AM coupling occurs only through the back-end dielectric WG. The optical thickness ($n_{core} \cdot t$) of the nitride core is $\sim 10$ times smaller than that of the SOI waveguide core, which leads to weaker photon confinement and increased radiative loss [44]. Moreover, the $Si_3N_4$ surface roughness is likely higher than that of the SOI leading to a greater scattering loss [44]. Both effects will lead to a higher waveguide attenuation in AM coupling.

## 5.7 Heating in the AMLED and thermal coupling

*DC operation*: Heating is significant in AMLED operation and the photodiode junction temperature $T_j$ is affected by the LED power consumption $P_{AMLED}$ according to $\Delta T_j \propto P_{AMLED}$ [45, 46]. Therefore, the rise in $I_{SC}$ is partly contributed by this $T_j$ (see section 5.4). Heating is more pronounced in SOI technology as compared to bulk Si technology due to the relatively poor thermal conductivity $\kappa$ [47, 48] of the BOX layer in the former.

Extracting $\Delta T_j$ and separating the independent contributions of EL intensity L and junction temperature $T_j$ to the total $I_{SC}$ are not possible analytically as $V_{OC}$ and $I_{SC}$ are related by an implicit equation (Eq. (5.3)) with coupled dependencies on L and $T_j$. We, therefore do it empirically from the measured PD I-V characteristics by obtaining explicit and independent calibration maps: $I_{SC}(L)$, $I_{SC}(T)$, $V_{OC}(L)$, and $V_{OC}(T)$. Here T represents the temperature variable in general without distinguishing between that of the junction and that of the ambient. The relations of $V_{OC}$ and $I_{SC}$ of the PD with L and T are calibrated independently by using a commercial off-chip LED, to isolate optical from thermal effects, and by varying $T_0$ at a fixed L. The off-chip LED emits at 650 nm with a FWHM of 40 nm, which approximately emulates the emission spectrum of the AMLED.

From a physics point-of-view, heating is also possible in the PD due to absorption of high energy photons emitted by the AMLED. In an ideal scenario, if the IQE of the PD is unity, the optical power intercepted by the

PD is estimated by $I_{SC} \cdot V_{OC}$, which is ~ 4 pW for AM coupling (see Fig. 5.9 (a)). This is negligibly low compared to $P_{AMLED}$. Thus, the AMLED is the major source of heat generation in the optical link.





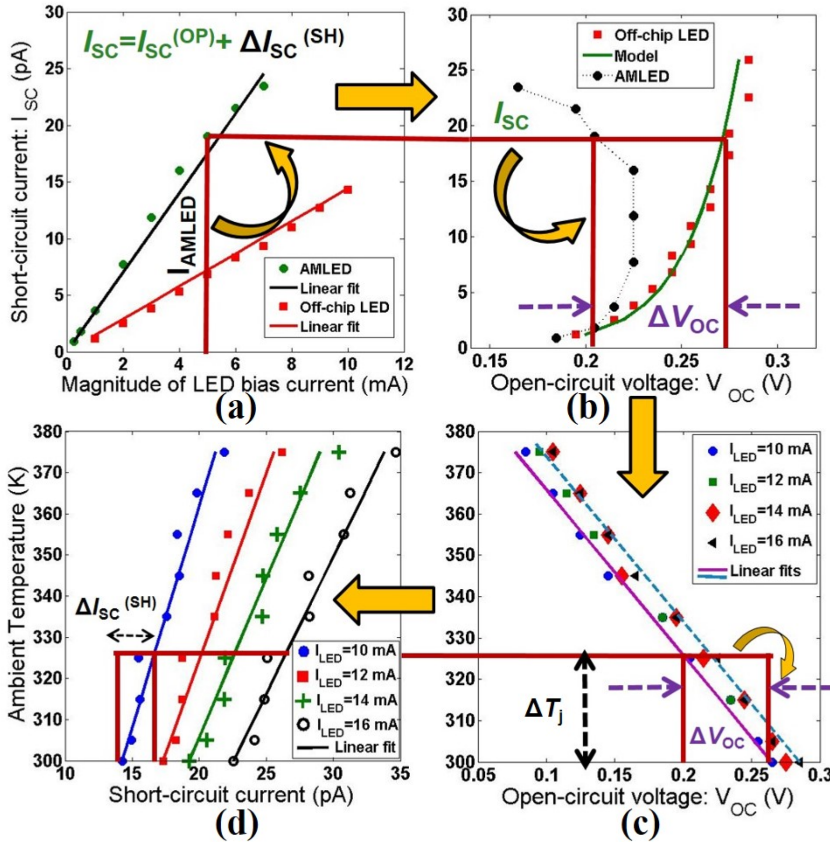


Figure 5.11: De-embedding procedure for separating the contributions of L and $\Delta T_j$ to the total $I_{SC}$ in AMLED operation in the default design (without heat sink): (a) $I_{SC}$ versus $I_{AMLED}$ at $T_0$ = 300 K. (b) Measured $V_{OC}$ (black) for AMLED operation and the calibrated value (green) using the off-chip LED at $T_0$ = 300 K and modeled by Eq. (5.3). (c) Calibrated $V_{OC}$-T curve and (d) $I_{SC}$-T curve of the PD for various off-chip LED currents (and hence L).

The following steps are followed (as shown in Fig. 5.11) for extracting thermal coupling in DC operation in our default design (without heat sink).

*Step 1*: $I_{SC}$ for a given $I_{AMLED}$ is measured and is assumed to be the sum of $I_{SC}^{(OP)}$ and $\Delta I_{SC}^{(SH)}$, which represent the independent contributions of L (optical) and $T_j$ respectively.

*Step 2*: Fig. 5.11(b) shows the variation of $I_{SC}$ versus $V_{OC}$ of the PD during AMLED operation and the calibrated pure optical variation at

$T_0$ = 300 K obtained using the off-chip LED. The deviation of $V_{OC}$ from the calibrated value, at the given $I_{SC}$ obtained in step 1, is recorded.

*Step 3*: Fig. 5.11(c) shows the calibrated $V_{OC}(T)$ for the PD for four different values of L of the off-chip LED. The slope of a linear fit of the ($V_{OC}$,T) data points yield a mean temperature coefficient $TC_{VOC}$ of -2.5 mV $K^{-1}$. The deviation $\Delta V_{OC}$ obtained in step 2, is then mapped onto the calibrated curve to obtain: $\Delta T_j = \frac{\Delta V_{OC}}{TC_{VOC}}$.

*Step 4*: Fig. 5.11(d) shows the calibrated $I_{SC}(T)$ for the PD, with a mean temperature coefficient $TC_{ISC}$ of 0.12 pA $K^{-1}$. The $\Delta T_j$ obtained in step 3 is then used to obtain $\Delta I_{SC}^{(SH)} = \Delta T_j \cdot TC_{ISC}$.

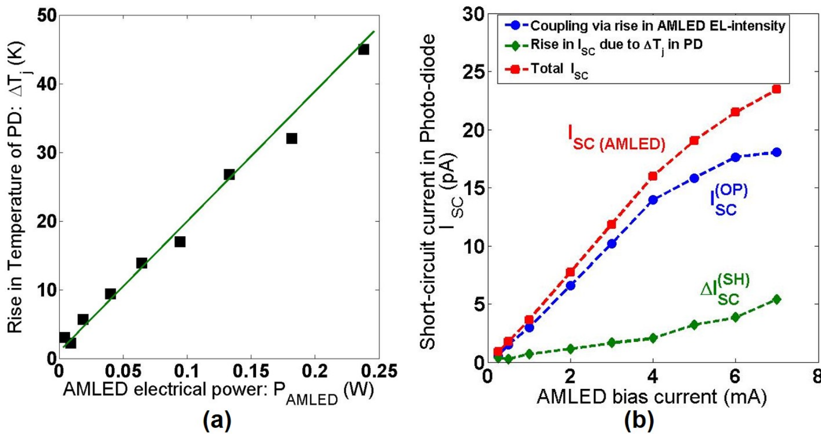


Figure 5.12: (a) Rise in PD junction temperature (symbols) because of heating in the AMLED in the default design of our optical link, following the procedure of Fig. 5.11. $\Delta T_j$ increases linearly with the LED electrical power $P_{AMLED}$. (b) The separated contributions of increasing L (blue) and increasing $T_j$ (green) to the total measured $I_{SC}$ (red).

Fig. 5.12(a) shows the extracted $\Delta T_j$ values at different $P_{AMLED}$. Fig. 5.12(b) shows the separated components of $I_{SC}$. In the default design, a maximum of around 13 % of the total $I_{SC}$ is contributed by thermal coupling. The slope of $I_{SC}^{(OP)}$ - $I_{AMLED}$ curve shows a gradual reduction for high values of $I_{AMLED}$. This is likely due to the combined T-dependencies of the IQE of AMLED $\eta_{LED}$, and that of $\eta_{WG}$. To investigate this hypothesis a bit further, the two efficiencies will be estimated. First, the coupling quantum efficiency $\eta_{AM} = I_{SC}^{(OP)} / I_{AMLED}$, as described earlier. Second, the IQE of the AMLED in the default design (without heat sink), measured vertically using the optical fiber (see section 5.3), obtained (in a.u.) as

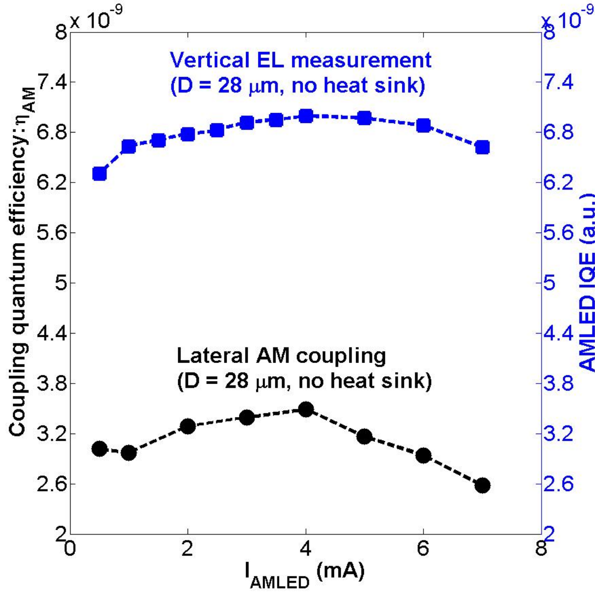


Figure 5.13: AMLED IQE (in blue, right axis) extracted via vertical EL-spectral measurement, and the AM coupling quantum efficiency (in black, left axis) extracted using the de-embedded $I_{SC}^{(OP)}$, plotted against $I_{AMLED}$ for the default optical link without heat sink.

$$\eta_{LED} = \frac{\int E(\lambda) d\lambda}{I_{AMLED}}. \tag{5.7}$$

Fig. 5.13 plots these two efficiencies against $I_{AMLED}$. It apeears that $\eta_{LED}$ reduces by ~ 6 % from its peak value, while $\eta_{AM}$ reduces by ~ 14 % of its peak value as $I_{AMLED}$ is increased till 7 mA. Such a reduction was not observed in the designs with heat sink (see Fig. 5.9). Thus, self-heating in the AMLED contributes partly to the drop in $\eta_{AM}$. The rest (~ 8 %) is possibly attributed to the T-dependency of $\eta_{WG}$, which was not investigated in this work.

*Transient operation*: In order to determine whether thermal coupling can affect the digital bit rates in data transfer, which in turn, affects the bandwidth, the link can be characterized by its thermal time constant $\tau_{TH} = R_{TH} \cdot C_{TH}$, where $R_{TH}$ and $C_{TH}$ are the effective thermal resistance and capacitance [45, 46] of the AMLED-link-PD system.

In order to extract $\tau_{TH}$, the AMLED is pulsed between "on" ($V_{AMLED}$ = 25 V) and "off" ($V_{AMLED}$ = 15 V) states at a pulse repetition frequency (PRF) of 1 Hz with a 50 % duty cycle and a 5 ns rise time, as shown in Fig. 5.14. In this measurement, the PD is biased at a constant forward bias current $I_{PD}$ = 1 mA. This bias ensures that $V_{PD}$ is sensitive only to $T_j$ with a mea-

sured temperature coefficient $TC_{VPD} = \partial V_{PD}/\partial T_j$ of -1.2 mV $K^{-1}$, and that $\partial V_{PD}/\partial L$ at a constant $T_j$ and constant $I_{PD}$ is negligible.

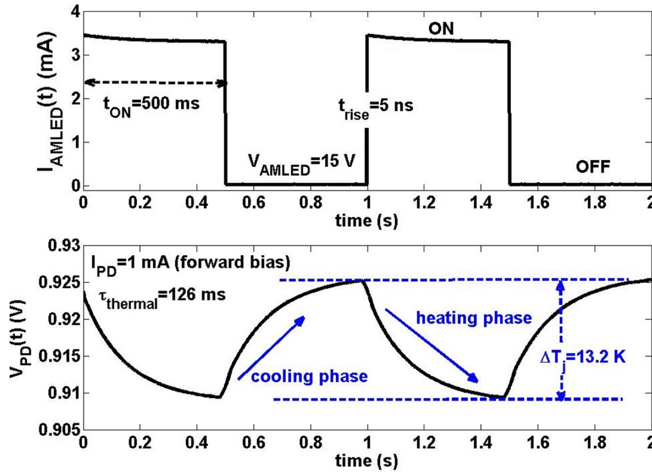


Figure 5.14: Measured transient waveforms of the pulsed AMLED current $I_{AMLED}(t)$ (top) and the resulting $V_{PD}(t)$ (bottom) when the PD is forward biased with a constant current of $I_{PD}$ = 1 mA for the design without heat sink. $V_{PD}$ shows a thermal RC relaxation behavior with a time constant $\tau_{TH}$ of 126 ms.

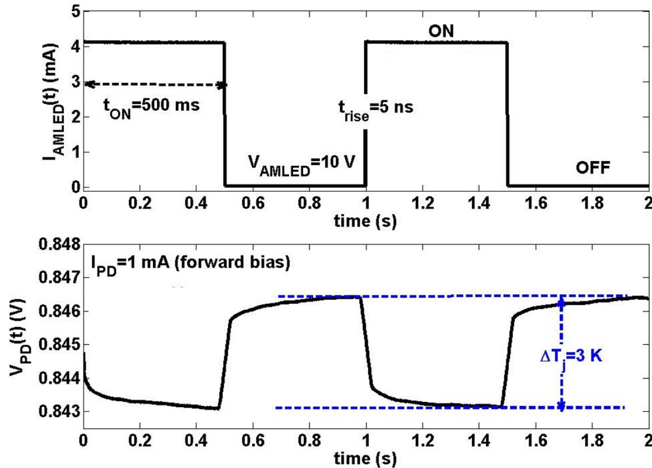


Figure 5.15: Measured transient waveforms of the pulsed AMLED current $I_{AMLED}(t)$ (top) and the resulting $V_{PD}(t)$ (bottom) when the PD is forward biased with a constant current of $I_{PD}$ = 1 mA for the design with heat sink. $V_{PD}$ shows a thermal RC relaxation behavior with a time constant $\tau_{TH}$ of 40 ms.

During the "on" phase, the AMLED heats up leading to the heating of the PD, which reduces $V_{PD}(t)$. In the "off" (cooling) phase, $V_{PD}(t)$ relaxes

back to its ambient value, exhibiting in both phases a first-order thermal RC behavior with $\tau_{TH}$ = 126 ms. Note that the electrical time constant of the measurement set-up (~ 5 ns) contributed by the PD and wiring parasitics is negligible compared to $\tau_{TH}$ and hence does not affect our measurement. Although heat propagates mainly via thermal phonons [49, 50], their propagation velocities are severely limited by the grain boundaries (crystallinity) of the material, defects, and interfaces between different materials. This is likely the reason for relatively large values of $\tau_{TH}$.



*Effect of heat sink*: $\Delta T_j$ can be reduced by including heat sinks. The heat sink significantly reduces the effective $R_{TH}$ of the link and thereby leads to a 6 times reduction in $\Delta T_j$ in DC operation (~ 30 K $W^{-1}$) compared to the same link without the heat sink (~ 180 K $W^{-1}$). The reduction of $R_{TH}$ also reduces $\tau_{TH}$ to 40 ms as shown in Fig. 5.15.

*Effect of link length*: The link length D (varying from 10 μm till 60 μm in steps of 10 μm) directly impacts the thermal propagation. Using pulsed measurements in all the designs at a PRF of 1 Hz, similar to the one in Fig. 5.15, a monotonic decrease in $\Delta T_j$ per unit $P_{AMLED}$ with increasing D has been obtained as shown in Fig. 5.16. Thus longer links have less thermal crosstalk.

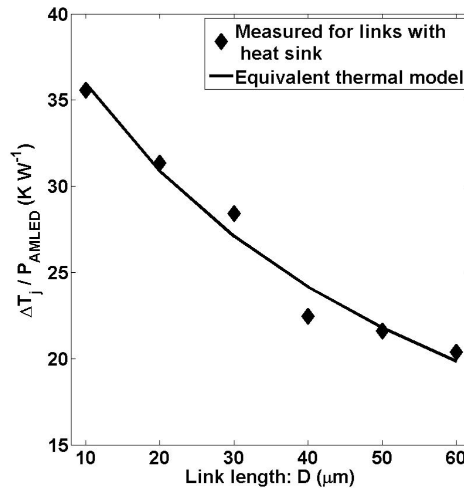


Figure 5.16: Measured versus modeled $\Delta T_j$ of the PD per unit $P_{AMLED}$ versus increasing D showing a monotonic decreasing behavior. A heat sink is present in the links used in this measurement. The modeled curve is obtained from Eq. 5.8.

The effects of adding a heat sink and changing the link length can be qualitatively understood using a thermal lumped π-network model with effective lateral (D-dependent) and vertical components of $R_{TH}$. Fig.

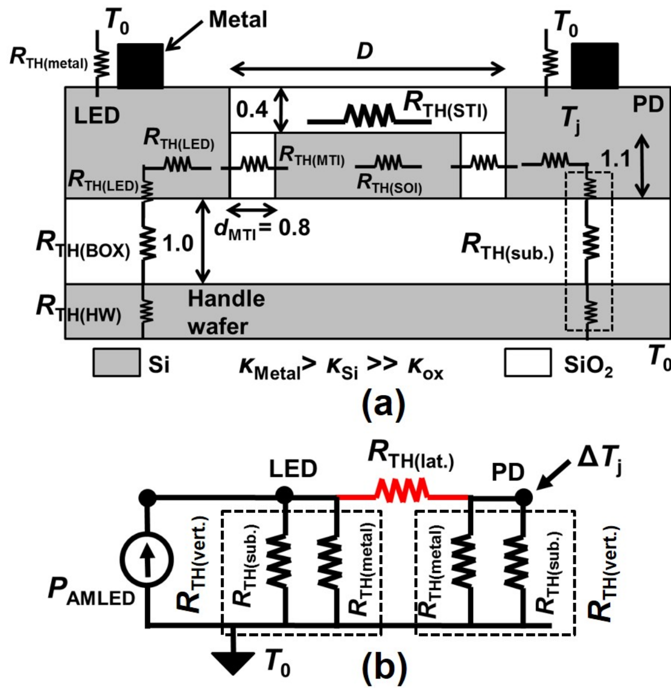


Figure 5.17: (a) A simplified 2-D cross-section of the optical link showing the important regions with their respective lumped thermal resistances, which is a function of their dimensions and the thermal conductivity κ of the material. The figure is not to scale. (b) The equivalent lumped π-network model.

5.17(a) shows a simplified 2-D cross-section of the optical link showing the important regions, their approximate dimensions, and their respective lumped thermal resistances. The thermal resistance is homologous to the electrical resistance of a body, where one replaces voltage and current in the electrical domain by change in temperature and input thermal power in the thermal domain. Note that the source of the thermal power is Joule heating in the AMLED, and thus is proportional to $P_{AMLED}$. For each indicated region of the link, $R_{TH} = l/(\kappa \cdot \sigma)$, where $l$ is the length along the direction of heat flow, $\kappa$ is the thermal conductivity, and $\sigma$ is the cross-sectional area normal to the direction of heat flow. Fig. 5.17(b) shows the equivalent lumped π-network, which is excited from the LED end by a DC power source $P_{AMLED}$. The lateral component $R_{TH(lat.)}$ is contributed mainly by the Si LED, PD, and the STI, MTI, and SOI layers. In addition, there is an effective vertical lumped component $R_{TH(vert.)}$, which is contributed by the LED/PD, the BOX layer, the handle wafer (represented together as $R_{TH(sub.)}$), and the metal electrodes ($R_{TH(metal)}$). In both the lateral and vertical components, there is also a contribution of the thermal resistances at the Si-$SiO_2$ interfaces. It can be derived that $R_{TH(lat.)}$ is a function of D (see Appendix C). In contrast, $R_{TH(vert.)}$ can be assumed to be insensitive

to D, and is thus a design-specific constant for the whole die, where all the test designs are present, and whose dimensions are much bigger than D. After solving this steady state $\pi$-network model, one can derive:

$$\Delta T_j(D) = \chi \cdot P_{AMLED} \cdot \frac{R^2_{TH(vert.)}}{R_{TH(lat.)}(D) + 2R_{TH(vert.)}}, \quad (5.8)$$

where the dimensionless parameter $\chi$ is the thermal conversion efficiency, i.e. the fraction of $P_{AMLED}$ that is converted to heat. It is a very reasonable to assume $\chi \approx 1$. This is because in conventional Si AMLEDs, the optical power conversion efficiency is very low ($\sim 10^{-6}$), as we observed in chapter 3. Eq. 5.8 fits the measured trend of decreasing $\Delta T_j$ with increasing D, for a fixed $P_{AMLED}$, and is shown in Fig. 5.16. Fitting is done via the Least Squares Method. Further details about the derivation of the thermal model and the extracted fit parameters are given in Appendix C.

## 5.8 Discussion and design recommendations

The main findings reported in sections 5.5 to 5.7, and their implications are as follows:

1. Within our measured range of $I_{LED}$, $\eta_{AM} > \eta_{FM}$. This result is an interplay of competing phenomena, encompassing $\eta_{LED}$, $\eta_{WG}$ and $\eta_{PD}$. Nonetheless, it is observed that both FM and AM coupling in standard CMOS is feasible.

2. The coupling efficiency $\eta$ decreases monotonically with increasing D, with the attenuation rates demonstrating waveguiding and thus anisotropic transmission. The rates of attenuation $\gamma_{FM}$ and $\gamma_{AM}$ are observed to be almost independent of the LED current. Further, $\gamma_{FM} < \gamma_{AM}$. A quantitative study on the optical transmission efficiency of the optical link, and on the waveguiding features of SOI-CMOS technology, which were not dealt herein in detail, will be discussed in the next chapter.

3. The different rates of attenuation in FM and AM coupling leads, for the particular design presented here, to a cross-over point in coupling efficiency around D = $D_T \approx 76$ µm, where the extrapolated measured values intersect as shown in Fig. 5.18. This indicates that for D < $D_T$, avalanche mode operation yields a higher $\eta$, while for longer link lengths forward mode operation of the LED is preferred from a coupling efficiency point-of-view.

4. The measured PD $I_{SC}$ is in the order of 10 pA in DC operation at $T_0$ = 300 K. For our optical link, this would enable data communication with an output (PD) referred signal-to-noise ratio (SNR) of

$\sim$ 15 dB for a bandwidth B of, e.g. 1 MHz, where

$$SNR = 10 \cdot \log \left[ \frac{I_{SC}^2}{2 \cdot q \cdot I_{SC} \cdot B} \right]. \quad (5.9)$$

Here shot noise is the main contributor for noise power [51]. A low SNR leads to a high bit error rate (BER) [52]. The SNR increases if $I_{SC}$ is increased. For this purpose, avalanche-photodiode (APD) based receivers can be employed because they leverage from the reverse multiplication factor (> 1) that generates a signal of $M \cdot I_{SC}$. Another distinct approach, especially when on-off keying is used in the communication link, is to use SPAD based receivers. SPADs provide a significant improvement in photon-sensitivity to compensate for the low $I_{SC}$, as compared to regular PDs or APDs, by operating in Geiger mode (above breakdown voltage). In this case, the BER is largely governed by the photon detection probability and dark count rate [28] of the SPAD.

5. Heating in the AM operation of the LED leads to an increase in the PD junction temperature $T_j$. During on-off keying of the AMLED, this leads to a parameter shift in the PD. However, given the significantly long thermal time constants (in the range 40-120 ms), no thermal data communication is expected during high speed opto-coupling; thermal coupling will at most lead to DC offsets at the receiver end. This offset will in turn depend on the "on" state duration and $P_{AMLED}$.

6. AM coupling consumes $\sim$ 10 times higher LED electrical power than FM coupling. However, the reported Si AMLED switching speed ($\sim$ GHz) is $\sim 10^3$ times higher than that reported for Si FMLEDs ($\sim$ MHz). Combined, this indicates that, for digital data communication, a reduction in "energy per bit" can be achieved in AM coupling as compared to FM coupling in Si.

From the analysis in this paper we can formulate several design recommendations to improve the optical link, and in particular its coupling quantum efficiency.

*Coupling in forward mode*: To enhance $\eta_{LED}$, the spacing between the contact and $n^+/p^+$ diffusion edge should be increased, which reduces the diffusion current [40]. Also, the injector/diffusion region widths should be reduced compared with that of the active region [53]. $T_{Fresnel}$ can be increased by having only one MTI (instead of two) for galvanic isolation between the LED and the PD. $\eta_{PD}$ can be enhanced by having both $d_{PD}$ and $W$ to be $> \alpha_{Si}^{-1}(\lambda)$, where $\alpha_{Si}^{-1}(\lambda)$ is the absorption length in Si. $\eta_{prop}$ can be increased by removing the STI and the nitride layer. The resulting single SOI WG will have a greater optical thickness ($n_{Si} \cdot t_{SOI}$) and lower

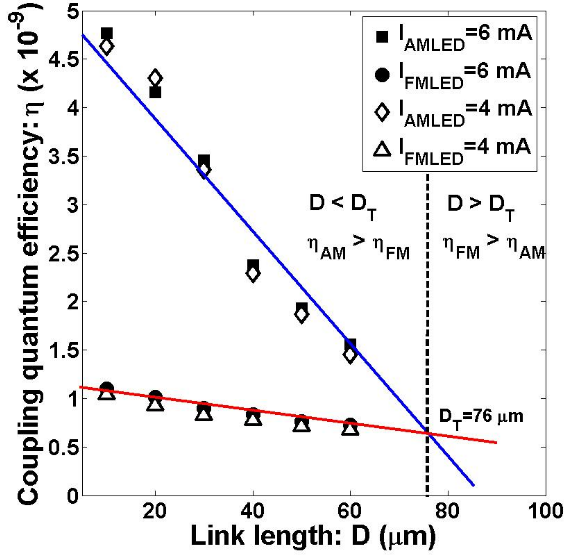


Figure 5.18: Measured coupling quantum efficiency η in AM and FM coupling versus link length D for our designs. A linear extrapolation of the data yields a cross-over point $D = D_T$ =76 μm.

absorption losses.

*Coupling in avalanche mode*: $\eta_{LED}$ can be enhanced by increasing the junction perimeter to area ratio. The LED dimension in the direction of optical propagation can be reduced to the order of $\alpha_{Si}^{-1}(\lambda)$. In addition, reducing the magnitude of $V_{BR}$ of the AMLED can not only increase its power efficiency [15] but also reduces the parasitic thermal coupling. $\eta_{PD}$ can be enhanced by having a lower doping level, which increases the depletion width and hence the responsivity. For links with SPAD based detectors, this recommendation is beneficial from the viewpoint of having a low dark count rate and high photon detection probability [27]. For the waveguide, $\eta_{in}$ (or $\eta_{out}$) can be enhanced by increasing the contact area between the EL-region of the LED (or the PD active area) and the nitride core. Lastly, $\eta_{prop}$ can be enhanced by patterning the WG on the $x$-$y$ plane, which would reduce the effect of D-dependent angular aperture of the PD.

A concise list of various extracted fit parameters used in this chapter can be found in Appendix C.

## 5.9 Conclusions

A monolithic, galvanically isolated, laterally-coupled and wide-spectrum (350 nm $< \lambda <$ 1270 nm) optical link in 0.14 μm silicon-on-insulator CMOS

technology has been demonstrated. Optical coupling has been analyzed in both forward and avalanche mode LED operation, quantified by the short-circuit current in the photodiode. The link exhibits a higher coupling quantum efficiency in avalanche mode LED operation as compared to forward mode LED operation. Coupling, especially through shorter wavelengths in avalanche mode, is made feasible via silicon dioxide and other inter-metal dielectrics like silicon nitride that form low-attenuation waveguide for the photons. High power dissipation and heating in the avalanche mode LED leads to an increase in the junction temperature of the photodiode, observed to be 180 K $W^{-1}$ (without heat sink) in DC operation of the LED. This is reduced to 30 K $W^{-1}$ by integrating a heat sink. Measured thermal time constants of our design are 120 ms (without a heat sink) and 40 ms (with a heat sink). Further, the coupling quantum efficiency has been experimentally shown to be monotonically decreasing with increasing link length, in agreement with a model that combines geometrical optics and attenuation.

## Supplementary Information: TCAD Raytracing animation to illustrate lateral aperture

The left and right squares represent the top-views of the Si LED and the Si PD, respectively. A ray of light (propagating from left to right) emanates from a point close to the periphery of the LED, and subsequently encounters two Si-$SiO_2$ interfaces to reach the PD. The angle of incidence is measured w.r.t. the horizontal axis.

# BIBLIOGRAPHY


[1] S. Dutta, V. Agarwal, R.J.E. Hueting, J. Schmitz, and A.J. Annema, "Monolithic optical link in silicon-on-insulator CMOS technology," Optics Express, vol. 25, no. 5, pp. 5440-5456, Mar. 2017.

[2] S. Dutta, R.J.E. Hueting, V. Agarwal, and A.J. Annema, "An integrated optical link in 140 nm SOI technology," Proc. Conference on Lasers and Electro-Optics, Session JW2A, paper no. 132, June 2016.

[3] X. Zheng, D. Patil, J. Lexau, F. Liu, G. Li, H. Thacker, Y. Luo, I. Shubin,J. Li, J. Yao, P. Dong, D. Feng, M. Asghari, T. Pinguet, A. Mekis, P. Amberg, M. Dayringer, J. Gainsley, H.F. Moghadam, E. Alon, K. Raj, R. Ho, J.E. Cunningham and A.V. Krishnamoorthy, "Ultra-efficient 10 Gb/s hybrid integrated silicon photonic transmitter and receiver," Opt. Express, vol. 19, no. 6, pp. 5172-5186, 2011.

[4] N. Rouger, L.T. Le, D. Colin and J-C. Crébier, "CMOS SOI Gate Driver with Integrated Optical Supply and Optical Driving for Fast Power Transistors," Proc. $28^{th}$ International Symposium on Power Semiconductor Devices (ISPSD), pp. 427-430, 2016.

[5] N. Van-Sang, L. Thang-Long, F. Sarrafin, T. Ngoc-Duc, D. Colin, N. Rouger, P. LeFranc, Y. Lembeye, J-D. Arnould, B. Allard and J-C. Crebier, "Contributions to dedicated gate driver circuitry for very high switching speed high temperature power devices," Proc. $28^{th}$ International Symposium on Power Semiconductor Devices (ISPSD), pp. 443-446, 2016.

[6] M.A. Green, J. Zhao, A. Wang, P.J. Reece and M. Gal, "Efficient silicon light-emitting diodes," Nature. vol. 412, pp. 805-808, 2001.

[7] T. Hoang, P. LeMinh, J. Holleman, V. Zieren, M.J. Goossens and J. Schmitz, "A High Efficiency Lateral Light Emitting Device on SOI," Proc. 12th IEEE International Symposium on Electron Devices for Microwave and Optoelectronic Applications, pp. 87-91, 2004.

[8] C. Schinke, D. Hinken, J. Schmidt, K. Bothe and R. Brendel, "Modeling the Spectral Luminescence Emission of Silicon Solar Cells and Wafers," IEEE J. Photovoltaics vol. 3, no. 3, 1038-1052, 2013.

[9] G. Piccolo, P.I. Kuindersma, L-Å. Ragnarsson, R.J.E. Hueting, N. Collaert and J. Schmitz, "Silicon LEDs in FinFET technology," Proc. $44^{th}$ European Solid State Device Research Conference (ESSDERC), pp. 274-277, 2014.

[10] B.P. van Drieënhuizen and R.F. Wolffenbuttel, "Optocoupler based on the avalanche light emission in silicon," Sensors and Actuators A, vol. 31, pp. 229-240, 1992.

[11] J. Schmitz, R. de Vries, C. Salm, T. Hoang, R.Hueting and J. Holleman, "On the switching speed of SOI LEDs," Proc. EUROSOI, pp. 101-102, 2008.

[12] A.G. Chynoweth and K.G. McKay, "Photon emission from Avalanche Breakdown in Silicon," Phys. Rev., vol. 102, no. 2, pp. 369-376, 1956.

[13] M. du Plessis, H. Aharoni, and L.W. Snyman, "Silicon LEDs fabricated in standard VLSI technology as components for all silicon monolithic integrated optoelectronic systems," IEEE J. Sel. Topics Quantum Electron., vol. 8, no. 6, pp. 1412-1419, 2002.

[14] L.W. Snyman, M. du Plessis, and H. Aharoni, "Injection-Avalanche-Based $n^+pn$ Silicon Complementary Metal Oxide Semiconductor Light-Emitting Device (450 - 750 nm) with 2-Order-of-Magnitude Increase in Light Emission Intensity," Jpn. J. Appl. Phys., vol. 46,

no. 4B, pp. 2474-2480, 2007.

[15] S. Dutta, R.J.E. Hueting, A.J. Annema, L. Qi, L.K. Nanver and J. Schmitz, “Opto-electronic modeling of light emission from avalanche-mode silicon $p^+n$ junctions,” J. Appl. Phys., vol. 118, 114506, 2015.

[16] A. Chatterjee, B. Bhuva, and R. Schrimpf, “High-speed light Modulation in avalanche breakdown mode for Si diodes,” IEEE Electron Device Lett., vol. 25, no. 9, pp. 628-630, 2004.

[17] H-C. Lee and C-K. Liu, “Si-based current-density-enhanced light emission and low-operating-voltage light-emitting/receiving designs,” Solid State Electronics, vol. 49, pp. 1172-1178, 2005.

[18] M. Sergio and E. Charbon, “An intra-chip electro-optical channel based on CMOS single photon detectors,” IEEE International Electron Devices Meeting (IEDM) Tech. Digest, Paper no. 822, 2005.

[19] B. Huang, X. Zhang, W. Wang, Z. Dong, N. Guan, Z. Zhang, and H. Chen, “CMOS monolithic optoelectronic integrated circuit for on-chip optical interconnection,” Opt. Commun., vol. 284, pp. 3924-3927, 2011.

[20] A. Khanmohammadi, R. Enne, M. Hofbauer, and H. Zimmermann, “Monolithic Integrated Optical Random Pulse Generator in High Voltage CMOS Technology,” Proc. European Solid State Device Research Conference (ESSDERC), pp. 138-141, 2015.

[21] L.W. Snyman, H. Aharoni, A. Biber, A. Bogalecki, L. Canning, M. du Plessis and P. Maree, “Optical sources, integrated optical detectors, and optical waveguides in standard silicon CMOS integrated circuitry,” Proc. SPIE, vol. 3953, Silicon-based Optoelectronics II, pp. 20-36, 2000.

[22] K. Xu, B. Huang, K.A. Ogudo, L.W. Snyman, H. Chen, and G.P. Li, “Silicon Light-emitting Device in Standard CMOS technology,” Proc. 8th International Photonics and OptoElectronics Meetings, paper no. OT1C.3, 2015.

[23] D. Li, W. Li, L. Duan, G. Zhang, S. Liu, and G. Dong, “Highly Integrable Organic Optocouplers on a Patterned Double-Side Indium Tin Oxide Substrate With High Isolation Voltage,” IEEE Electron Device Lett., vol. 36, no. 2, pp. 171-173, 2015.

[24] R. Dangel, J. Hofrichter, F. Horst, D. Jubin, A. La Porta, N. Meier, I.M. Soganci, J. Weiss, and B.J. Offrein, “Polymer waveguides for electro-optical integration in data centers and high-performance computers,” Opt. Express, vol. 23, no. 4, pp. 4736-4750, 2015.

[25] J. Chen, N. Bamiedakis, P. Vasil’ev, T. Edwards, C. Brown, R. Penty, and I. White, “High-Bandwidth and Large Coupling Tolerance Graded-Index Multimode Polymer Waveguides for On-board High-Speed Optical Interconnects,” J. Lightwave Tech., vol. 34, no. 12, pp. 2934-2940, 2015.

[26] P. Wessels, M. Swanenberg, H. van Zwol, B. Krabbenborg, H. Boezen, M. Berkhout, and A. Grakist, “Advanced BCD technology for automotive, audio and power applications,” Solid-State Electronics, vol. 51, pp. 195-211, 2007.

[27] S. Mandai, M. W. Fishburn, Y. Maruyama and E. Charbon, “A wide spectral range single-photon avalanche diode fabricated in an advanced 180 nm CMOS technology,” Opt. Express, vol. 20, no. 6, pp. 5849-5857, 2012.

[28] M-J. Lee, P. Sun and E. Charbon, “A first single-photon avalanche diode fabricated in standard SOI CMOS technology with a full characterization of the device,” Opt. Express, vol. 23, no. 10, pp. 13200-13209, 2015.

[29] B.G. Streetman, and S.K. Banerjee, *Solid State Electronic Devices*, $6^{th}$ ed. (PHI Learning Pvt. Ltd., 2009).

[30] David J. Griffiths, *Introduction to Electrodynamics*, $3^{rd}$ ed., ISBN $81-7758-293-3$ (Pearson Education, 1999).

[31] L. Yan, G. Koops, P. Steeneken, A. Heringa, R. Surdeanu, L. van Dijk, “Integrated heat sinks for SOI power devices,” Proc. 25th International Symposium on Power Semiconductor Devices (ISPSD), pp. 285-288, 2013.

[32] Robert F. Pierret, *Semiconductor Device Fundamentals* (Addison-Wesley Publ., 1996).

[33] M. Lahbabi, A. Ahaitouf, M. Fliyou, E. Abarkan, J.-P. Charles, A. Bath, A. Hoffmann, S.E. Kerns and D.V. Kerns, Jr., “Analysis of electroluminescence spectra of silicon and gallium arsenide p-n junctions in avalanche breakdown,” J. Appl. Phys., vol. 95, no. 4, pp. 1822-1828, 2004.

[34] M.A. Green, “Self-consistent optical parameters of intrinsic silicon at 300 K including temperature coefficients,” Solar Energy Materials & Solar Cells, vol. 92, pp. 1305-1310, 2008.

[35] G.E. Giakoumakis, “Matching Factors for Various Light-Source-Photodetector Combinations,” Appl. Phys. A, vol. 52, pp. 7-9, 1991.

[36] M.A. Green, and M.J. Keevers, “Optical properties of intrinsic silicon at 300 K,” Progress in photovoltaics, vol. 3, pp. 189-192, 1995.

[37] E.F. Schubert, *Light Emitting Diodes* (Cambridge University Press, 2006).

[38] K. Rajkanan, R. Singh, and J. Schewchun, “Absorption coefficient of silicon for solar cell calculations,” Solid-State Electronics, vol. 22, pp. 793-795, 1979.

[39] R.J.E. Hueting, A. Heringa, B.K. Boksteen, S. Dutta, A. Ferrara, V. Agarwal, and A.J. Annema, “An Improved Analytical Model for Carrier Multiplication Near Breakdown in Diodes,” IEEE Trans. Electron Devices, vol. 64, no. 1, pp. 264-270, 2017.

[40] V. Puliyankot and R.J.E. Hueting, “One-dimensional Physical Model to Predict the Internal Quantum Efficiency of Si-Based LEDs,” IEEE Trans. Electron Devices, vol. 59, no. 1, pp. 26-34, 2012.

[41] K.A. Ogudo, D. Schmieder, D. Foty, and L.W. Snyman, “Optical propagation and refraction in silicon complementary metal-oxide-semiconductor structures at 750 nm: toward on-chip optical links and microphotonic systems,” J. Micro/Nanolith. MEMS MOEMS, vol. 12, no. 1, 013015, 2013.

[42] I.H. Malitson, “Interspecimen Comparison of the Refractive Index of Fused Silica,” J. Opt. Soc. Am., vol. 55, pp. 1205-1208, 1965.

[43] M.J. Adams, “Loss calculations in weakly-guiding optical dielectric waveguides,” Opt. Comm., vol. 23, no. 1, pp. 105-108, 1977.

[44] G.T. Reed, A.P. Knights, *Silicon Photonics: An Introduction* (John Wiley and Sons Ltd, 2004).

[45] L.T. Su, J.E. Chung, D.A. Antoniadis, K.E. Goodson and M.I. Flik, “Measurement and modeling of self-heating in SOI nMOSFET’s,” IEEE Trans. Electron Devices, vol. 41, no. 1, pp. 69-75, 1994.

[46] W. Jin, W. Liu, S.K.H. Fung, P.C.H. Chan and C. Hu, “SOI Thermal Impedance Extraction Methodology and Its Significance for Circuit Simulation,” IEEE Trans. Electron Devices, vol. 48, no. 4, pp. 730-736, 2001.

[47] M.B. Kleiner, S.A. Kühn and W. Weber, “Thermal Conductivity Measurements of Thin Silicon Dioxide Films in Integrated Circuits,” IEEE Trans. Electron Devices, vol. 43, no. 9, pp. 1602-1609, 1996.

[48] M. Asheghi, K. Kurabayashi, R. Kasnavi and K.E. Goodson, “Thermal conduction in doped single-crystal silicon films,” J. Appl. Phys., vol. 91, pp. 5079-5088, 2002.

[49] R. Berman, *Thermal conduction in solids* (Oxford University Press, 1976).

[50] M. Kaviany, *Essentials of heat transfer* (Cambridge University Press, 2011).

[51] S.M. Sze and K.K. Ng, *Physics of Semiconductor Devices* 3rd edition, John Wiley & Sons, Inc., USA, 2007.

[52] J. Genoe, D. Coppée, J.H. Stiens, R.A. Vounckx, and M. Kuijk, “Calculation of the current response of the spatially modulated light CMOS detector,” IEEE Trans. Electron Devices, vol. 48, no. 9, pp. 1892-1902, 2001.

[53] V. Puliyankot, G. Piccolo, R.J.E. Hueting, A. Heringa, A. Kovalgin, and J. Schmitz, “Increased Light Emission by Geometrical Changes in Si LEDs,” Proc. 8th IEEE International Conference on Group IV Photonics, pp. 287-289, 2011.

# CHAPTER 6

# WIDE-SPECTRUM OPTICAL WAVEGUIDING IN SOI-CMOS TECHNOLOGY

**Abstract**

This chapter presents a technology computer-aided design (TCAD) based analysis on wide-spectrum (480 nm $< \lambda <$ 1300 nm), dielectric slab waveguides based on silicon-on-insulator and silicon nitride for monolithic integration of optical links with on-chip, wide-spectrum, low-intensity and isotropic light sources in silicon-on-insulator (SOI)-CMOS technologies. Geometrical conditions for waveguiding are discussed and transmission efficiencies are estimated using finite difference time domain (FDTD) simulation for varying optical wavelengths emitted by conventional silicon-based wide-spectrum light-emitting diodes. In addition, the effects of waveguide geometry, and galvanic isolation on the transmission efficiencies are reported.

*"I do not know what I may appear to the world, but to myself I seem to have been only like a boy playing on the seashore, and diverting myself in now and then finding a smoother pebble or a prettier shell than ordinary, whilst the great ocean of truth lay all undiscovered before me."* (Isaac Newton)

---

This chapter is an extension of the work presented at the $17^{th}$ IEEE International Conference on Numerical Simulation of Optoelectronic Devices (NUSOD), 2017 [1].

## 6.1 Introduction

The integration of photonic functionality in CMOS is promising for high-speed data communication, and opto-electronic system-on-chip applications. For most contemporary photonic and/or opto-electronic integrated circuits [2–6], CMOS technology is commonly extended with a dedicated optical waveguide (WG) layer having a low absorption coefficient ($\alpha$) and a high refractive index ($n$) for photonic functionalities [2]. Some industrial CMOS technologies, however, offer built-in thin films suitable as WGs, the most common being the silicon (Si) layer in silicon-on-insulator (SOI) technology [2, 6–8]. In the previous chapter, a monolithic optocoupler [7] designed in 0.14 μm Bipolar CMOS-DMOS (BCD)-SOI technology was presented, which not only includes an SOI layer as a WG for infrared (IR) light, but also a thin silicon nitride ($Si_3N_4$) film laid atop the active Si surface, which is a potential WG for visible and IR light [8–13]. In addition, the optocoupler comprises an Si LED that exhibits wide-spectrum ($400$ nm $< \lambda <$ $1300$ nm ) and isotropic electroluminescence (EL). An Si photodiode (PD) detects light laterally. Such features of the LED, combined with the inherent off-axis alignment of the WGs w.r.t. the LED and the PD, makes the optical transmission efficiency $\eta_t(\lambda)$ rather difficult to analyze by means other than numerical simulation such as the Finite Difference Time Domain (FDTD) simulation. Significant prior studies and characterizations of $\eta_t(\lambda)$ were performed on SOI and $Si_3N_4$ based WGs [8–13], but the scope was limited to high-intensity, monochromatic and external laser sources with off-chip coupling and long range transmission. In contrast, our study caters to complex geometry of an SOI device, on-chip isotropic optical excitation, and short-haul transmission.

Section 6.2 of this chapter shows, using opto-electronic TCAD simulations in the Sentaurus Device tool [14], the built-in WG conditions for SOI and $Si_3N_4$ layers leading to anisotropic transmission based on ray optics. In section 6.3 hybrid-mode (mixed TE and TM polarizations) EM wave simulations [15] are performed to estimate the $\lambda$-dependent transmission efficiency $\eta_t(\lambda)$ where it is also shown how $\eta_t(\lambda)$ is affected by the geometry of the optocoupler, namely the core thickness $t$, link spacing $L$, and galvanic isolation (only in SOI). Although FDTD simulation can be done using many other tools (e.g. COMSOL, Lumerical, etc.), Sentaurus TCAD has been chosen in this work because it combines the capability of solving Maxwell's equations with that of performing opto-electronic simulations in semiconductors, commonly used in industrial CMOS technology. Section 6.4 provides a further discussion on the obtained simulation results, and their implications on the overall coupling efficiency of the optocoupler. Finally, section 6.5 concludes our work.

## 6.2 Geometrical conditions for waveguiding

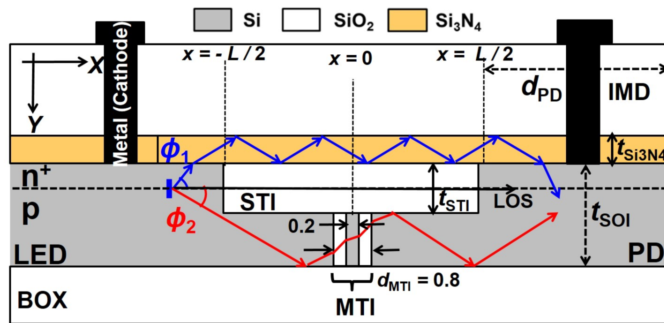


Figure 6.1: A schematic cross-section of the SOI-based optocoupler showing relevant parameters and design features, and two example ray-traces when guided via the $Si_3N_4$ (blue) and the SOI WGs (red).

Fig. 6.1 shows the schematic 2-D cross-section of the key features of a typical SOI-based optocoupler as described in the previous chapter; a p-n junction Si LED and PD, the shallow trench isolation (STI), the medium trench isolation (MTI), the buried oxide (BOX), the $Si_3N_4$ layer, and a back-end $SiO_2$ layer, also known as inter-metal dielectric (IMD). The length of the STI layer (composed of $SiO_2$) will henceforth be termed as link length or WG length L. The MTI column is typically composed of $SiO_2$ reinforced by a thin silicon core. This feature is used for galvanic isolation between different voltage domains in smart power SOI technologies such as BCD technology. The $Si_3N_4$ layer is relatively thin (limited to a few hundred nm in most SOI CMOS technologies [9, 16]), and generally used as an etch-stop layer prior to opening contacts during fabrication. The maximum thickness of the nitride layer is limited by thermal-induced stress between $Si_3N_4$ and $SiO_2$ [10].

Consider a ray of light originating from a point along the p-n junction (EL region of the LED), within one attenuation length from the STI edge ($x = -L / 2$), making an angle $\phi$ w.r.t. the positive x-axis (Fig. 6.1). The value of $\phi$ determines the photon trajectory in the optocoupler. To simplify our understanding, only the range $-90^o < \phi < 90^o$ is considered. Rays with any other $\phi$ are assumed to be self-absorbed within the LED and do not contribute to the propagation along the positive x-axis. This is valid provided that the LED dimensions are larger than the attenuation length for the maximum $\lambda$ of interest.

Three dominant propagation mechanisms for the light ray can be identified as follows.

1. Line-of-sight (LOS) propagation occurs along the $x$-axis within a small aperture $|\phi| < \delta$ through the STI, where $\delta$ depends on L, the STI thickness ($t_{STI}$), refractive indices of Si ($n_{Si}(\lambda)$), and $SiO_2$ ($n_{SiO2}(\lambda)$). The propagation loss is mainly due to Fresnel reflections at the two Si-STI interfaces and self-absorption in the Si LED. $SiO_2$ has negligible absorption in the entire spectral range of interest: 480 nm $< \lambda <$ 1300 nm [17].

2. In-plane guiding occurs via the SOI core cladded with $SiO_2$ in the STI and the BOX. The index contrast between Si ($\sim$ 4.0) and $SiO_2$ ($\sim$ 1.45) in the SOI WG is high. Moreover, attenuation is low in the IR spectrum due to a significantly lower absorption coefficient of Si [18]. Waveguiding via the SOI WG (without MTI) occurs if the condition for total internal reflection (TIR) is satisfied at the SOI-BOX interface [19] (see Fig. 6.3(a)):

$$\phi > -\cos^{-1}\left(\frac{n_{SiO2}(\lambda)}{n_{Si}(\lambda)}\right). \tag{6.1}$$

If an MTI column is present in the SOI layer (see Fig. 6.3(b)), then the necessary WG condition is additionally constrained at the SOI-MTI interface by

$$\phi > -\sin^{-1}\left(\frac{n_{SiO2}(\lambda)}{n_{Si}(\lambda)}\right). \tag{6.2}$$

The above two inequalities are depicted graphically in Fig. 6.2(a). Note that the MTI column leads to an additional Si-$SiO_2$ interface perpendicular to the $x$-axis, which reduces the range of $\phi$ for which propagation occurs.

3. The thin $Si_3N_4$ layer with $SiO_2$ cladding (STI and IMD) forms a WG. Ideally, $Si_3N_4$ has negligible absorption in 480 nm $< \lambda <$ 1300 nm [20]. However, in practice, the crystalline quality and stoichiometry of this layer is sensitive to its fabrication technique [21]. Such defects, combined with the rough interface between $Si_3N_4$ and the low-index IMD (like $SiO_2$) in CMOS back-end, results in additional propagation losses due to volume and surface scattering. In this WG, light must couple first from the Si LED directly into $Si_3N_4$, and post-propagation also couple from $Si_3N_4$ into the Si PD. Such an out-of-plane coupling and subsequent guiding through the nitride core requires the fulfillment of the following two constraints:

$$n_{Si}(\lambda) > n_{Si3N4}(\lambda) > n_{SiO2}(\lambda), \text{ and} \tag{6.3}$$

$$\cos^{-1}\left(\frac{n_{SiO2}(\lambda)}{n_{Si}(\lambda)}\right) > \phi > \cos^{-1}\left(\frac{n_{Si3N4}(\lambda)}{n_{Si}(\lambda)}\right). \tag{6.4}$$

The first constraint is valid at all $\lambda$. The second constraint is related to the TIR criterion. This is depicted graphically in Fig. 6.2(b) and Fig. 6.3(c). For any $\lambda$, $\phi$ has to lie in the region bounded by the two curves. The top (squares) curve represents the left-hand bound of condition (6.4), while the bottom (circles) curve represents the right-hand bound of condition (6.4). One can infer from the figure that increasing the spectral range $\Delta\lambda$ to be coupled via the $Si_3N_4$ WG, leads to a reduction in the allowed range of incident angles $\Delta\phi$.

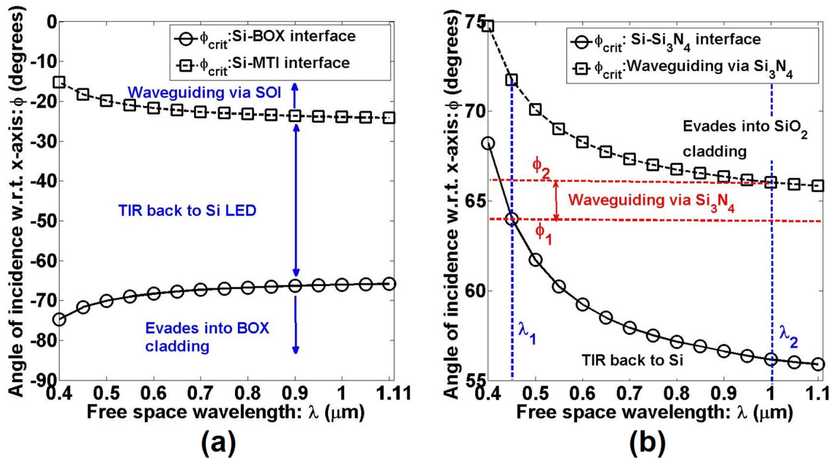


Figure 6.2: Graphical representation of the range of $\phi$ as a function of $\lambda$ for which waveguiding can occur via (a) the SOI WG (see also Fig. 6.3a,b), and (b) the $Si_3N_4$ WG (see also Fig. 6.3(c)).

The dispersion relations $n_{Si}(\lambda)$, $n_{SiO2}(\lambda)$, and $n_{Si3N4}(\lambda)$, assumed for this analysis are referred from the work of Green and Keevers [18], Malitson [22], and Philipp [20], respectively. In TCAD, these relations are used as well to obtain the wavelength dependent coefficients of $n$ and extinction coefficient $k$.

The constraints on $\phi$ affect the optical transmission, which can be captured by extracting the TCAD simulated gain $G_{PD}$ in the PD, defined as

$$G_{PD} = 20 \cdot \log\left(\frac{I_{PD}}{I_{dark}}\right). \tag{6.5}$$

Fig. 6.4(a) and (b) show two examples of raytraces in the $Si_3N_4$ and the SOI WG respectively for the indicated geometries. Fig. 6.4(c) shows the TCAD simulated $G_{PD}$ versus $\phi$ at $\lambda = 1100$ nm, and intensity of 1 mW cm$^{-2}$. A polar plot has been chosen for the sake of better comprehensibility and visualization, analogous to a "directivity" plot of a radiating source [23]. This choice of $\lambda$ ensures negligible material absorption in both the WGs. Here

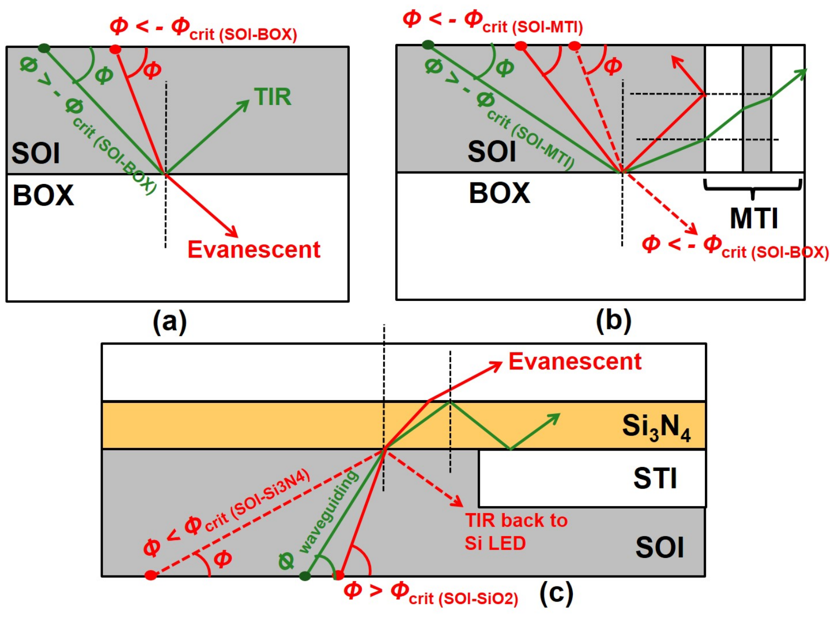


Figure 6.3: Schematic representation of ray propagation to illustrate the constraints on $\phi$ for which waveguiding can occur via (a) the SOI WG without MTI, (b) the SOI WG with MTI, and (c) the $Si_3N_4$ WG.

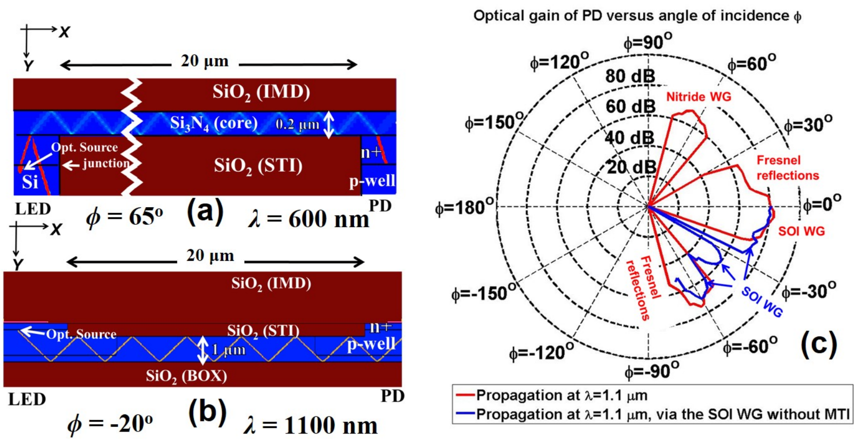


Figure 6.4: Raytraces showing propagation via (a) the $Si_3N_4$ WG at $\lambda$ = 600 nm, and $\phi$ = 65°, (b) the SOI WG without MTI at $\lambda$ = 1100 nm, and $\phi$ = -20°. (c) TCAD simulated $G_{PD}$ versus $\phi$ at $\lambda$ = 1100 nm, showing the directional dependency of optical propagation via the $Si_3N_4$, the STI, and the SOI layer with and without an MTI column.

$I_{dark}$ is the dark current flowing through the PD at a small reverse bias (~2 V). In most SOI technologies [16], the SOI thickness ($\lesssim$ 1 µm) is smaller than the diffusion length of minority carriers along the y-axis. Hence, the

entire PD region drawn in Fig. 6.1 contributes to $I_{PD}$, considering optical propagation along the x-axis. A ray of light originating from a point source in the p-n junction of the Si LED can reach the PD via the $Si_3N_4$ WG, the SOI WG, or the STI. Note that due to the choice of a relatively long λ, and a short L = 20 μm in this particular simulation, some rays also reach the PD via stray Fresnel reflections at various interfaces and boundaries of the structure. These reflections are very specific to the geometry, boundary conditions, and location of the point source; hence a systematic study of their contribution is difficult. As L increases, and λ decreases, the contributions from such reflections become progressively less significant. When the ray of light reaches the PD, it shows up in the form of a lobe in the $G_{PD}$ versus ϕ polar plot. A flowchart of the FDTD simulation procedure using ray optics is shown in Fig. 6.5(a).

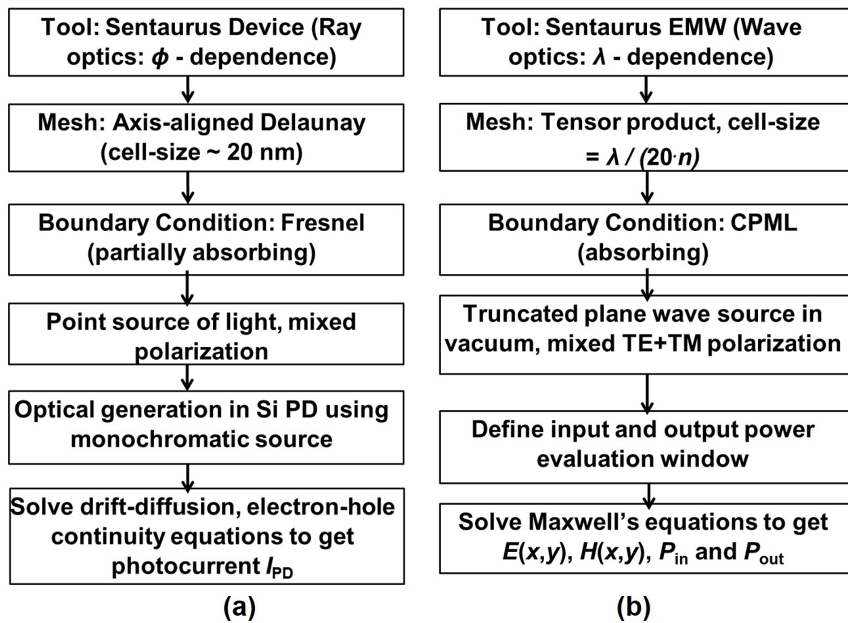


Figure 6.5: Flowchart of the main steps involved in the FDTD simulation of the waveguides using the (a) ray optic method, and (b) wave optic method.

## 6.3 Spectral transmission efficiency ($\eta_t$)

In this section, we study the effect of both geometry and λ on the transmission efficiency for optical propagation via the $Si_3N_4$ and the SOI WGs. Raytracing simulation (as done in Section 6.2) is insufficient in this regard since the geometries involved are comparable with the optical wavelengths. Moreover, in raytracing solvers only a single mesh point can be assigned as a light source at a time, and multiple simultaneous excitations are needed to incorporate multiple values of ϕ. This makes the simulation unnecessar-

ily complicated and time consuming. Thus, a wave optical approach must be resorted to, which is included in the EM wave solver in Sentaurus. The EMW tool works on a tensor-product mesh, unlike the axis-aligned mesh in raytracing. To ensure convergence of the Finite Difference Time Domain (FDTD) simulation, a wavelength-dependent meshing strategy is adopted. In the present work, a mesh density of 20 nodes per wavelength was used (in both $x$ and $y$ directions). A finer mesh yields more accuracy at the cost of increased computation time.



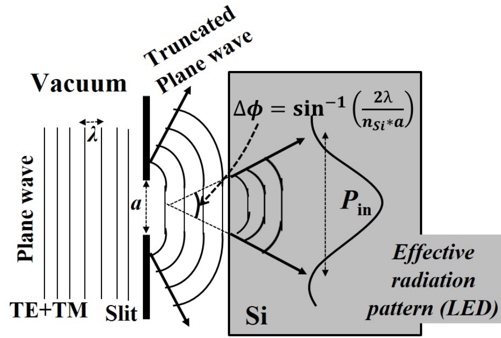


Figure 6.6: Definition of the truncated plane wave excitation having spatial divergence $\Delta\phi$ to mimic a multi-modal optical source inside a lossy dispersive medium (silicon). This approximates a radiation pattern of an LED.

As shown in Fig. 6.6, a spread in $\phi$ is enforced by defining a truncated plane wavefront as the excitation, which exhibits spatial divergence. However, the EM wave solver used in this work comes with a constraint; the optical excitation must be defined in vacuum and cannot be defined inside any lossy dispersive medium. In order to comply with this additional constraint, the excitation window is placed in vacuum and the boundary termination of the test structure is modified as required in each case to mimic the optical environment of the device, as discussed in the coming paragraphs. In each simulation, the Convolutional Perfectly Matched Layer (CPML) boundary condition [24] is assumed in both $x$ and $y$ directions at the surfaces/edges of the device structure. CPML is an advanced absorbing boundary condition, which absorbs waves impinging the boundary with a wide range of incidence angles. This eliminates unwanted angle-dependent scattering, and reflections from the terminations of our structure. Moreover, it is important to mention that non-ideal behavior such as scattering losses due to a rough core-cladding interface, and non-uniformity of optical properties in a material have been ignored for simplicity. A flowchart of the FDTD simulation procedure using wave optics is shown in Fig. 6.5(b).

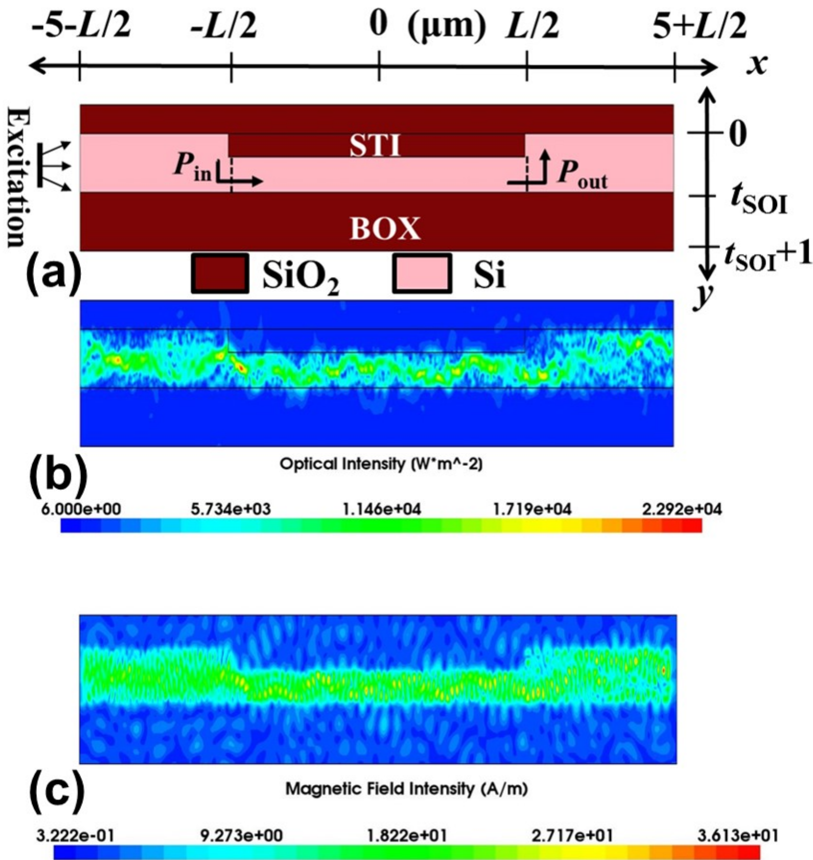


Figure 6.7: (a) The SOI WG: The time-averaged and y-integrated input ($P_{in}$) and output ($P_{out}$) optical powers are evaluated at x=-0.5 L and x=0.5 L respectively. Convolutional Perfectly Matched Layer (CPML) boundary conditions [24] are assumed at the edges of the structure in both x and y directions, and $t_{STI}$=0.4 μm. (b) Optical intensity profile and (c) Magnetic field intensity profile for L = 20 μm, $t_{SOI}$ = 1 μm, and λ=1100 nm.

### 6.3.1 The SOI WG

Fig. 6.7(a) shows the structure used as our simulation input deck. A truncated plane-wave (TPW) excitation with mixed TE and TM polarization and a fixed intensity that has spatial divergence, is used to mimic our Si-embedded optical source. The time-averaged and y-integrated input ($P_{in}$) and output ($P_{out}$) optical powers are evaluated at x=–0.5 L and x=0.5 L respectively. The simulated profiles for optical intensity and the magnetic field intensity H(x,y) are shown for λ = 1100 nm in Figs. 6.7(b) and (c) respectively, showing optical confinement and guiding via the SOI layer. Note that the thickness of the WG core is $t_{SOI} - t_{STI}$.

In Fig. 6.8(a), we observe that for a fixed $t_{SOI}$ = 1 μm, and any given

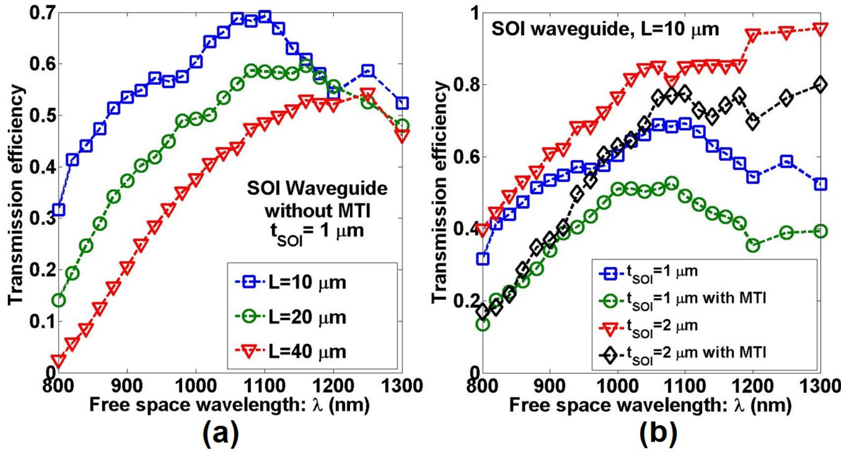


Figure 6.8: Simulated $\eta_t(\lambda)$ of propagation via the SOI WG for (a) different L and fixed $t_{SOI}$, and (b) the effect of MTI for different $t_{SOI}$ at a fixed L.

L, $\eta_t$=$P_{out}/P_{in}$ first increases with increasing $\lambda$ due to a sharp decrease in the absorption coefficient of Si ($\alpha_{Si}$) [25], reaches a maximum at a certain $\lambda_{peak}$, and eventually decreases gradually due to a reduction in the mode-propagation efficiency for longer $\lambda$ (also referred to as radiative losses [26]). When absorption losses in the Si core becomes negligible for longer $\lambda$, $\eta_t(\lambda)$ is governed by the power confinement factor (PCF) in the WG core [27, 28]. The PCF increases as the so-called V-number ($V(\lambda)$) [27] of the WG increases, where

$$V = \frac{2\pi \cdot (t_{SOI} - t_{STI}) \cdot (n_{Si}^2 - n_{SiO2}^2)^{\frac{1}{2}}}{\lambda}. \tag{6.6}$$

Since V decreases sharply with increasing $\lambda$ for a fixed core thickness $t_{SOI} - t_{STI}$, the PCF and consequently $\eta_t$ reduces with $\lambda$.

Further, for a fixed $\lambda$, $\eta_t$ decreases with increasing L due to absorption. For $\lambda > 1150$ nm (corresponds to Si band gap of 1.12 eV), $\eta_t$ is significantly less sensitive to L, due to negligible absorption at such long $\lambda$. In Fig. 6.8(b), we observe that for a fixed L, $\eta_t(\lambda)$ increases as $t_{SOI}$ is increased from 1 μm to 2 μm, due to increased mode-propagation efficiency. Again, this happens due to an increased PCF caused by an increase in V (see Eq. (6.6)). This also explains the observation that $\eta_t(\lambda)$ increases to $\lambda$ = 1300 nm for $t_{SOI}$ = 2 μm; $\lambda_{peak}$ being shifted beyond 1300 nm. Further, the presence of the MTI, leads to a fixed additional 20 % reduction in $\eta_t$ for any L and $t_{SOI}$, caused by Fresnel reflections at the Si-$SiO_2$ interfaces. The ripples in $\eta_t(\lambda)$ are likely caused by inter-modal interference.

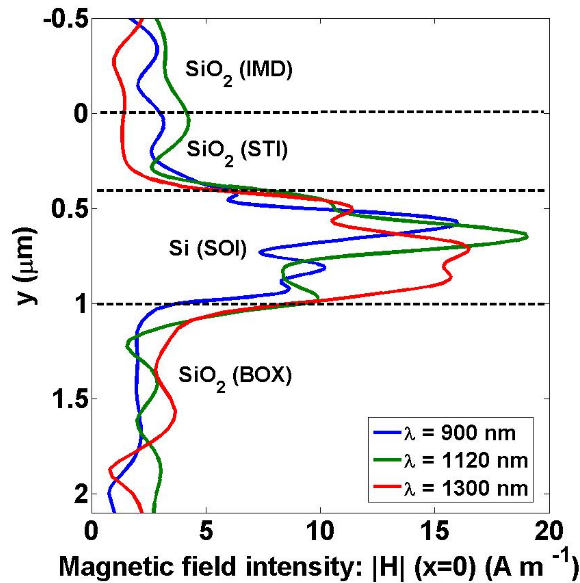


Figure 6.9: Simulated profile of the magnetic field intensity (absolute value) along the $y$-axis at $x = 0$, and various $\lambda$ for the SOI WG (without MTI, $L = 20$ μm, $t_{SOI} = 1$ μm).

To further elucidate the $\lambda$-dependence of the transmission efficiency of the SOI WG, the $|H|$-field profiles along the $y$-axis at $x = 0$ for three different $\lambda$ are shown in Fig. 6.9. As $\lambda$ increases, the field spreads out more into the cladding. The peak field lies inside the SOI core, whose magnitude first increases as $\lambda$ increases from 900 nm to 1120 nm (due to reduced absorption in Si), and then decreases as $\lambda$ further increases to 1300 nm (due to a reduction in the V-number).

### 6.3.2 The $Si_3N_4$ WG

Fig. 6.10(a) shows the structure used to simulate the $Si_3N_4$ WG. The TPW excitation (constrained by the solver to be placed in vacuum) is given an initial orientation $\phi \approx 62^o$. This mimics our Si-based optical source without violating the aforesaid necessary conditions for waveguiding. The dashed lines represent the power evaluation windows used for input and output in order to calculate $\eta_t(\lambda)$. Figs. 6.10(b) and (c) show the intensity profile and $H(x,y)$ respectively at $\lambda = 600$ nm, showing optical confinement and out-of-plane guiding. Light is coupled in from the Si LED into $Si_3N_4$, and is coupled out from $Si_3N_4$ to the Si PD. For the physical dimensions involved in typical SOI technologies and also in this simulation exercise, the $Si_3N_4$ core is optically much thinner ($\sim$ 10 times) than the SOI core, where the optical thickness is the product of refractive index and the physical thickness ($n \cdot t$). This implies that the V-number for the $Si_3N_4$ WG is

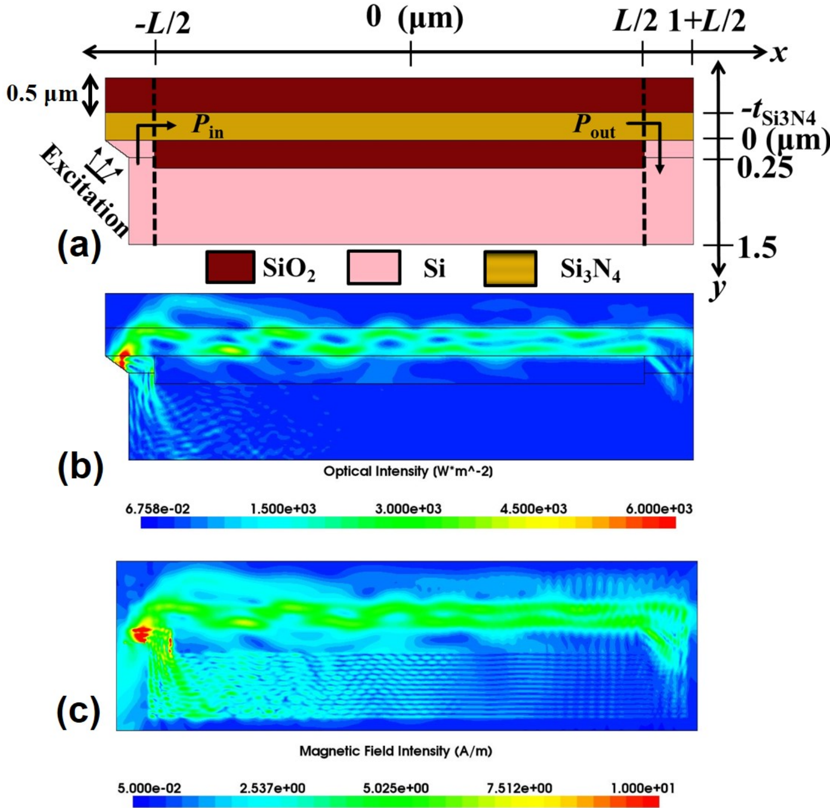


Figure 6.10: (a) The $Si_3N_4$ WG: Time-averaged and $y$-integrated input ($P_{in}$) and output ($P_{out}$) optical powers are evaluated at $x = -0.5$ L and $x = 0.5$ L respectively. CPML boundary conditions are assumed for both $x$ and $y$ axes. (b) Optical intensity profile and (c) Magnetic field intensity profile for L = 20 µm, $t_{Si3N4} = 0.4$ µm, and $\lambda = 600$ nm.

proportionately smaller as compared to the SOI WG (Eq. 6.6). Hence, the PCF in the $Si_3N_4$ core is less [27], thereby increasing the radiative losses [26]. Consequently, the material and dimensions of the cladding layers, as well as the SOI layer running underneath the STI layer can affect the spectral transmission efficiencies for the $Si_3N_4$ WG.

In Fig. 6.11(a), we observe that for a fixed $t_{Si3N4}$ and L, $\eta_t$ falls sharply with increasing $\lambda$, due to a reduction in V-number and hence the PCF. A slight increase in $\eta_t$ is observed for $\lambda \geqslant 1100$ nm, which can be explained by an increased edge-coupling to the underlying SOI layer due to a thin ($\approx 0.4$ µm) STI cladding. Further, $\eta_t(\lambda)$ shows a relatively small L-dependence (attenuation) than observed in the SOI case, due to the negligible extinction coefficient and thus $\alpha_{Si3N4}$. Thus, only radiative losses (due to finite cladding thicknesses) account for the small L-dependent attenuation. A greater L-dependence is observed for $\lambda > 800$ nm, where the

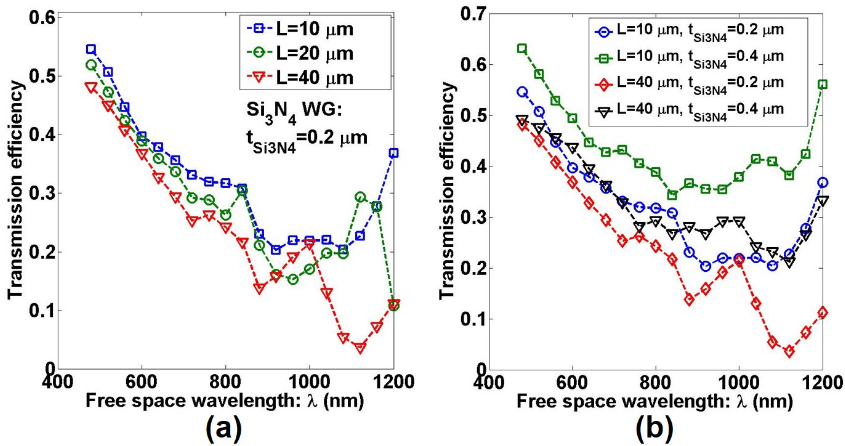


Figure 6.11: Simulated $\eta_t(\lambda)$ of propagation via the $Si_3N_4$ WG for (a) different L and fixed $t_{Si3N4}$, and (b) different $t_{Si3N4}$ and L.

coupling via the SOI layer kicks in. As such, $\eta_t(\lambda)$ reduces with increasing L due to absorption in the SOI layer. The ripples in the curve are likely caused by inter-modal interference. In real structures, however, a higher attenuation is expected [7] (see also Chapter 5) because of roughness in the core-cladding interface and volume scattering due to lattice defects in the core [26] (ignored in our simulation). In Fig. 6.11(b), we observe that for any L, as $t_{Si3N4}$ is doubled from 0.2 μm to 0.4 μm, a ~ 15 % increase in $\eta_t(\lambda)$ is observed due to increased V-number and hence PCF in the core.

To further elucidate the λ-dependence of the transmission efficiency of the $Si_3N_4$ WG, the |H|-field profiles along the $y$-axis at $x = 0$ for three different λ are shown in Fig. 6.12. As λ increases, the field spreads out more into the $SiO_2$ cladding (STI and IMD). Since the STI is only 0.4 μm thick, the field couples into the SOI layer underneath; the coupling strengthening with increasing λ. In particular, for $\lambda > 1100$ nm, the peak H-field shifts to the SOI layer. For $\lambda < 1100$ nm, the peak of the propagating H-field lies inside the $Si_3N_4$ core, whose magnitude decreases as λ increases from 600 nm to 1120 nm due to a reduction in the V-number, and hence the PCF. Note that for $\lambda > 1100$ nm, since the coupling via the SOI layer becomes significant, the inclusion of the BOX layer underneath affects the H-field profile as shown in Fig. 6.13 for $\lambda = 1120$ nm. When the BOX layer is included (which has a higher refractive index than vacuum), the peak H-field in both the $Si_3N_4$ core is reduced and also vertically shifted away from the $Si_3N_4$-IMD interface. Further, the H-field penetrates deeper into the BOX layer as compared to free-space (vacuum) termination (due to a reduced index contrast w.r.t. the SOI layer).

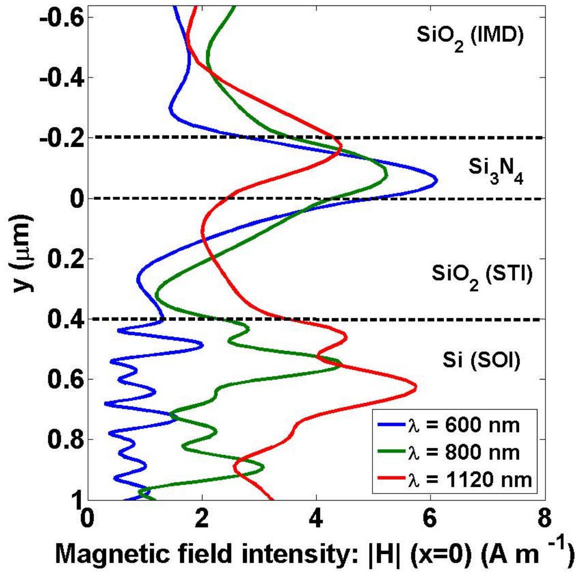


Figure 6.12: Simulated profile of the magnetic field intensity (absolute value) along the $y$-axis at $x = 0$, and various $\lambda$ for the $Si_3N_4$ WG ($L = 10$ μm, $t_{Si3N4} = 0.2$ μm).

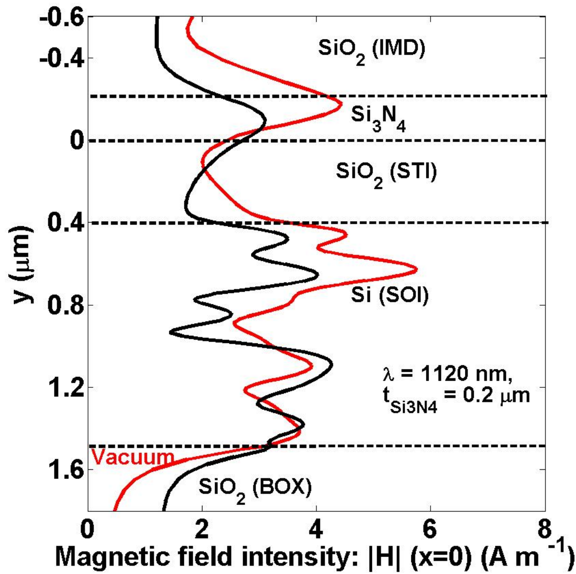


Figure 6.13: Simulated profile of the magnetic field intensity (absolute value) along the $y$-axis at $x = 0$, and $\lambda = 1120$ nm for the $Si_3N_4$ WG ($L = 10$ μm, $t_{Si3N4} = 0.2$ μm) with the SOI layer terminated with vacuum (red) and terminated with the BOX layer (black).

## 6.4 Discussion and implications

The analysis done so far can be further used to estimate the coupling efficiency of the SOI based optocoupler. The estimation of spectral transmission efficiencies for the different optical paths, plus the knowledge of the $\phi$-dependency of each path can be combined to construct a single design-specific curve $\eta_{comb}(\lambda)$, which yields the combined (cumulative) efficiency weighted over the $\phi$-domain for the optocoupler system, defined as follows:

$$\eta_{comb}(\lambda) = \sum_{i=1}^{2} w_i(\lambda) \cdot \eta_i(\lambda), \tag{6.7}$$

where $i$ denotes an optical path ($Si_3N_4$, or SOI WG), and $w_i(\lambda) = \Delta\phi_i/\pi$ is the weight assigned to the $i$th optical path, where $\Delta\phi_i$ is the range bounded by the inequalities (6.1), (6.2) (only when MTI is present), and (6.4) . This definition aids us to mimic a scenario where the waveguide is optically excited by a range of $\phi$, e.g. via a conventional Si based LED that emits photons more or less isotropically. Fig. 6.14 plots $\eta_{comb}(\lambda)$ for the indicated geometries. The transmission is dominated by the $Si_3N_4$ WG for $\lambda$ <800 nm, and by the SOI WG for $\lambda$ >800 nm.

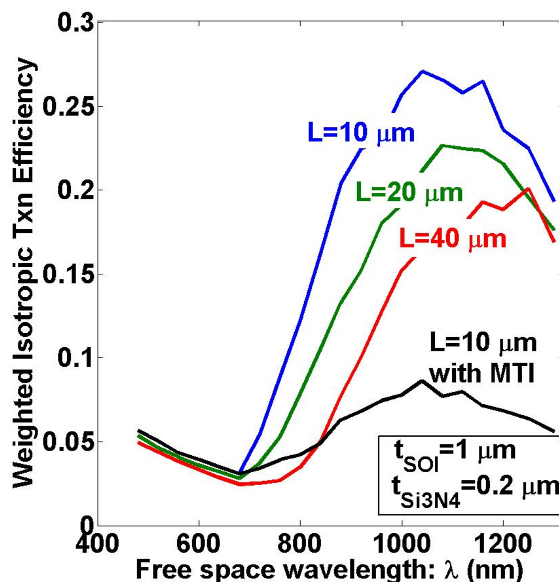


Figure 6.14: $\phi$-weighted cumulative transmission efficiencies ($\eta_{comb}$) as defined in Eq. (6.7) for indicated geometrical parameters assuming isotropic EL combining both the optical paths: $Si_3N_4$ WG, and SOI WG.

As a further application, let us now revisit the concept of coupling efficiency as discussed in chapter 5. The emission specific responsivity

($S$) of the PD was shown therein, where only the spectral irradiance of the LED and the TCAD simulated monochromatic responsivity of the PD were multiplied according to Eq. (5.4). This exercise yielded a 100 times higher $S$ for the normalized avalanche-mode EL-spectrum as compared to a normalized forward-mode EL-spectrum. However, the waveguide transmission efficiency was not included in that calculation. The combined spectral transmission efficiency obtained by the numerical simulations in this chapter provides a more accurate understanding of the concept of spectral overlap which affects the coupling quantum efficiency (CQE) of the optocoupler. By introducing the additional factor $\eta_{comb}(\lambda)$, we can rewrite Eq. (5.4) as:

$$\tilde{S} = \int \eta_{comb}(\lambda) \cdot E(\lambda) \cdot \frac{I_{SC}(\lambda)}{P_{opt}} d\lambda, \tag{6.8}$$

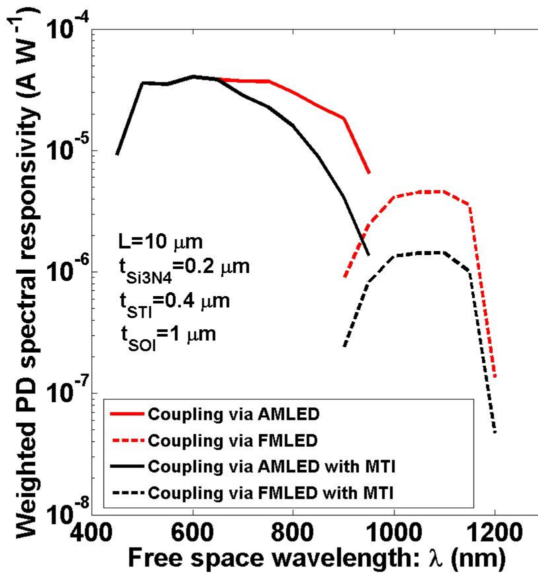


Figure 6.15: Emission and transmission-specific spectral responsivity of the Si PD given by the integrand of Eq. (6.8)

where $E(\lambda)$ is the power-normalized spectral irradiance of the LED, and $I_{SC}(\lambda)$ is the short circuit current generated in the PD, when illuminated by monochromatic light of free-space wavelength $\lambda$ with power $P_{opt}$ (see section 5.4 in the previous chapter). Fig. 6.15 plots the integrand of Eq. (6.8) for the indicated geometrical parameters. This is a modified version of the original Fig. 5.5 in the previous chapter. A ~ 20 times higher $\tilde{S}$ is obtained for the AM EL-spectrum as compared to the FM EL-spectrum, thereby demonstrating that for a unit $P_{opt}$, the CQE is still higher in the visible spectrum. It must be stressed that this comparison assumes the same total optical power in both AM and FM LED operation. Since the IQE

of Si FMLEDs are reported to be higher than that of Si AMLEDs [29, 30] , this means that both forward and avalanche mode LED operation can yield more or less a similar order of magnitude for the CQE, provided that the LED and PD designs are optimized separately for FM and AM electroluminescence. Our measurements discussed in the previous chapter with two MTI columns between the LED and the PD, yielded a ~ 6 times higher CQE in AMLED operation. It should also be noted that in that design, both the optical power and the profile of the EL-area of the LED in FM and AM were different.

## 6.5 Conclusions

A numerical FDTD analysis has been presented on wide-spectrum (480 nm $< \lambda <$ 1300 nm), dielectric slab waveguides based on silicon-on-insulator and silicon nitride for integration of optical links with monolithic, wide-spectrum, low-intensity and isotropic light sources in SOI-CMOS technology. Geometrical conditions for waveguiding have been discussed. Transmission efficiencies have been estimated for varying geometry and optical wavelengths emitted by conventional Si-based wide-spectrum LEDs. It has been observed that transmission is dominated by the $Si_3N_4$ WG for $\lambda$ <800 nm, and by the SOI WG for $\lambda$ >800 nm. For the latter, the incorporation of a medium trench isolation (MTI) as a galvanic isolation feature leads to a ~ 20 % reduction in the transmission efficiency. A thicker SOI layer leads to a higher $\eta_t(\lambda)$ but also a higher inter-modal interference. Out-of-plane waveguiding occurs via the optically thin $Si_3N_4$ layer, which should be present between the active Si and the top $SiO_2$ cladding for excitation at the LED end. The shallow trench isolation and the inter-metal dielectric serve as the cladding layers for this WG. The analysis can be extended to more complex optical links, and also to simulate 3-D systems.

# BIBLIOGRAPHY


[1] S. Dutta, L. Orbe, and J. Schmitz, "TCAD analysis of wide-spectrum waveguides in high-voltage SOI-CMOS," Proc. $17^{th}$ IEEE International Conference on Numerical Simulation of Optoelectronic Devices (NUSOD), p. MC4, 2017 (DOI:10.1109/NUSOD.2017.8009969).

[2] C. Sun, M.T. Wade, Y. Lee, J.S. Orcutt, L. Alloatti, M.S. Georgas, A.S. Waterman, J.M. Shainline, R.R. Avizienis, S. Lin, B.R. Moss, R. Kumar, F. Pavanello, A.H. Atabaki, H.M. Cook, A.J. Ou, J.C. Leu, Y-H. Chen, K. Asanović, R.J. Ram, M.A. Popović, and V.M. Stojanović, "Single-chip microprocessor that communicates directly using light," Nature, vol. 528, pp. 534-538, 2015.

[3] M. du Plessis, H. Aharoni, and L.W. Snyman, "Silicon LEDs fabricated in standard VLSI technology as components for all silicon monolithic integrated optoelectronic systems," IEEE J. Sel. Topics Quantum Electron., vol. 8, no. 6, pp. 1412-1419, 2002.

[4] B. Huang, X. Zhang, W. Wang, Z. Dong, N. Guan, Z. Zhang, and H. Chen, "CMOS monolithic optoelectronic integrated circuit for on-chip optical interconnection," Opt. Commun., vol. 284, pp. 3924-3927, 2011.

[5] A. Khanmohammadi, R. Enne, M. Hofbauer, and H. Zimmermann, "Monolithic integrated optical random pulse generator in high voltage CMOS technology," Proc. European Solid State Device Research Conference (ESSDERC), pp. 138-141, 2015.

[6] N. Rouger, L.T. Le, D. Colin and J-C. Crébier, "CMOS SOI gate driver with integrated optical supply and optical driving for fast power transistors," Proc. $28^{th}$ International Symposium on Power Semiconductor Devices (ISPSD), pp. 427-430, 2016.

[7] S. Dutta, V. Agarwal, R.J.E. Hueting, J. Schmitz, and A.J. Annema, "Monolithic optical link in silicon-on-insulator CMOS technology," Opt. Express, vol. 25, no.4, pp. 5440-5456, 2017.

[8] R. Baets, A.Z. Subramanian, S. Clemmen, B. Kuyken, P. Bienstman, N. Le Thomas, G. Roelkens, D. Van Thourhout, P. Helin, and S. Severi, "Silicon Photonics: silicon nitride versus silicon-on-insulator,"
in proc. OFC 2016, p. Th3J.1.

[9] A.Z. Subramanian, P. Neutens, A. Dhakal, R. Jansen, T. Claes, X. Rottenberg, F. Peyskens, S. Selvaraja, P. Helin, B. Du Bois, K. Leyssens, S. Severi, P. Deshpande, R. Baets, and P. Van Dorpe, "Low-loss singlemode PECVD silicon nitride photonic wire waveguides for 532-900 nm wavelength window fabricated within a CMOS pilot line," IEEE Photonics J., vol. 5, no. 6, p. 2202809, 2013.

[10] M. Melchiorri, N. Daldosso, F. Sbrana, L. Pavesi, G. Pucker, C. Kompocholis, P. Bellutti, and A. Lui, "Propagation losses of silicon nitride waveguides in the near-infrared range," Appl. Phys. Lett., vol. 86, 121111, 2005.

[11] H. Yamada, "Analysis of optical coupling for SOI waveguides," Piers Online, vol. 6, no. 2, pp. 165-168, 2010.

[12] G. Li, J. Yao, Y. Luo, H. Thacker, A. Mekis, X. Zheng, I. Shubin, J-H. Lee, K. Raj, J.E. Cunningham, and A.V. Krishnamoorthy, "Ultralow-loss, high-density SOI optical waveguide routing for macrochip interconnects," Opt. Express, vol. 20, no. 11, pp. 12035-12039, 2012.

[13] F. Grillot, L. Vivien, S. Laval, and E. Cassan, "Propagation loss in single-mode ultrasmall square silicon-on-insulator optical waveguides," J. Lightwave Tech., vol. 24, no. 2, pp. 891-896, 2006.

[14] Sentaurus Device User Guide, version H-2013.03, Synopsys Inc., 2013.

[15] Sentaurus Device Electromagnetic Wave Solver User Guide, version H-2013.03, Synopsys Inc., 2013.

[16] P. Wessels, M. Swanenberg, H. van Zwol, B. Krabbenborg, H. Boezen, M. Berkhout, and A. Grakist, "Advanced BCD technology for automotive, audio and power applications," Solid-State Electronics, vol. 51, pp. 195-211, 2007.

[17] L. Gao, F. Lemarchand, and M. Lequime, "Refractive index determination of $SiO_2$ layer in the UV/Vis/NIR range: spectrophotometric reverse engineering on single and bi-layer designs," J. Europ. Opt. Soc. Rap. Public., vol. 8, 13010, 2013.

[18] M.A. Green, and M.J. Keevers, "Optical properties of intrinsic silicon at 300 K," Progress in photovoltaics, vol. 3, pp. 189-192, 1995.

[19] E. Hecht, "*Optics*," $4^{th}$ ed. (Pearson Addison Wesley, 2002).

[20] H.R. Philipp, "Optical properties of silicon nitride," J. Eelctrochemical Soc., vol. 120, pp. 295-300, 1973.

[21] B. Rangarajan, A.Y. Kovalgin, K. Wörhoff, and J. Schmitz, "Low-temperature deposition of high-quality silicon oxynitride films for CMOS-integrated optics," Opt. Lett., vol. 38, no. 6, pp. 941-943, 2013.

[22] I.H. Malitson, "Interspecimen comparison of the refractive index of fused silica," J. Opt. Soc. Am., vol. 55, pp. 1205-1208, 1965.

[23] E.F. Schubert, "*Light Emitting Diodes*," (Cambridge University Press, 2006).

[24] A. Taflove, and S.C. Hagness, "*Computational Electrodynamics: The Finite-Difference Time-Domain Method*," (Boston: Artech House, $3^{rd}$ ed., 2005).

[25] M.A. Green, "Self-consistent optical parameters of intrinsic silicon at 300 K including temperature coefficients," Solar Energy Materials & Solar Cells, vol. 92, pp. 1305-1310, 2008.

[26] G.T. Reed, and A.P. Knights, "*Silicon Photonics An Introduction,*" ISBN 0-470-87034-6 (John Wiley & Sons Ltd., England, 2004).

[27] A.W. Snyder, and J.D. Love, "*Optical Waveguide Theory*," (Chapman and Hall, New York, USA, 1983).

[28] S.N. Kulkarni, and S.R. Patrikar, "Schrödinger wave equation for confinement of photon in a waveguide," J. Modern Opt., vol. 59, no. 16, pp. 1391-1395, 2012.

[29] L.W. Snyman, M. du Plessis, and H. Aharoni, "Injection-Avalanche-Based $n^{+}$pn silicon complementary metal oxide semiconductor light-emitting device (450 - 750 nm) with 2-order-of-magnitude increase in light emission intensity," Jpn. J. Appl. Phys., vol. 46, no. 4B, pp. 2474-2480, 2007.

[30] M.A. Green, J. Zhao, A. Wang, P.J. Reece and M. Gal, "Efficient silicon light-emitting diodes," Nature. vol. 412, pp. 805-808, 2001.

CHAPTER 7

# Summary & Recommendations

In this chapter, the most important conclusions presented in this thesis are summarized, followed by a discussion about recommendations for future work. Finally, a list of the original contributions is presented.

## Chapter 2

In this chapter, a model to establish a relationship of light emission from avalanche breakdown in Si $p^+n$ junctions with the applied reverse bias voltage has been demonstrated. The model predicts the primary dependence of the emission spectrum on the hot carrier temperature which can be derived from the (effective) electric field. The effect of bias on the relative increase in emission intensity has been modeled for devices with two different breakdown voltages. The model shows good agreement with our experiments. However, a variation in the spatial profile of electroluminescence was observed possibly caused by local defects. In particular, it is recommended to extend this work by studying the influence of defects, and surface states on the avalanche mode optical emission profile and intensity. In addition, the model includes only inter-band electronic transitions as the mechanism for electroluminescence. More intricate modeling, which involves e.g. Monte-Carlo simulations on carrier distribution functions, and also the contributions from other mechanisms like direct inter-band transitions and intra-band relaxations, can be pursued.

Avalanche-mode electroluminescence can also be studied in the purview of other semiconductors such as Germanium. With a much smaller bandgap of ~ 0.67 eV, but with similar relative permittivity as silicon, lower breakdown voltages can be achieved. An ultra-shallow $p^+n$ junction in a Ge-on-Si substrate has been reported in [1]. Hence, optical coupling in Ge-integrated CMOS technology is yet another future direction for research.

Integration of Ge in CMOS for optical receivers has already advanced in recent years for e.g. monolithic Ge-on-SOI based photodetectors [2, 3], fully depleted Ge CMOS logic devices [4], etc.

## Chapter 3

In this chapter, the dependency of optical power efficiency $\eta$ on the breakdown voltage $V_{BR}$ of avalanche-mode (AM) $p^+$-n-$n^+$ junction silicon (Si) LEDs in silicon, designed in a standard 65 nm bulk CMOS technology, has been shown experimentally and explained with analytical models. The experiments show a maximum $\eta$ at $V_{BR} \sim 6$ V, which is in agreement with our proposed opto-electronic model, when applied on trapezoidal field profiles. The model further predicts the value of such an optimal $V_{BR}$ for two idealized configurations; viz. abrupt $p^+$-n and p-i-n diodes. The model opens new prospects for further experimental validation, using more advanced Si technologies in the future. Moreover, the model can be improved, for instance by incorporating 2-D or 3-D electron temperature and consequently emission profiles, and by incorporating effects such as tunneling into the model, which have been ignored so far in this work.
In addition, further investigation of the influence of technology and device geometry on the shape of the relative spectral irradiance curve is recommended. As a separate remark, a detailed study on optical and electrical reliability of AMLEDs is yet another interesting topic.

## Chapter 4

In this chapter, Avalanche-mode (AM) superjunction (SJ) light-emitting diodes (LEDs) employing the reduced surface field (RESURF) effect have been presented. The devices have been optimized for a higher uniformity in the electric field profile that increases the internal quantum efficiency of the LEDs. These devices were designed in a 140 nm SOI-CMOS technology with a limited set of available mask layers, and hence doping levels (N). Moreover, the design rules set the lower bound on the p- and n-type layer widths ($d = 0.384$ μm). As a result, the breakdown voltages of the SJLEDs were relatively high. Based on our results in chapter 3, it is therefore interesting to pursue research on SJLEDs with advanced technologies, where d can be reduced and N can be increased. This would enable superjunction RESURF at lower breakdown voltages, which can further improve the power conversion efficiency.

## Chapter 5

In this chapter, a monolithic, galvanically isolated, laterally-coupled and wide-spectrum ($350$ nm $< \lambda < 1270$ nm) optical link in 0.14 μm silicon-on-

insulator CMOS technology has been demonstrated. Optical coupling has been analyzed in both forward and AM LED operation, quantified by the short-circuit current in the photodiode. The link exhibits a higher coupling quantum efficiency in AM LED operation as compared to forward mode LED operation. Improving the coupling quantum efficiency $\eta$ would mean consuming less electrical power to achieve the same bit error rate in the optical link, when used for intra-chip data communication. The efficiency of the AM LED can be enhanced by for e.g. optimizing $V_{BR}$ as discussed in Chapter 3, or employing SJ LEDs (Chapter 4). In high-intensity environments, the input optical power determines the SNR and thereby the bit error rate. For instance, a 3 Gb/s optical receiver with off-chip illumination ($\lambda$ = 850 nm) was reported [5] using PDs in standard 180 nm CMOS. On the other hand, if optical intensities are low (like in our monolithic link), the bit error rate and thereby the maximum acceptable data rate will be limited by the SNR at the output of the optical receiver, in spite of the fact that Si AM LEDs have been reported to exhibit GHz range small-signal modulation speeds [6]. High-speed communication in such a scenario is feasible by using highly sensitive SPAD based receivers, which are sensitive to the number of photons received per bit, and thereby relies on $\eta$. Prior art reported SPADs [7, 8] in the same SOI technology. Here, the maximum data rate is limited by the dead-time of the SPAD (depends in turn on bit error rate specifications). For example, a dead-time of ~ 100 ns was demonstrated in the work of [8] that translates into a maximum data rate in the order of ~ 10 Mb/s. Measuring the maximum achievable data rate in our optical link requires high-speed measurements with RF de-embedding test structures, including power efficient LED driver circuitry [9].

In addition, the wide-spectrum nature of avalanche-mode electroluminescence, offers new scope for the application of AMLEDs in integrated visible range photonic functionalities, which is an emerging trend in the optical community. So far, expensive multi-line lasers are needed as the optical source in such photonic integrated ICs. In specific applications, where the absolute optical power is not crucial, AMLEDs can serve as very cost-effective and compact solutions for generating multiple wavelengths of light from a single device. Visible range photonics are recently finding applications in fluorescence microscopy (used in biomedical analyses like DNA sequencing), on-chip spectrometry, food quality inspection, etc. Moreover, the fact that the same Si LED can emit both IR and visible range photons can be used to realize wavelength-domain multiplexing on-chip.

## Chapter 6

In this chapter, a FDTD analysis has been presented on wide-spectrum (480 nm $< \lambda <$ 1300 nm), dielectric slab waveguides employing SOI and silicon nitride for monolithic integration of optical links with on-chip, wide-

spectrum, low-intensity and isotropic light sources in a 140 nm SOI-CMOS technology. Geometrical conditions for tuning the waveguiding have been discussed. The transmission efficiencies have been estimated for varying geometry, and optical wavelengths emitted by conventional Si-based wide-spectrum LEDs. The adverse effect of galvanic isolation on the transmission efficiency has also been shown. The analysis can be easily extended to more complex optical links, such as on-chip optical excitation and also to simulate 3-D systems. In addition, back-end waveguiding in CMOS can be further investigated. For e.g. the effect of varying the material and/or geometry of the top cladding layer for the silicon nitride waveguide. As yet another example, metal-insulator-metal (MIM) stacks as a back-end waveguide can also be investigated.

## Original contributions of this thesis

The work presented in this thesis contains several original contributions:

- A model has been proposed that relates the EL-spectra and optical intensity of avalanche-mode silicon diodes to the magnitude and spatial distribution of the electric field, and the electron temperature profile.

- So far, the concept of non-local avalanche breakdown was reported only in the context of impact ionization in thin silicon diodes. For the first time, this thesis extends and incorporates this quasi-ballistic phenomenon to explain the experimentally observed dependency of the optical power efficiency on the breakdown voltage of $p^+$-n-$n^+$ silicon diodes and advanced bipolar transistors. In addition, the theory also predicts the aforesaid dependency for ideal scenarios of a one-dimensional triangular and rectangular (uniform) field-profile.

- The concept of superjunction (SJ) RESURF was so far used only in the context of overcoming the breakdown voltage versus on-resistance trade-off in power semiconductor devices. In this thesis, for the first time, SJ based AMLEDs have been realized in a 140 nm SOI-CMOS technology (A-BCD9). The design demonstrates a direct link between the spatial uniformity of the breakdown electric field and the internal quantum efficiency of the LED. In other words, RESURF has been used for the first time to increase the ratio of the EL-area to the total electrically active area.

- The thesis presents the design, characterization, and analysis of a wide-spectrum optical link formed by an Si LED and an Si PD, monolithically integrated in a BCD SOI-CMOS technology. Two figures of merit for such an optical link have been introduced. Firstly, the emission-specific responsivity of a PD that quantifies the spectral overlap between the irradiance of the LED and the responsivity of

the PD. Secondly, the coupling quantum efficiency, which highlights the combined efficiency of the LED, the WG, and the PD.

- Thermal coupling from an Si AMLED to an Si PD in SOI technology with galvanic isolation has been experimentally characterized for the first time, in both dc and transient (on-off keying) operation of the LED. The extracted junction temperature of the PD due to thermal coupling has been subsequently explained using a steady-state thermal lumped-element model of the system.

- An extensive FDTD analysis has been shown, for the first time, that discusses the various lateral optical paths and their respective propagation efficiencies, in order to study the waveguiding mechanism in the SOI-based optical link. Such a simulation exercise provides an in-depth understanding of monolithic optical coupling. It also provides insight into device-design optimization strategies.

- Last but not the least, the thesis describes, as supplementary work, experimental methods to obtain the optical transmission spectra of the thick back-end (inter-metal dielectric stack) present in standard CMOS technologies. This is useful to extract and de-embed a more precise spectral irradiance of the Si based LED.

I end here with yet another quote of Richard P. Feynman:

*"We are at the very beginning of time for the human race. It is not unreasonable that we grapple with problems. But there are tens of thousands of years in the future. Our responsibility is to do what we can, learn what we can, improve the solutions, and pass them on."*

# BIBLIOGRAPHY

[1] A. Sammak, L. Qi, W.B. de Boer, and L.K. Nanver, "PureGaB $p^{+}n$ Ge diodes grown in large windows to Si with a sub-300 nm transition region," Solid-State Electronics, vol. 74, pp. 126-133, 2012.

[2] G. Masini, G. Capellini, J. Witzens, and C. Gunn, "A 1550 nm, 10 Gbps monolithic optical receiver in 130 nm CMOS with integrated Ge waveguide photodetector," In proc. of $4^{th}$ IEEE International Conf. Group IV Photonics, pp. 1-3, 2007.

[3] S.J. Koester, C.L. Schow, L. Schares, G. Dehlinger, J.D. Schaub, F.E. Doany, and R.A. John, "Ge-on-SOI-detector/Si-CMOS-amplifier receivers for high-performance optical-communication applications," J. Lightwave Tech., vol. 25, no. 1, pp. 46-57, 2007.

[4] H. Wu, and P.D. Ye, "Fully depleted Ge CMOS devices and logic circuits on Si," IEEE Trans. Electron Devices, vol. 63, no. 8, pp. 3028-3035, 2016.

[5] S. Radovanovic, A.J. Annema and B. Nauta, "A 3 Gb/s optical detector in standard CMOS for 850 nm optical communication," IEEE J. Solid-State Circuits, vol. 40, no. 8, pp. 1706-1717, 2005.

[6] A. Chatterjee, B. Bhuva, and R. Schrimpf, "High-speed light modulation in avalanche breakdown mode for Si diodes," IEEE Electron Device Lett., vol. 25, no. 9, pp. 628-630, 2004.

[7] S. Mandai, M. W. Fishburn, Y. Maruyama and E. Charbon, "A wide spectral range single-photon avalanche diode fabricated in an advanced 180 nm CMOS technology," Opt. Express, vol. 20, no. 6, pp. 5849-5857, 2012.

[8] M-J. Lee, P. Sun and E. Charbon, "A first single-photon avalanche diode fabricated in standard SOI CMOS technology with a full characterization of the device," Opt. Express, vol. 23, no. 10, pp. 13200-13209, 2015.

[9] V. Agarwal, S. Dutta, A.J. Annema, R.J.E. Hueting, P.G. Steeneken, and B. Nauta, "Low power wide spectrum optical transmitter using avalanche mode LEDs in SOI CMOS technology," Opt. Express, vol. 25, no. 15, pp. 16981-16995, 2017.

APPENDIX A

# OPTO-ELECTRONIC MODEL PARAMETERS

Table A.1: List of fitting and physical parameters used in the opto-electronic model. $m_0$ = 9.11×10$^{-31}$ kg is the electron rest mass in vacuum.

| Parameter | Value |
|---|---|
| $E_{g1}$ | 1.12 eV (at 300 K) |
| $E_{g2}$ | 2.15 eV (at 300 K) |
| $E_{g3}$ | 3.2 eV (at 300 K) |
| $E_{p1}$ | 18.27 meV (at 300 K) |
| $E_{p2}$ | 57.73 meV (at 300 K) |
| $C_1$ | 5.5 |
| $C_2$ | 4.0 |
| $A_1$ | $3.231 \times 10^2$ cm$^{-1}$ eV$^{-2}$ |
| $A_2$ | $7.237 \times 10^3$ cm$^{-1}$ eV$^{-2}$ |
| $A_d$ | $1.052 \times 10^6$ cm$^{-1}$ eV$^{-2}$ |
| $v_{sat}$ | $10^7$ cm s$^{-1}$ (at 300 K) |
| B | $\sim 10^{-9}$ cm$^3$s$^{-1}$ |
| $m_e^*$ | $0.328 m_0$ |
| $m_h^*$ | $0.49 m_0$ |
| L | $116 \times 10^{10}$ s$^{-1}$ (at 300 K) |
| $V_{ref}$ | 6.72 V |
| m | $\approx$ 6.3 (fitted) |
| k | $\approx -1$ (fitted) |

APPENDIX B

# EXPERIMENTAL STUDY ON THE EL-SPECTRAL RIPPLES: BACK-END INTERFERENCE

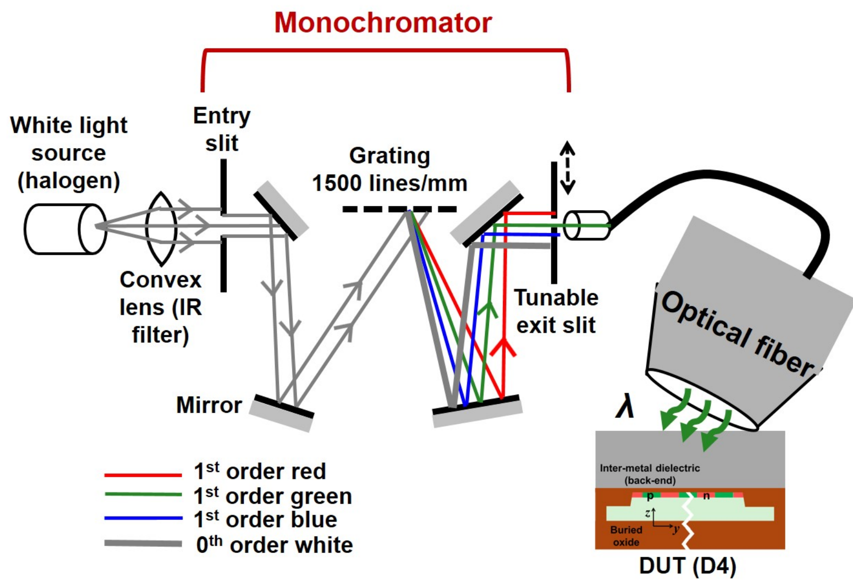


Figure B.1: Schematic of the experimental set-up used to measure the transmission spectrum of the inter-metal dielectric stack covering the SJ-LEDs in Chapter 4. The SJ-LED is operated as a photo-diode by illuminating it with light at finely resolved wavelengths ($\approx 5$ nm). The measured short-circuit current is proportional to the intensity of light at a given free-space wavelength $\lambda$ reaching the active area of the SJ-LED.

The measured AM-EL spectra of our AMLEDs fabricated in standard

SOI-CMOS technology (A-BCD9 from NXP Semiconductors) and the 65 nm bulk CMOS technology from TSMC exhibit significant ripples, in particular within 600 nm$< \lambda <$800 nm, with local crests and troughs located at specific wavelengths, irrespective of the device under test (DUT). The DUT in Chapter 2 is covered with a thin pure boron layer, but with relatively reduced ripple-amplitudes. In the other DUTs such as in Chapters 3, 5, and 4, the Si-surface of the SJ-LEDs are covered by a ~10 µm thick inter-metal dielectric (multi-layer back-end), and consequently the spectral ripples are more pronounced. This layer, despite having negligible optical absorption, acts as a composite Fabry-Perot cavity owing to its different refractive index ($\approx$ 1.4) in contrast to that of Si ($\approx$ 4.0). Prior to coupling through the optical fiber, the optical path of the vertically emitted photons consists of the multi-layer back-end and the $\sim$ 0.1-0.25 µm thick Si present between the junction plane and the oxide interface. In this appendix, two experimental methods along with their merits and limitations have been described, which were used to study the transmittance of this optical path and demonstrate the effect of Fabry-Perot interference due to the back-end.

## B.1 Method I: Spectral photocurrent technique

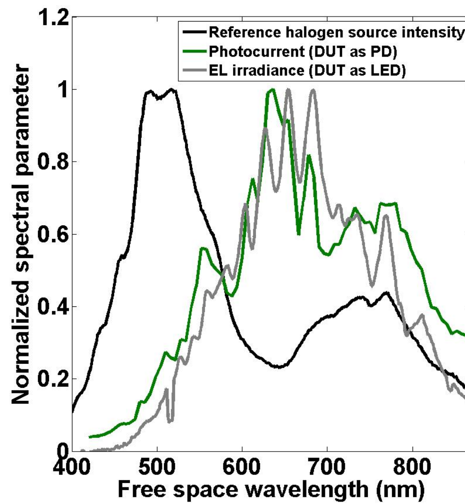


Figure B.2: Normalized spectral irradiance (blue) of the $0^{th}$ order white light from the monochromator used as an optical source to test the transmission spectrum of the back-end. The normalized photo-current (green) of the test diode is a relative measure of the transmission efficiency around a given optical wavelength.

In order to demonstrate the transmission spectrum of this optical path, we use the principle of reciprocity of light propagation, by operating the DUT (SJ-LED D4) as a PD to transduce light into measurable photo-current.

The optical set-up for this experiment is shown in Fig. B.1 is used. Wide-spectrum (white) light from a halogen source is passed through a bifocal convex lens, which creates a parallel beam and filters out IR wavelengths ($\lambda$ >900 nm) to reduce heat propagation. The beam is collimated with an entry slit of a monochromator, which is a mirror assembly consisting of a diffraction grating with 1500 lines/mm. The grating creates a spatially resolved continuous line spectrum, which is then projected onto a mechanically tunable exit slit. The position of the exit slit is then varied to select a specific $\lambda$. The position of the $0^{th}$ order maxima of all colors coincide, thereby producing visible white light at the lowermost position of the exit slit. The EL-spectrum of this reference white light is measured with the ADC-1000-USB spectrometer and is shown in Fig. B.2. The $1^{st}$ order maxima follow subsequently, in order of increasing $\lambda$. The gap-width of the exit slit can be optimized to allow sufficient intensity to exit, while maintaining a tolerable finesse (sharpness) of the selected spectral line as desired for the experiment. We use a gap-width of 0.5 mm in this work, and select spectral lines in steps of $\Delta\lambda$ = 5 nm. The emerging light is subsequently coupled to the optical fiber (the same one is used in measuring the EL-spectra) to illuminate the DUT, operated as a PD. The measured $I_{SC}$ for different $\lambda$ is proportional to the incident intensity, thereby yielding a relative measure of the transmission spectrum of the optical path as shown in Fig. B.2. The positions of the ripples in the measured photocurrent are in good agreement with those obtained in the measured EL-spectrum of the DUT (SJ-LED D4) as also shown in Fig. B.2.

*Merits*:

1. This method is handy to demonstrate the presence of back-end interference, plus its effect on the opto-electronic properties (photoconductivity) of a specific DUT.

2. Since near-monochromatic light is used to shine on the DUT with the optical fiber, the optical transmittance can be extracted with a good spatial precision.

3. In addition, since this method measures the photocurrent of the DUT, it takes into account the contribution of self-absorption in the Si DUT, when operated as an LED.

*Limitations*:

1. The relative irradiance of the halogen source has spectral non-uniformity (and does not have a perfectly white spectrum as ideally desired). This affects the overall measurement.

2. The method requires a separate monochromator, which has, in most situations, a different grating resolution and therefore a different

spectral resolution than the built-in diffraction grating of the spectrometer. Moreover, the measured spectrum is dependent on the spectral responsivity of the specific DUT. Both the factors make the process of de-embedding the optical transmittance from the measured EL-spectra of the LEDs rather cumbersome and inaccurate.

3. This method works only if the DUT has a sufficiently large quantum efficiency of detection within the spectral range of interest. This means that this method may not be efficient to demonstrate the back-end transmittance for forward biased EL-spectra of Si LEDs since Si has poor responsivity for $\lambda > 1000$ nm, even if an external optical source emitting at these wavelengths are at our disposal.

## B.2 Method II: Surface reflectance technique

This method measures the spectral reflectance from the surface of the DUT using a broad-spectrum halogen source. The optical set-up is shown in Fig. B.3. The DUT is illuminated by a parallel beam of light from a 31-31-81 halogen lamp from Bausch & Lomb, focussed using an objective lens (Leica P/N 311383). A part of the source beam is split and collected at the top with an optical fiber (Fiber 1). Fiber 1 is connected to an ADC-1000-USB spectrometer from Avantes, thus capturing the spectral irradiance of the source $S(\lambda)$. The reflected light from the surface of the DUT is collected with another optical fiber (Fiber 2) connected to the same spectrometer, thus capturing the spectral reflectance $R(\lambda)$. The back-end stack acts as a composite Fabry-perot resonating cavity. Fig. B.4 shows the measured $S(\lambda)$ and $R(\lambda)$.

As Si has a relatively high absorption in the spectral range of interest, and is much thicker ($\sim 400$ μm) than the back-end dielectric ($\sim$ 10-20 μm), the transmitted light $T(\lambda) = S(\lambda)$-$R(\lambda)$ can be assumed to be entirely attenuated within Si. Thus, we can neglect the effect of any reflection from deep in the Si body or from the bottom surface of the wafer. The spectral transmittance can then be extracted as $t(\lambda) = 1\text{-}R(\lambda)/S(\lambda)$, and is shown in Fig. B.5. The measured EL-spectrum of the DUT can be subsequently divided by this extracted $t(\lambda)$ to obtain the de-embedded EL-spectrum, as has been shown in chapter 3.

*Merits*:

1. Since the same built-in diffraction grating (thereby the same spectral resolution) is used to measure both $S(\lambda)$ and $R(\lambda)$, therefore this method can be directly used to de-embed the measured EL-spectrum of the LED.

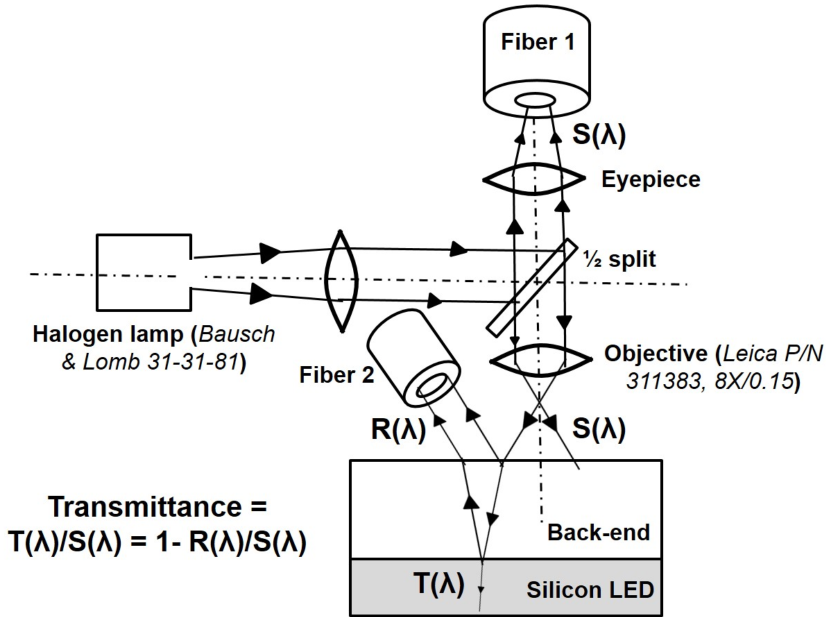


Figure B.3: Schematic of the experimental set-up to measure the spectral reflectance of the DUT.

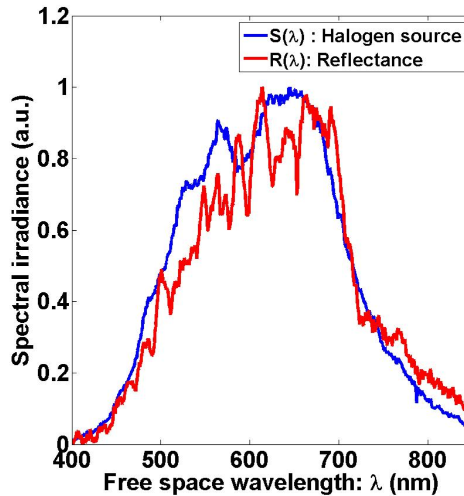


Figure B.4: Measured relative spectral irradiance of the halogen source and the reflected light from the DUT surface.

2. Since $t(\lambda)$ depends only on the ratio of $R(\lambda)$ to $S(\lambda)$, therefore this method is insensitive to the non-uniformities in the relative spectral irradiance of the halogen source itself.

3. This method does not depend on the quantum efficiency of detection of the DUT, since there is no electrical measurement involved. This

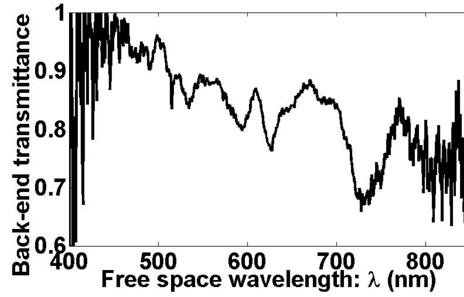


Figure B.5: Spectral transmittance t(λ) of the back-end stack extracted from reflectance measurement.

means that this method can also be extended to forward biased EL-spectra of Si LEDs, provided if we have a suitable optical source emitting at these wavelengths at our disposal.

*Limitations*:

1. This method does not subsume the opto-electronic properties (e.g. photo-conductivity) that are affected by the electronic band structure) of the specific DUT.

2. Since the illumination is done with an objective lens whose aperture is much bigger than the active area of the DUT itself, this method has a relatively poor spatial precision, and is expected to be prone to optical interference from regions/devices in close proximity to the DUT.

3. The optical source in this method is much brighter in comparison to the one in method I, because in this case the halogen source beam does not undergo chromatic separation prior to being incident on the DUT. Hence, stray reflections from unwanted surfaces might add up to the measurements. These effects, however, being independent of the DUT, get canceled out once we take the ratio of R(λ) to S(λ). Thus, this limitation can be bypassed.

APPENDIX C

# EQUIVALENT THERMAL MODEL OF THE SOI OPTICAL LINK AND FIT PARAMETERS

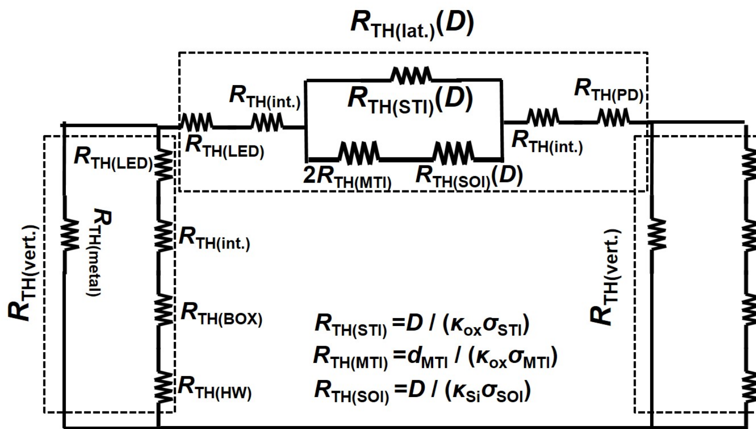


Figure C.1: Lumped thermal network of the SOI based optical link described in chapter 5, showing lumped thermal resistances contributed by various regions. $D$ is the link length, $\kappa$ is the thermal conductivity, and $\sigma$ is the cross-section area of the respective region.

We revisit the thermal model of the SOI based optical link described in chapter 5 and furnish more details. Fig. C.1 shows the schematic of the thermal network consisting of the lumped thermal resistances contributed by individual regions of the structure. The thermal resistance of region $i$ is represented by $R_{TH(i)}$, where $i$ can be "STI", "MTI", "SOI", "BOX", "HW" (handle wafer), "LED", "PD", "int." (interface), and "metal". Only

the components $R_{TH(STI)}$ and $R_{TH(SOI)}$ depend on the link length D. By definition, one can write:

$$R_{TH(i)} = \frac{l_i}{\kappa_i \cdot \sigma_i}. \tag{C.1}$$



Here $l_i$ represents the length of the respective region along the direction of heat flow, and we have: $l_{STI}$ = D, $l_{MTI}$ = $d_{MTI}$ = 0.8 μm, and $l_{SOI}$ = D - $2d_{MTI}$. The parameter $\kappa_i$ is the thermal conductivity of the material of the region, namely Si for LED, PD, SOI, and HW; oxide (ox) for STI, MTI, and BOX; or metal for the electrodes. $\sigma_i$ is the cross-sectional area normal to the direction of heat flow. The whole network can be simplified into an equivalent $\pi$-network as shown in Fig. C.2.

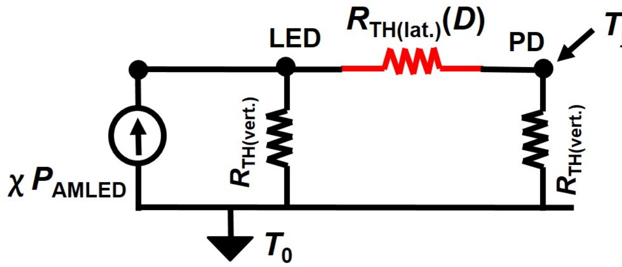


Figure C.2: An equivalent $\pi$-network model of the thermal network shown in Fig. C.1, which is excited by a DC power source via the avalanche-mode LED.

The vertical component $R_{TH(vert.)}$ comprises the sub-network formed by the LED, vertical interfaces, BOX, and HW in series, and the metal electrodes in parallel (see Fig. C.1). This lumped parameter is treated to be independent of D for reasons given in chapter 5.

The lateral component $R_{TH(lat.)}$ is D-dependent and is of importance to us. A simple network analysis leads to the following relation:

$$R_{TH(lat.)}(D) = R_{TH(ser.)} + r_1 \cdot D \cdot \frac{r_2 \cdot D + r_3}{(r_1 + r_2) \cdot D + r_3}, \tag{C.2}$$

where the parameters are given by

$$R_{TH(ser.)} = R_{TH(LED)} + R_{TH(PD)} + R_{TH(int.)}, \tag{C.3}$$

$$r_1 = (\kappa_{ox} \cdot \sigma_{STI})^{-1}, \tag{C.4}$$

$$r_2 = (\kappa_{Si} \cdot \sigma_{SOI})^{-1}, \tag{C.5}$$

$$r_3 = 2 \cdot R_{TH(MTI)} - \frac{2 \cdot d_{MTI}}{(\kappa_{Si} \cdot \sigma_{SOI})^{-1}}. \tag{C.6}$$

Now, consider the simplified $\pi$-network of Fig. C.2. The thermal excitation power $\chi \cdot P_{AMLED}$ is modeled analogous to a current source in the electrical domain. Here, $\chi \approx 1$, is the thermal power conversion efficiency and $P_{AMLED}$ is the DC electrical power dissipated in the avalanche-mode LED. The thermal power branches into two paths. The part $P_2$ that flows through $R_{TH(lat.)}$ is derived by simple resistive division to be

$$P_2 = \chi \cdot P_{AMLED} \cdot \frac{R_{TH(vert.)}}{R_{TH(lat.)} + 2 \cdot R_{TH(vert.)}}. \tag{C.7}$$

Consequently the difference between the PD junction temperature $T_j$ and the ambient temperature $T_0$ is simply $P_2 \cdot R_{TH(vert.)}$. Thus one finally obtains

$$T_j(D) = T_0 + \chi \cdot P_{AMLED} \cdot \frac{R^2_{TH(vert.)}}{R_{TH(lat.)}(D) + 2R_{TH(vert.)}}. \tag{C.8}$$

Note that the temperature difference $T_j - T_0$ is analogous to potential difference in the electrical domain. The only difference is that in electrical domain, the reference potential is typically chosen as ground or 0 V. In thermal domain, this is replaced by $T_0$ = 300 K.

By fitting the measured data for $\Delta T_j$ in chapter 5 to the model represented by Eq. C.8 via the least squares method, the aforesaid parameters have been obtained, and are listed in Table C.1 along with other extracted parameters for the optical link.

Table C.1: List of extracted/fit parameters for our optical link. Unless otherwise specified, values are for the default design without a heat sink and having a link length D = 28 μm. Values of $\eta_{AM}$ and $\eta_{FM}$ correspond to $T = T_0 = 300$ K, and $I_{AMLED} = I_{FMLED} = 4$ mA.

| Parameter | Value |
|---|---|
| $I_0$ | 1 fA |
| $\eta_{AM}$ (with heat sink, and D = 20 μm) | $4.0 \times 10^{-9}$ |
| $\eta_{FM}$ (with heat sink, and D = 20 μm) | $0.92 \times 10^{-9}$ |
| $TC_{VOC}$ | -2.5 mV $K^{-1}$ |
| $TC_{VPD}$ (at $I_{PD}$ = 1 mA forward bias) | -1.2 mV $K^{-1}$ |
| $TC_{ISC}$ | 0.12 pA $K^{-1}$ |
| $\Delta T_j/P_{AMLED}$ (without heat sink) | 180 K $W^{-1}$ |
| $\Delta T_j/P_{AMLED}$ (with heat sink) | 30 K $W^{-1}$ |
| $\tau_{thermal}$ (without heat sink) | 126 ms |
| $\tau_{thermal}$ (with heat sink) | 40 ms |
| $\gamma_{FM}$ (with heat sink) | 0.072 dB $\mu m^{-1}$ |
| $\gamma_{AM}$ (with heat sink) | 0.195 dB $\mu m^{-1}$ |
| $R_{TH(ser.)}$ (with heat sink) | 725.4 K $W^{-1}$ |
| $r_1$ (with heat sink) | 862.3 K $W^{-1}$ $\mu m^{-1}$ |
| $r_2$ (with heat sink) | 31.1 K $W^{-1}$ $\mu m^{-1}$ |
| $r_3$ (with heat sink) | 356.5 K $W^{-1}$ |
| $R_{TH(vert.)}$ (with heat sink) | 258.8 K $W^{-1}$ |

# LIST OF PUBLICATIONS

## Peer reviewed

1. V. Agarwal, **S. Dutta**, A.J. Annema, R.J.E. Hueting, P.G. Steeneken, and B. Nauta, "Low power wide spectrum optical transmitter using avalanche mode LEDs in SOI CMOS technology", Optics Express, vol. 25, no. 15, pp. 16981-16995, 2017.
2. **S. Dutta**, L. Orbe, and J. Schmitz, "TCAD analysis of wide-spectrum waveguides in high-voltage SOI CMOS", proceedings of the 17$^{th}$ IEEE International Conference on Numerical Simulation of Optoelectronic Devices (NUSOD), p. MC4, 2017 (DOI: 10.1109/NUSOD.2017.8009969).
3. **S. Dutta**, G.J.M. Wienk, R.J.E. Hueting, J. Schmitz, and A.J. Annema, "Optical power efficiency versus breakdown voltage of avalanche-mode silicon LEDs in CMOS", IEEE Electron Device Lett., vol. 38, no. 7, pp. 898-901, 2017.
4. **S. Dutta**, P.G. Steeneken, J. Schmitz, A.J. Annema, and R.J.E. Hueting, "The avalanche-mode superjunction LED", IEEE Trans. Electron Devices, vol. 64, no. 4, pp. 1612-1618, 2017.
5. **S. Dutta**, V. Agarwal, R.J.E. Hueting, J. Schmitz, and A.J. Annema, "Monolithic optical link in silicon-on-insulator CMOS technology", Optics Express, vol. 25, no. 5, pp. 5440-5456, 2017.
6. R.J.E. Hueting, A. Heringa, B.K. Boksteen, **S. Dutta**, A. Ferrara, V. Agarwal and A.J. Annema, "An Improved Analytical Model for Carrier Multiplication Near Breakdown in Diodes", IEEE Trans. Electron Devices, vol. 64, no. 1, pp. 264-270, 2017.
7. V. Agarwal, A.J. Annema, **S. Dutta**, R.J.E. Hueting, L.K. Nanver, and B. Nauta, "Random Telegraph Signal phenomena in avalanche mode diodes: Application to SPADs", proceedings of the 46$^{th}$ European Solid-State Device Research Conference (ESSDERC), pp. 264-267, 2016.
8. **S. Dutta**, R.J. E. Hueting, V. Agarwal, and A.J. Annema, "An integrated optical link in 140 nm SOI technology", proceedings of the Conference on Lasers and Electro-Optics (CLEO), Session JW2A, p. 132, 2016.
9. **S. Dutta**, R.J.E. Hueting, A.J. Annema, L. Qi, L.K. Nanver and J. Schmitz, "Opto-electronic modelling of light emission from avalanche-mode silicon p$^{+}$n junctions", J. Appl. Phys., vol. 118, no. 11, 114506, 2015.

## Other

1. Contributory talk on "Light from silicon", MESA+ Symposium 2017, Enschede, The Netherlands.
2. Invited talk on "Optocoupling in standard CMOS for smart power", Emerging Technologies Conference (ETCMOS), Warsaw, vol. 6, Advanced Materials and Optoelectronics Track, pp. 45-61, 2017.
3. **S. Dutta**, R.J.E. Hueting, L.K. Nanver, and J. Schmitz, "Avalanche-mode LEDs in silicon", ICT Open, Amersfoort, The Netherlands, 2016.

4. **S. Dutta**, R.J.E. Hueting, L.K. Nanver, and J. Schmitz, "Optocoupling in CMOS: Avalanche-mode LEDs in silicon", (poster) MESA+ Symposium 2015.

# ACKNOWLEDGMENTS

"Since you are reading this page, it actually means that I have achieved my objective in doing (or rather entering the world of) "research", which has been indeed one of my main mottos while growing up. Most people at this time of their career would say, "Life in these four hard-working years has been a roller-coaster ride". Well, not in my case, because I perceived my four years of research as a staircase. I was lucky not to find myself gravitating downwards, although at each step I did stop for a while, figuring out where I was heading to. But a staircase also means that the journey was never smooth. Life, much like photons, comes in discrete and entangled bits, where you get some chances of survival. Anyway, I am supposed to thank people in this section, who helped, nurtured and spent time with me during this four-year journey. A couple of pages is not enough to thank everyone, so if I have missed your name, apologies in advance.

I would start here by thanking my daily supervisor Dr. Raymond J.E. Hueting (Ray) and my project leader Dr. Anne-Johan Annema (AJ). You guys were the first people from the Netherlands, I talked to. AJ, as a foreigner I wrongly pre-conceived you to be a lady before seeing you on Skype. Thanks for selecting me. Thanks for playing the role of the strictest in-house reviewer for all my papers, and presentations, to make them reader-friendly. Thanks for teaching to pluck "low-hanging fruits" and "fit everything into a bigger picture". Apologies for the slight disagreement we had during paper writing. Ray, I have achieved the feat of knowing your middle names but I am omitting them here for brevity ;-) . You were the friendliest, and the most supportive supervisor I could ever ask for. You acted as a litmus paper for all my random daily ideas and discussions. As they say, first impressions matter a lot. You gave a very nice first impression of this country and its people. I enjoyed the freedom and friendly work atmosphere, which amazed me so much in a positive way. Thanks to Remke, for being the lighthouse upon my arrival to Twente and settling here properly. Thanks for organizing the day outs and the Christmas dinners. Thanks to Jurriaan, for being a different kind of guide on how to think like a scientist. You always knew how to make my papers and articles catchy; I learnt a lot of lexical nuances. Special thanks to Prof. dr. Lis Nanver. Lis, without you my work wouldn't have got the desired kick-start. Technically and psychologically, you and your devices showed me "the light". Thanks to Prof. Dr. Peter Steeneken, who spent many priceless hours in making our tape-outs a success and teaching me new things in design. Peter, thanks for all the chip-finishing work and for your patience throughout in listening to my results. Thanks to Maarten Swanenberg for his valuable suggestions and comments during our user committee meetings. Thanks Vishal, my project partner, for his patience in circuit design, layout and time-consuming measurements to drive my unconventional LEDs in standard CMOS. Thanks prof. dr. Edoardo Charbon and M-J. Lee for their timely insight into SPADs and helping in our design. Thanks to Sander, who was my lab teacher. In all my work, you were the "basement brick" a phrase that I translated from Hindi, meaning a true support who often goes without receiving much of the deserved credit. You were also my needed ears to practise my Dutch at random times. "Van harte bedankt voor je waardevolle geduld." In the final phase of my PhD, three more people deserve mention. Firstly, Luis Orbe, who spent his precious time to comment and check my simulation results. Secondly, Jingjing Xie for her timely help in making my numerical simulations up and running in no time. Thirdly Jeroen Korterijk from Optical Sciences group, for his prompt support in setting up my optical experiment involving the monochromator.

I will now move on to my "very selective" friends (outside work) who deserve mention. They were full of fun, and didn't let me feel, at least for a certain period of time, to be living in a remote corner of the country. Starting with Miquel, who was an invaluable friend for the very short time I have seen him. Special thanks to Matteo, who was my host the moment I arrived in Enschede. Next, I would like to thank three special friends I made in Enschede, who were fun and motivating to be with: Dr. Johan Skolski (just Johan for me), probably you were the most jubilant person I ever spent time with. Thanks for the all the fun we had hanging out in the city center, trying every bar and restaurant on Friday evenings. Thanks for a fun-filled Christmas market trip, which was unforgettable in so many aspects, probably because I was not completely drunk. "Merci". Thanks to Dr. Jozef Vincenc Obona (just Jozef for me). You were so fun to hang out with. Thanks to our mundane discussions. Thanks for giving me good advices when needed. Road trips in Germany, Czechia, and Bratislava couldn't be more interesting if they weren't with you. "Daku jem". Thanks to Paul, my first Dutch friend and one of the smartest I ever met, who had time for me, to hang out. Thanks Maria for being a nice company in Vienna, especially for drinking tea with cats around. Thanks Kelcy for trying out Salsa lessons with me.

I should now focus on my colleagues. Thanks Ines, Boni, Alessandro, Hugo, Johan (this one is Dutch) and DJ for all the fun, movies, beers, and intelligent discussions. Thanks Boni and Alessandro for helping and motivating me in my work. Thanks to Alessandro for also being spontaneous in planning a quick vacation in Barcelona. Thanks to Alessandro and DJ (also my paranymphs) in particular for making the awesome road-trip in Iceland. Thanks to Sourish for being a homely friend sitting a few feet away to have some fun breaks during work. Glad that you pushed me enough to go for the Aurora hunt in Sweden. It was a remarkable trip of a lifetime, inside the Arctic circle. On a serious note, thanks to him for providing me the opportunity to learn about atomic layer deposition mechanisms of GaN and AlN, and contribute (both conceptually and practically) to measurement techniques such as XRD, XPS, and plasma optical emission spectroscopy. Thanks to Gaurav, for giving me the much needed distraction to take part in discussions and problems in his own work. I learnt a lot about GaN and TCAD simulations in general. Thanks to the Dutch nation. I fell in love with biking all over again. It is the only country where I have seen a flyover for bikes. Only I wish the trains here were a tad bit better. Thanks to the neighbors Germany, and France, where I fulfilled my high-speed railway-desires by quickly planning a few vacations in those countries. Thanks to all those acquaintances I made during all my traveling (Floris, Gregory, Jamie, Miranda, Rosalba, Daniele, Florian, Eliana). Special thanks to "thuisbezorgd.nl" for delivering food on busy/lazy evenings on those fast and noisy "bromfiets". Lastly, thanks to my paranymphs to do the honor of walking down the aisle with me in this wedding ceremony, where I am getting married to science."

Satadal Dutta

29$^{th}$ September 2017
Enschede.

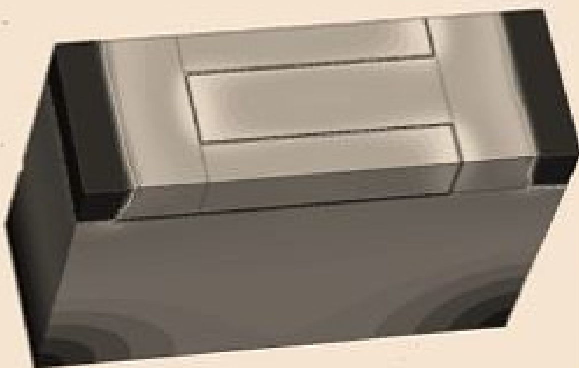

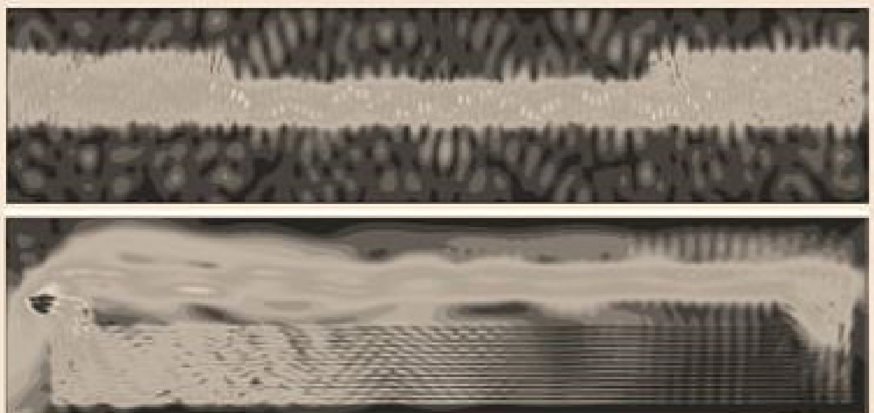

ISBN: 978-90-365-4413-9

DOI: 10.3990 / 1.9789036544139